CHAPTER 9

Plasma-Enhanced Chemical Vapor Deposition of Functional Coatings

L. Martinu, O. Zabeida and J.E. Klemberg-Sapieha

Department of Engineering Physics, École Polytechnique de Montréal, CP 6079, Station Centre-Ville, Montréal, Québec H3C 3A7, Canada

Summary 393
9.1 Introduction 393
9.1.1 Functional Coating Considerations 393
9.1.2 Plasma Processing of Materials 397
9.2 Processes in PECVD 399
9.2.1 Process Parameters 399
9.2.2 Plasma Gas-Phase Reactions 399
9.2.3 Plasma–Surface Interactions 400
9.3 PECVD Reactors and Deposition Concepts 402
9.3.1 General Considerations 402
9.3.2 Low-, Medium- and Radio-Frequency Plasma Reactors 403
9.3.3 Microwave and Dual-Mode MW/RF Plasma Systems 403
9.3.4 Complementary Plasma Systems 405
9.4 Process Diagnostics and Monitoring 406
9.4.1 Diagnostic and Monitoring Techniques 406
9.4.2 Plasma Characteristics of PECVD Processes and Energetic Aspects of Thin Film Growth 408
9.5 PECVD Materials: Effect of Surface Processes on the Microstructure and Properties 414
9.5.1 Characterization Methodology Specific to PECVD Coatings 414
9.5.2 Silicon-Based (Inorganic) Coatings 416
9.5.3 Carbon-Based and Related Coatings 423
9.5.4 Metal-Based Compound and Nanocomposite Films 427
9.5.5 Interface Engineering 432
9.6 Functional Characteristics and Applications of PECVD Coatings 436
9.6.1 Optical and Related Functional Coating Systems 437
9.6.2 Protective Tribological Coatings 449
9.7 Future and Perspectives 457

Copyright © 2010 Peter M. Martin. Published by Elsevier Inc.
All rights reserved.

Summary

Plasma-based technologies are increasingly used for the fabrication of thin films and coatings for numerous applications ranging from optics and optoelectronics to aerospace, automotive, biomedical, microelectronics, and others. The present chapter reviews the advances in plasma-enhanced chemical vapor deposition (PECVD). Based on knowledge of fundamental physical and chemical processes in the active plasma environments, we describe present understanding of plasma–surface interactions that are the cornerstone for tailoring the materials' functional characteristics, in particular their optical, mechanical, electrical, tribological, protective, and other properties. We illustrate the state of the art in PECVD by the description of the performance of different coating systems and thin film architectures suitable for industrial-scale applications. This chapter represents a source of information for those who wish to familiarize themselves with the status of knowledge in the area of materials science of functional coatings, in particular in PECVD, as well as for those who seek inspiration for practical surface engineering solutions.

9.1 Introduction

9.1.1 Functional Coating Considerations

Recent advances in science and technology have stimulated the development of new coating materials, surface and interface engineering processes, and thin film systems, that provide ever-improving performance in numerous areas, ranging from optics and optoelectronics to aerospace, automotive, biomedical, microelectronics, and other applications. Many successful solutions in these fields have been identified which are generally based on a layered functional coating architecture, schematically illustrated in Figure 9.1. In each case, one individual layer or the whole thin film system may simultaneously fulfill several functions (e.g. selective optical absorption and mechanical protection; optical transparency and gas barrier; antistatic

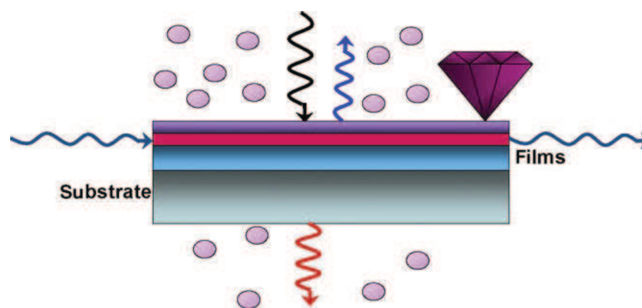

Figure 9.1: Schematic illustration of a functional coating system.

Table 9.1: Main functional characteristics of PECVD coatings and thin film systems

Functional properties	Controlled characteristics
Optical	Refractive index, n
	Extinction coefficient, k
	Optical loss, absorption coefficient, α
	Color: La^*b^* or Xyz coordinates
Mechanical	Adhesion: work of adhesion, W_a; critical load, L_C
	Stress, σ
	Hardness, H
	Young's modulus, E
	Toughness, K_T
Tribological	Coefficient of friction, μ
	Scratch resistance: critical load, L_C
	Wear coefficient, K
	Erosion rate, E_R
	Corrosion resistance: open circuit potential, OCP; corrosion current, I_{corr}
Electrical	Resistivity, ρ
	Dielectric loss, tan δ
	Charge carrier density, N_C
	Charge mobility, μ_C
Thermal	Coefficient of thermal expansion, CTE
	Thermal conductivity, γ_T
Barrier	Gas permeability, OTR
	Water vapor permeability, WVTR

properties and scratch resistance; erosion and corrosion resistance; fatigue resistance and high thermal conductivity; wear resistance and biocompatibility; photocatalytic effect and hydrophobicity; and numerous other combinations of properties summarized in Table 9.1). Therefore, it is increasingly important to assess and optimize the film characteristics not only individually, but in their complexity, with respect to their compatibility with other layers, and with respect to their designed applications. This imposes particular requirements on the fabrication methods and characterization.

Functional coating systems can be fabricated by different deposition techniques reviewed in detail in the present book; these include physical vapor deposition (PVD) from a solid primary source (e.g. thermal or electron beam evaporation, magnetron or ion beam sputtering, cathodic arc deposition), chemical vapor deposition (CVD) from a gas-phase primary source, plasma-enhanced chemical vapor deposition (PECVD) from a gas-phase source with activation in a glow discharge environment, and other vacuum and non-vacuum techniques

(sol-gel, flame hydrolysis, electrochemical and electroless deposition, thermal-, plasma-, and cold-spraying, and others).

Among the above processes, PECVD has received particular attention, as documented by earlier reviews [1–8]; it has been employed industrially in microelectronics for several decades, and it has now penetrated into a large number of other sectors as illustrated in Table 9.2. In certain areas (e.g. in optics), its industrial acceptance was originally slow, mainly owing to the complexity of the plasma–chemical reactions, plasma–surface interactions, and process control. However, thanks to fundamental and applied research and the development of new instrumentation tools, recent advances in plasma processing, and in PECVD in particular, have greatly increased the interest in PECVD for the fabrication of different coating systems. Its industrial use has been significantly broadened, as also illustrated throughout this chapter and in the relevant references. Not only can PECVD provide materials with functional characteristics similar to those obtained by their PVD and non-vacuum counterparts, but the PECVD processes can frequently address numerous novel aspects of functional coating fabrication. The main driving forces and stimulation for such interest reside with the following attributes, addressed in detail throughout this chapter:

- The broad range of control of plasma–chemical reactions and plasma–surface interactions allows one to optimize the film composition and microstructure: the films generally possess a high packing density ($\sim 98\%$), and are therefore hard and environmentally stable. This can be achieved by tailoring the energetic interaction between the plasma and the surface, frequently by using bias-controlled or pulsed plasma techniques. In one deposition reactor, one can fabricate a multifunctional system (such as the one schematically illustrated in Figure 9.1), while providing a combination of the desired optical, mechanical, thermal, and other properties.
- PECVD is suitable for the fabrication of films with different compositions and microstructures, allowing one to continuously vary film characteristics as a function of depth (graded or inhomogeneous films). This can be used for the fabrication of a very attractive category of optical devices such optical rugate filters, as well as hard and tough protective coatings and biomedical materials. The absence of abrupt interfaces (in addition to specific optical and other effects) leads to a uniform distribution (or compensation) of internal stresses, generally giving rise to enhanced adhesion and mechanical integrity.
- PECVD provides high deposition rates ($r_D \sim 1$–10 nm/s, or more), substantially higher than other, more traditional vacuum-based techniques (e.g. PVD). This is the basis for a reliable low-cost fabrication technology.
- Different substrate shapes (including 3D) can be uniformly coated (flat, hemispherical, cylindrical shapes, interior of tubes, etc.).

Table 9.2: Applications of PECVD functional coatings

Application	Examples of devices and film systems
Microelectronics and microsystems	Transistors Microelectromechanical systems (MEMS)
Optics, photonics, telecommunication and information technologies	Optical interference filters (including antireflective (AR) coatings) Ophthalmic lenses Optical waveguides Displays (including barrier coatings) Decorative (protective) coatings Optical coatings on plastics Protective coatings for storage media
Aerospace and outer space	Protective coatings against solid particle erosion and corrosion Protection against space environment (atomic oxygen, radiation, thermal cycling, charge accumulation)
Automotive	Protective coatings for engine components (low friction and wear) Protective coatings for light assemblies (corrosion resistance) Protective coatings for fuel distribution (permeation barriers)
Energy generation and saving	Photovoltaics (amorphous and polycrystalline silicon, AR coatings) Protective coatings for fuel cells Corrosion-resistant coatings Self-cleaning (photocatalytic) surfaces Smart windows
Biomedical and pharmaceutical	Protective coatings for implants Protective coatings for surgical tools Biocompatible coatings
Sensors	Miniaturized microphone (mechanoacoustic effects) Gas and vapor sensors (electrical, optical, and structure-related effects)
Manufacturing	Protective coatings on cutting tools (high-speed machining, dry machining, machining of non-ferrous metals, of non-metals and composites) Antisticking coatings (e.g. molds)
Textiles	Hydrophobic coatings Antiseptic textiles
Packaging	Barriers against gas and vapor permeation coatings on flexible substrates

- The PECVD process is compatible with different types of film fabrication equipment – this appears very attractive when retrofitting existing hardware to accommodate this deposition technology. In addition, the deposition process occurs at low temperatures (typically ranging from near room temperature (RT) with no intentional heating, to about 350 °C, when additional heating is applied).
- In recent years, we have witnessed an increasing interest in materials processing using atmospheric pressure glow discharge (APGD) [9, 10]. This has also stimulated much progress in PECVD at elevated pressures pointing toward possible low-cost, high-throughput, coating fabrication approaches.

9.1.2 Plasma Processing of Materials

Historically, the real onset of the plasma processing of materials (specifically using glow discharges) came in the late 1960s with the advent of integrated circuit technology. Electronics, in mid-1990 a $1.5 trillion industry worldwide, has enabled most other products to evolve (see Table 9.2). The electronics industry, in turn, is fed by the $100–200 billion annual semiconductor market, which is based on $40–50 billion equipment and materials sectors, of which plasma reactors constitute annual sales exceeding $2 billion [11]. These numbers are continuously increasing, given the acceptance of plasma-based technologies in other areas.

Based on the variability and the role of the initial gas-phase processes and plasma–surface interactions (involving atoms and molecular fragments – radicals, ions, and energetic photons), materials processing using ‘cold’ (thermodynamically non-equilibrium) plasma can be divided into the following categories, based on the choice of the working gases or vapors and the discharge conditions:

- PECVD of inorganic thin films (such as oxides, nitrides and carbides of metals or semiconductors) or organic thin films (such as soft materials, also called ‘plasma polymers’, hard carbon films, crystalline diamond and others) – the main subject of this chapter
- plasma etching or sputter-etching (dry removal of materials), forming volatile products resulting from the chemical reactions of the plasma-generated free radicals and surface atoms, which are frequently ablated with additional ion bombardment assistance (for an overview, see [4, 12])
- surface modification, during which material is neither added nor removed in significant amounts, but the composition and structure of the surface and/or of the near-surface layers are controllably modified by plasma exposure; this process allows one to tailor the surface and interface properties (for example, to improve adhesion

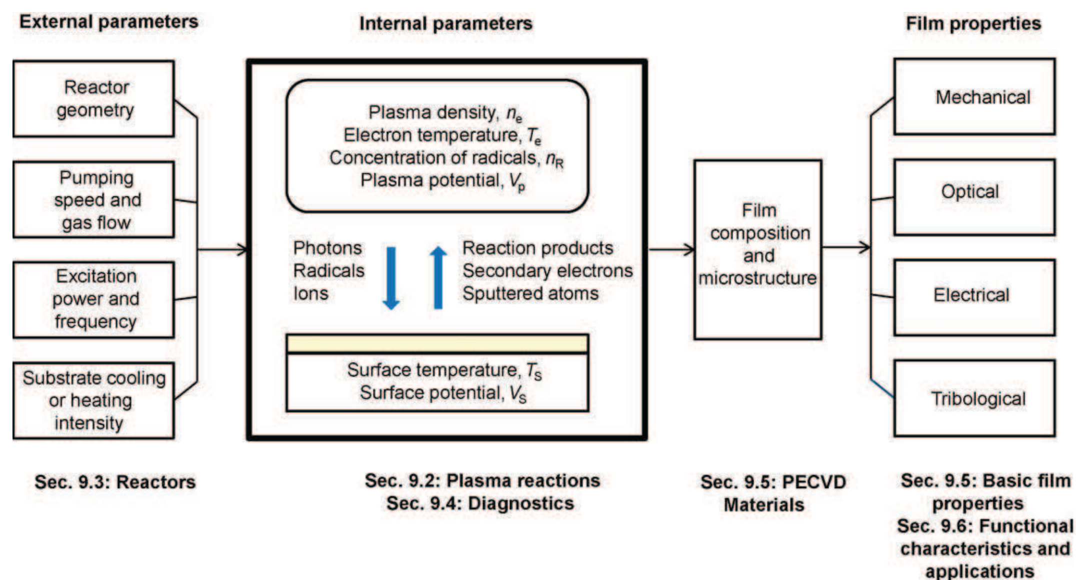

Figure 9.2: Schematic illustration of the structure of this chapter and of the relation between the deposition system, the internal and external process parameters, and the film characteristics.

before film deposition, surface hardness and control roughness, and/or to add specific surface functions providing wettability, biocompatibility, sterility, dye uptake, etc.) (for an overview, see [4, 11, 13, 14]).

Often, these three processes are in competition, and the prevalence of one of them can be controllably adjusted by the choice of the external plasma parameters (Figure 9.2).

The main objective of the present chapter is to review advances in PECVD of functional coatings for different applications (the first item in the above list). We start with a succinct overview of basic phenomena involved in the gas-phase reactions and plasma–surface interactions (Section 9.2) that are at the core of different reactor concepts (Section 9.3), while relying on the use and capabilities of different plasma diagnostic and process monitoring tools (Section 9.4). This is followed by the description of the properties of various PECVD materials, governed by their composition and microstructural characteristics, frequently tailored by an appropriate choice of the energy (E_i) and flux (Φ_ι) of the impinging ions (Section 9.5). Finally, we review PECVD film architectures suitable for specific applications illustrated by industrial-scale PECVD systems (Section 9.6). We wish to emphasize here that, considering the very extensive literature which now exists in this field, we have not attempted to list all of the relevant publications, but rather use a selection of examples which we feel represents the particular physical, chemical, materials science, surface engineering, and technological viewpoints advanced in this work.

9.2 Processes in PECVD

9.2.1 Process Parameters

In spite of the proliferation of low-pressure plasma processes already in use, or having potential for near-term or longer term industrial applications, there is still much ongoing research regarding the most efficient use of plasma. The reasons for this are the relative novelty of plasma, on the one hand, and its inherent complexity, on the other. To ensure high quality and reproducibility of a given plasma process, numerous parameters must be controlled (Figure 9.2); these include so-called 'external' parameters such as pressure, p, gas flow, discharge excitation frequency, f, power, P, and the resulting 'internal' plasma characteristics, particularly the electron (plasma) density, n_e, the electron energy distribution function, $f_e(E)$ or EEDF, electrical potentials, and fluxes of different species toward the surfaces exposed to plasma.

Gas-phase chemical processes are largely responsible for the chemical composition of the films deposited, along with plasma–surface interactions and substrate surface conditions, which dictate film microstructure and surface morphology.

9.2.2 Plasma Gas-Phase Reactions

During deposition, the bulk plasma parameters generally control the rate at which chemically active precursor species (molecular fragments – free radicals) and energetic species (electrons, ions, photons) are created. Even for relatively simple gas mixtures involving two or three gases, several dozens of plasma reactions are taking place and many new species are created. For many of these processes the reaction rates are not readily available. This complicates the detailed modeling of PECVD (e.g. [15]); instead, the experimental approach that takes into account the very general pathway combined with the process optimization is frequently used.

The EEDF is an essential parameter for plasma processing. It represents how many electrons are available for the ionization and other plasma reactions, for example, electron-impact dissociation, that produces free radicals. The radicals created in the plasma bulk interact further in the gas phase and at the surface, thus ultimately leading to film formation (Table 9.3).

EEDF is affected by all external parameters in a complex way. As an example, Figure 9.3 shows experimentally determined EEDFs in an active CH_4/H_2 radio frequency (RF) inductively coupled plasma (ICP), in which variation of p is seen to affect the mean electron energy and the energetic tail.

One of the important factors influencing the EEDF and processing plasma is the discharge field frequency, $f = \omega/2\pi$. Most often, high-frequency plasmas ($f > 1$ MHz) are used for PECVD of dielectric films, in order to avoid surface charging and plasma instabilities. These

Table 9.3: Basic reactions in active plasma environments

Reaction	General equation	Example
Reactions with electrons		
Ionization	$e + A \rightarrow A^+ + 2e$	$e + N_2 \rightarrow N_2^+ + 2e$
Excitation	$e + A \rightarrow A^* + e$	$e + O_2 \rightarrow O_2^* + e$
Dissociation	$e + AB \rightarrow e + A + B$	$e + SiH_4 \rightarrow e + SiH_3 + H$
Dissociative ionization	$e + AB \rightarrow 2e + A^+ + B$	$e + TiCl_4 \rightarrow 2e + TiCl_3^+ + Cl$
Dissociative attachment	$e + AB \rightarrow A^- + B$	$e + SiCl_4 \rightarrow Cl^- + SiCl_3$
Three-body recombination	$e + A^+ + B \rightarrow A + B$	$e + H^+ + CH_4 \rightarrow H + CH_4$
Radiative recombination	$e + A^+ \rightarrow A + h\nu$	$e + Ar^+ \rightarrow Ar + h\nu$
Reactions between heavy species		
Charge exchange	$A^+ + B \rightarrow A + B^+$	$N_2^+(fast) + N_2(slow) \rightarrow N_2(fast) + N_2^+(slow)$
Penning ionization	$A^* + B \rightarrow A + B^+ + e$	$He^* + O_2 \rightarrow He + O_2^+ + e$
Ionization by interchange	$A^+ + BC \rightarrow AB^+ + C$	$N^+ + O_2 \rightarrow NO^+ + O$
Combination	$A + B \rightarrow AB$	$2SiH_3 \rightarrow Si_2H_6$
	$AB + CD \rightarrow AC + BD$	$SiH_2 + O_2 \rightarrow SiO + H_2O$
Heterogeneous interactions (with surfaces)		
Adsorption	$R_g + S \rightarrow R_S$	$CH_2 + S \rightarrow (CH_2)_S$
Metastable deexcitation	$A^* + S \rightarrow A + S$	$N_2^* + S \rightarrow N_2 + S$
Sputtering	$A^+ + B_S \rightarrow A + B$	$Ar^+ + H_S \rightarrow Ar + H$
Secondary electron emission	$A^+ + S \rightarrow S + e$	$O^+ + S \rightarrow S + e$

R: radical; S: surface; g: gas.

are, generally, the International Telecommunications Union (ITU)-approved industrial, scientific, and medical frequencies (13.56 MHz – radio frequency, RF; or 2.45 GHz – microwave, MW) [16]. Higher frequency leads to higher power efficiency, i.e. less power is needed (on average) to create one ion–electron pair [17]. As a consequence, the ionization and dissociation rates are higher in the MW plasma than in RF plasma, generally leading to a higher r_D and a higher ion flux, Φ_i, toward the exposed surface [18].

Optimization of the PECVD processes involves identification of discharge characteristics giving rise to the formation of large densities of free radicals (n_R) that diffuse toward the surface (flux of the film forming species, Φ_ν), as well as to high concentrations of ions (due to high n_e) favoring high Φ_i, as will be discussed in the subsequent sections.

9.2.3 Plasma–Surface Interactions

We have pointed out above that the choice of f defines the deposition reactor, and it influences the fundamental plasma properties such as the EEDF; however, it also has an important effect

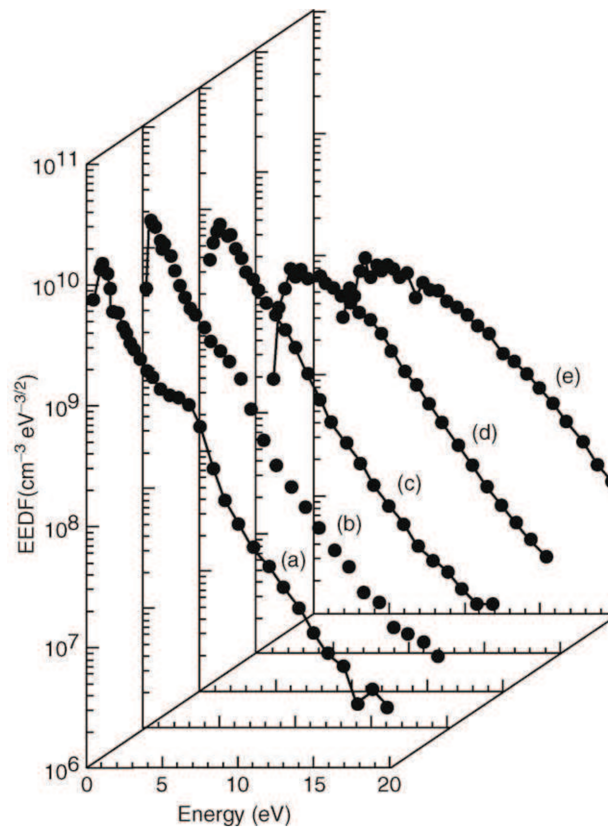

Figure 9.3: Electron energy distribution functions in a CH_4/H_2 (5:75 mixture) plasma as a function of pressure: (a) 50 mtorr, (b) 40 mtorr, (c) 30 mtorr, (d) 20 mtorr, and (e) 10 mtorr. This example pertains to an RF inductively coupled (ICP, 13.56 MHz) plasma reactor, 1 kW power, plasma volume of ~ 1.5 liters. (After [19].)

on how the plasma interacts with the exposed surface. At a surface in contact with plasma, there is an interface, the plasma sheath, which is electrically non-neutral, in contrast to plasma itself. An electrically isolated surface is at a floating potential, V_f, with respect to the plasma potential, V_p. Since $V_f < V_p$, positive ions are accelerated from the plasma to the surface, while some of the electrons are repelled. However, under steady-state conditions, no net current flows, since ion and electron fluxes are then equal. In this case, the thickness of the sheath, d_s, is a few times the Debye length, λ_D, and grows with increasing average electron energy and decreasing n_e.

Assuming, for simplicity, that the EEDF is Maxwellian, and that the surface immersed in the plasma is a plane, the potential difference across the sheath can be

approximated by [20]:

$$V_p - V_f = (k_B T_e/2e)\ln(m_i/2\pi m_e) \tag{9.1}$$

where k_B is the Boltzmann constant, T_e the electron temperature, e the electron charge, and m_i and m_e the masses of ions and of electrons. We note that on floating potential surfaces, the ion energy $E_i = e(V_p - V_f)$ is typically a few times the electron temperature expressed in electron volts. The ions always acquire some additional energy as they pass through the sheath on their way to the surface.

The energy of the charged particles impinging on a substrate can be adjusted by biasing it at a potential V_B with respect to V_p. For the case of an insulating material, it can only be biased by applying a periodic voltage. The substrate surface exposed to the plasma is then capacitively charged, that is, electrically polarized, providing a mean DC voltage component, V_B. When a positive ion diffuses from the plasma bulk into the sheath region, it will then be accelerated toward the substrate, which it strikes with a maximum kinetic energy $E_{i,max}$ [21–23]:

$$E_{i,max} = e|V_p - V_B| + \Delta E/2 \tag{9.2}$$

The last term is due to the periodic modulation of the sheath voltage. At low excitation frequency $\Delta E \approx 2\ V_{AC}$, while for the high f values this term is inversely proportional to the number of RF cycles needed for the ion to pass through the sheath. This leads to the fact that for the ions originated from the same plasma, the maximum energy they gain in the sheath can be almost two times higher for the light ions (e.g. H^+) than for the heavy ones (e.g. $TiCl_4^+$). In the pressure range generally used for plasma processing, the ions lose part of their energy owing to elastic and inelastic (e.g. charge transfer) collisions in the sheath, and exhibit an ion energy distribution function (IEDF), discussed in more detail in Section 9.4.

In conclusion, the processes leading to the deposition of thin films in the plasma environment include reactions in the gas phase, transport toward the surface involving specific energetic considerations, and reactions at the surface, giving rise to film formation and microstructural evolution, providing specific film functional properties (as indicated in Figure 9.2). Energetic aspects of plasma–surface interactions and the importance and ranges of ion and photon energies, particularly of the ultraviolet (UV) and vacuum ultraviolet (VUV) radiation, are discussed in Section 9.4.

9.3 PECVD Reactors and Deposition Concepts

9.3.1 General Considerations

Plasma deposition equipment usually consists of six modules or functions: its main part is the reactor chamber, completed by the pumping system, power supply and monitor, electrical

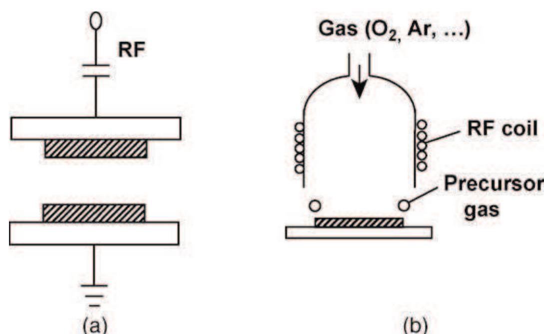

Figure 9.4: Schematic illustration of the reactor configurations of low-, mid- and radio-frequency PECVD systems: (a) parallel plate plasma reactor; (b) downstream (remote) RF inductively coupled plasma reactor.

matching network, process control and instrumentation, and process diagnostics. While most of the modules are similar for all PECVD and in many cases for PVD processes, they differ principally by the reactor configuration and the power supply modules, depending on the range of plasma excitation frequency, the nature of the substrates, and film quality requirements. In the following, we describe systems that have been successfully applied for the fabrication of PECVD functional coatings, some of which form the basis for industrial plasma equipment.

9.3.2 Low-, Medium- and Radio-Frequency Plasma Reactors

Low-, medium- and radio-frequency (LF, MF, RF) deposition systems can all possess internal electrodes, while the RF reactors can also use external plasma excitation using a coil or rings, as illustrated in Figure 9.4. This allows one to distinguish them based on the level of control of the bulk plasma characteristics and ion bombardment effects. The RF systems depicted in Figure 9.4 are similar to those frequently used in microelectronics for PECVD and reactive ion etching (RIE) [2, 3]. The r_D values on the grounded electrode are substantially lower than on the RF-powered electrode (usually 5–10 times) depending on the gas nature and composition. Typically, $E_{i,max} = 25$ eV on the grounded electrode (Eq. 9.2), while on the RF-powered electrode, E_i values may reach several hundred electron volts owing to high V_B.

9.3.3 Microwave and Dual-Mode MW/RF Plasma Systems

Many successful deposition systems for functional (mostly dielectric) coatings are based on the use of MW discharges that generally provide high n_e and hence high Φ_i values (Figure 9.5). In a single-mode MW reactor (Figure 9.5a–e), the substrate is placed on a grounded or electrically floating substrate holder, facing a MW (low water-content fused silica or alumina) window through which the MW power is supplied using different MW applicators [11, 24].

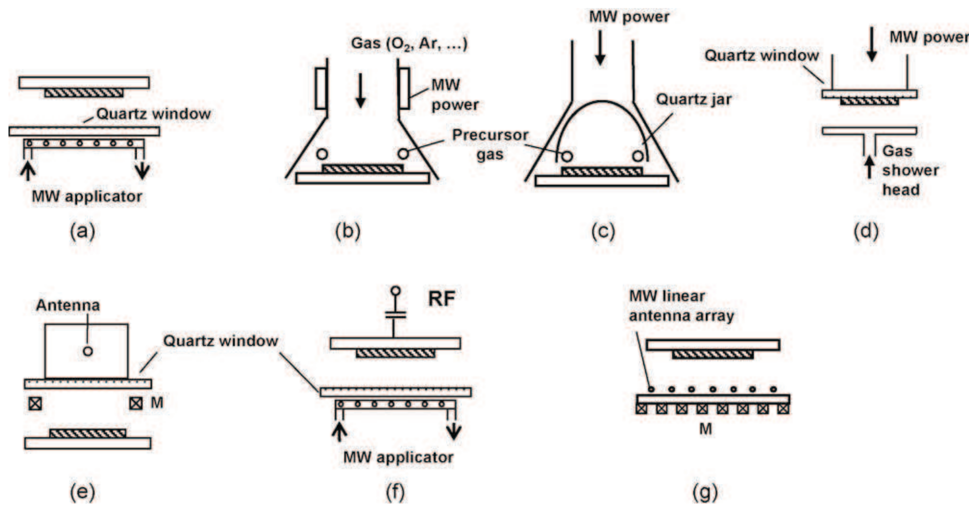

Figure 9.5: Schematic illustration of the reactor configurations of microwave frequency PECVD systems with different modes of excitation: (a) linear applicator; (b) remote MW excitation; (c) horn antenna; (d) plasma impulse CVD (PICVD); (e) electron cyclotron resonance (ECR); (f) dual-mode MW/RF; (g) distributed antenna array combined with ECR (DECR) (M indicates magnets).

Pulsed MW plasma with low pulsing frequency (f_p of about 100 Hz) and a low duty cycle ($D \leq 0.1$) have become prominent for optical and other functional coatings. This process has achieved a high level of sophistication at Schott Glaswerke GmbH (Mainz, Germany; see Figure 9.5d) [25, 26]. In their 'plasma impulse' chemical vapor deposition (PICVD) process, the dielectric substrates are placed directly on the MW window; in such a case, at a relatively high pressure on the order of 1 torr, very dense plasma is formed near the substrate during a very short pulse (typically 1–100 ms in duration).

A dual-mode MW/RF plasma approach has been developed at École Polytechnique in Montreal [18, 27, 28] (see Figure 9.5f) and also used by others [29, 30]. The substrates are placed on the RF-powered substrate holder facing the MW window, through which the MW power is applied with different types of linear applicators: slow wave structure, slotted waveguide, or surface wave launchers have been considered and tested [11, 24].

Other concepts include remote MW/RF reactors [29, 30] and electron cyclotron resonance (ECR) configurations (e.g. distributed ECR (DECR) [31] or integrated distributed ECR [32]), in which magnetic field is applied in conjunction with the MW discharge in order to further increase n_e and hence the dissociation rate (Figure 9.5e, g).

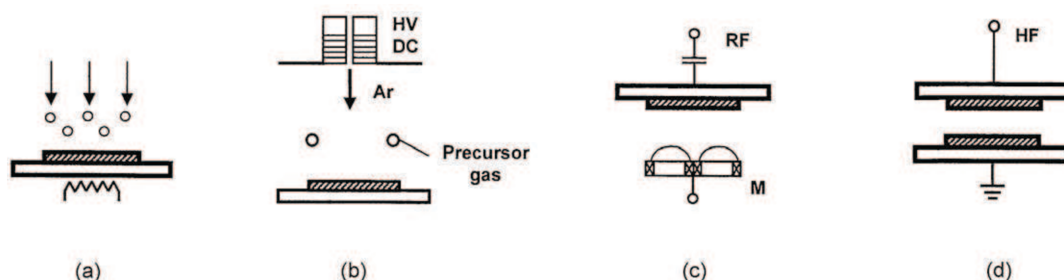

Figure 9.6: Schematic illustration of the reactor configurations using different modes of operation: (a) atomic layer deposition (ALD) or CVD; (b) cascade arc; (c) hybrid PECVD/PVD system combining a parallel plate RF electrode and magnetron sputtering; (d) atmospheric pressure plasma.

9.3.4 Complementary Plasma Systems

In addition to the basic configuration employing the thermal CVD technique (typically 300–800 °C) and the RF- and MW-based systems, there has been significant interest in novel complementary deposition approaches for functional coatings from a precursor gas or vapor using plasma enhancement alternatives; these include:

- The plasma-assisted atomic layer deposition (ALD) (Figure 9.6a) process in which the coatings are grown by sequentially introducing ‘pulses’ of a precursor; the final film then grows layer by layer, generally providing high surface conformity, very smooth surfaces, and other beneficial characteristics [33, 34].
- Cascade arc PECVD (Figure 9.6b), in which plasma of a carrier gas is excited in a series (cascade) of high-voltage arc electrodes. In such a system, developed at the Eindhoven University of Technology [35, 36], the activated gas expands at ultrasonic speed into a vacuum. On its way toward the substrate it dissociates, and activates precursor molecules that contribute to the film growth.
- Hybrid deposition systems benefit from the possibility of combining, in one reactor, both the PECVD and PVD approaches, such as illustrated in Figure 9.6c for the particular case of RF-PECVD and magnetron sputtering (or evaporation) [37]. This allows one to fabricate different coating architectures including multilayers or graded layers, or doped or nanostructured (nanocomposite) coatings with specific optical, mechanical, and other characteristics [38, 39].
- Much progress has recently been made in the development of APGD suitable for surface treatment [40] and explored for PECVD [9, 10] (Figure 9.6d). The system can be thought of as a capacitor, where one of the electrodes is covered with a layer of dielectric material (e.g. ceramic or glass). The high-voltage power supply, which

causes breakdown in the interelectrode gap, typically operates in the frequency range from 10 to 30 kHz. The pulseless (glow) discharge then has to be operated under specific conditions related to the choice of gases, power levels and frequency, in order to avoid corona (dielectric barrier discharge or silent discharge), which consists of a multitude of filamentary microdischarges [41, 42].

9.4 Process Diagnostics and Monitoring

9.4.1 Diagnostic and Monitoring Techniques

As indicated above, the relations between the external PECVD parameters available to the operator and the resulting film properties are rather complex. If we are to understand, control, and optimize the processes taking place inside the reactor, knowledge of internal parameters (such as particle generation, their flow and energies) is essential. The diverse plasma diagnostic techniques provide the possibility of accessing this information and developing understanding of the general process rules and interrelationships between input parameters and plasma characteristics, as well as the particularities of each PECVD system (Table 9.4).

The plasma bulk diagnostic techniques can be classified in many ways; for example; (1) by the particles they measure (electrons, ions, radicals, photons, etc.); (2) by being active (introducing additional signal into the system like a laser beam in laser-induced fluorescence (LIF) or external voltage in Langmuir probes); (3) by being passive (sampling neutrals in mass spectrometry or emitted light in optical emission spectroscopy (OES)); or (4) by the parameters they can help to assess (n_e, n_R, etc.). An extensive literature describing principles and applications of different techniques is now available [43–46]. In addition, the list of available tools is completed by numerous techniques available for monitoring the film growth process directly on the substrate surface, and they are related to the films' mass/density, optical, electrical, and other properties [47–49].

The most popular techniques, the parameters detected, and other characteristics are summarized in Table 9.4. One of the most persistent problems in using diagnostics in any PECVD system is contamination of the electrical or optical components by the deposited films; this can substantially reduce precision, lead to artifacts, or even render the measurements impossible. The ways of dealing with such problems depend on both the technique and the process. There exist numerous possible solutions to such difficulties; including the use of shutters (opened only during the short period of the measurement itself); long inert gas purges; use of collimators with diaphragms to minimize deposition on windows and lenses; application of high positive or negative voltages to the electric (Langmuir) probes to heat-evaporate or to sputter-remove the accumulated film, and other approaches [43–45, 50–52].

Table 9.4: Diagnostic methods and their capabilities suitable for advanced analysis and control of PECVD processes

Diagnostics method	Measured parameters	Derived characteristics	Perturb the plasma	Time resolution	Space resolution	Cost	Contamination a problem	Advantages	Shortcomings/ comments
(a) Plasma bulk									
Langmuir probes	*I–V* characteristics; ion and electron currents	n_e, T_e, V_p, λ_D, EEDF	Slightly	10^{-5} s	5 mm	$–$$	+++	Simple instrumentation	Complex interpretation
Mass spectrometry	Mass-selective intensity	Concentrations of atoms, molecules, and fragments	Slightly	10^{-3} s	1 cm	$$–$$$	++	Many species, straightforward	Differential pumping, short-lived species
Ion energy analysis	Ion current	IEDF	Slightly	10^{-4} s	1 cm (0.1 mm)	$	+++	Direct ion flux	No mass resolution
Optical emission spectroscopy	Spectrally resolved emission intensity	Concentrations of atoms, molecules, and fragments; vibrational and rotational temp., partial info. on EEDF	No	10^{-9} s	1 mm × 10 cm	$-$$$	+	Easy to set up	Indirect, convoluted interpretation
Absorption spectroscopy	Spectrally resolved absorption	Concentrations of atoms, molecules, and fragments	No	10^{-9} s	1 mm × 10 cm	$$$	+	Access to radical densities	Bulky, limited set of species
Laser-induced fluorescence	Induced light intensity	Concentrations of atoms, molecules, and fragments	No	10^{-9} s	1 mm × 10 cm	$$$	+	Access to radical densities	Bulky, limited set of species
Plasma impedance	Current, voltage, phase shift	Resistance, capacitance, n_e	No	10^{-3} s	None	$	–	Simple	Indirect, convoluted interpretation
(b) In situ real-time film growth monitoring									
Quartz crystal microbalance	Vibration frequency	Mass, d, r_D, density (indirect)	Slightly	1 s	1–5 nm	$	–	Simple	Sensitive to heating and to electric fields
Interferometry	Light intensity in transmission or reflection	d, n, r_D	No	10^{-3} s	1–5 nm	$–$$	+	Simple	Single wavelength or multiwavelength; transparent films
Spectroscopic reflection/transmission	Spectrally resolved light intensity	d, n, r_D	No	10^{-3} s	1–5 nm	$$	+	Wide range of λ	Partially transparent films
Spectroscopic ellipsometry	Ellipsometric angles $\Psi(\lambda)$ and $\Delta(\lambda)$	d, n, k, r_D	No	10^{-1} s	0.2 nm	$$$	+	Precise assessment of n and k in a wide range of λ	Costly, only for at least partially transparent films
Resistivity	Current, resistance	d	No	10^{-3} s	Depends on knowledge of the resistivity	$	–	Simple	Only for conductors, affected by electric fields

9.4.2 Plasma Characteristics of PECVD Processes and Energetic Aspects of Thin Film Growth

Key parameters that influence the film microstructure in low-pressure, low-temperature deposition processes are E_i and Φ_i. In the PECVD process these are most frequently controlled by the choice of excitation frequency (RF vs MW), or by applying pulsed direct current (DC) or RF-induced negative substrate bias, V_B (see Section 9.3). The IEDF can be evaluated in the process chamber using a multigrid electrostatic ion energy analyzer (IEA) [53] or a quadrupole mass spectrometer integrated with an IEA [54, 55].

Examples of IEDFs in different PECVD systems in nitrogen are shown in Figure 9.7. In a parallel plate RF (13.56 MHz) system, with a discharge in N_2 at 40 mtorr, the E_i value at the grounded substrate holder is around 15 eV (Figure 9.7a) owing to the fact that typically $V_p = 20–25$ V, while E_i can reach many hundreds of eV on the capacitively coupled RF-powered electrode (Figure 9.7d). In the latter case, the IEDF is structured due to sheath modulation [21]. In fact, the IEDFs, n_e, V_B, and V_p values in PECVD are very similar to those encountered in magnetron sputtering and RIE.

MW plasmas usually yield high r_D, Φ_i, and n_e values, and high dissociation rates. In a simple MW reactor, a typical value of V_p is 10 V, generally yielding E_i of approximately 5–10 eV such as in the continuous wave (cw) mode in N_2 (Figure 9.7b). In such MW plasmas, two approaches can be used to control E_i and Φ_i, pulsed-mode discharges and RF-induced surface biasing (dual-mode or dual-frequency MW/RF plasma deposition). In pulsed MW plasma which is frequently used, two plasma regimes can be distinguished during each pulse cycle: high-density plasma during the T_{on} period, and decaying plasma during the T_{off} period. As a consequence, the IEDF adopts a bimodal shape (Figure 9.7c), with the high-energy peak corresponding to ions generated during the T_{on} period, and the low-energy peak being due to ions arising from the T_{off} period [53]. The ratio of the peak intensities depends on the duty cycle $D = T_{on}/(T_{on} + T_{off})$. This permits tuning of the plasma–surface interactions in deposition, as well as in etching or surface modification processes.

The possibility of selectively controlling E_i and Φ_i values over a large range is illustrated by the IEDFs in the dual-mode MW/RF discharge (Figure 9.7e, f). The effects of such control on adjusting film microstructure and, hence, specific properties and functional and device characteristics is discussed in more detail in Section 9.5.

Appropriate control of ion bombardment energy ($E_i < 1$ keV) is particularly important in the context of the deposition of thin films at low substrate temperature, T_S. Film growth, while under ion bombardment, leads to growth-related effects such as interfacial atom mixing, high surface mobility (diffusion) of deposited species, resputtering of loosely bound species, and deep penetration of ions below the surface, leading to the displacement of atoms (forward sputtering or knock-in effects) [3, 58]. Such phenomena give rise to the disruption of growth

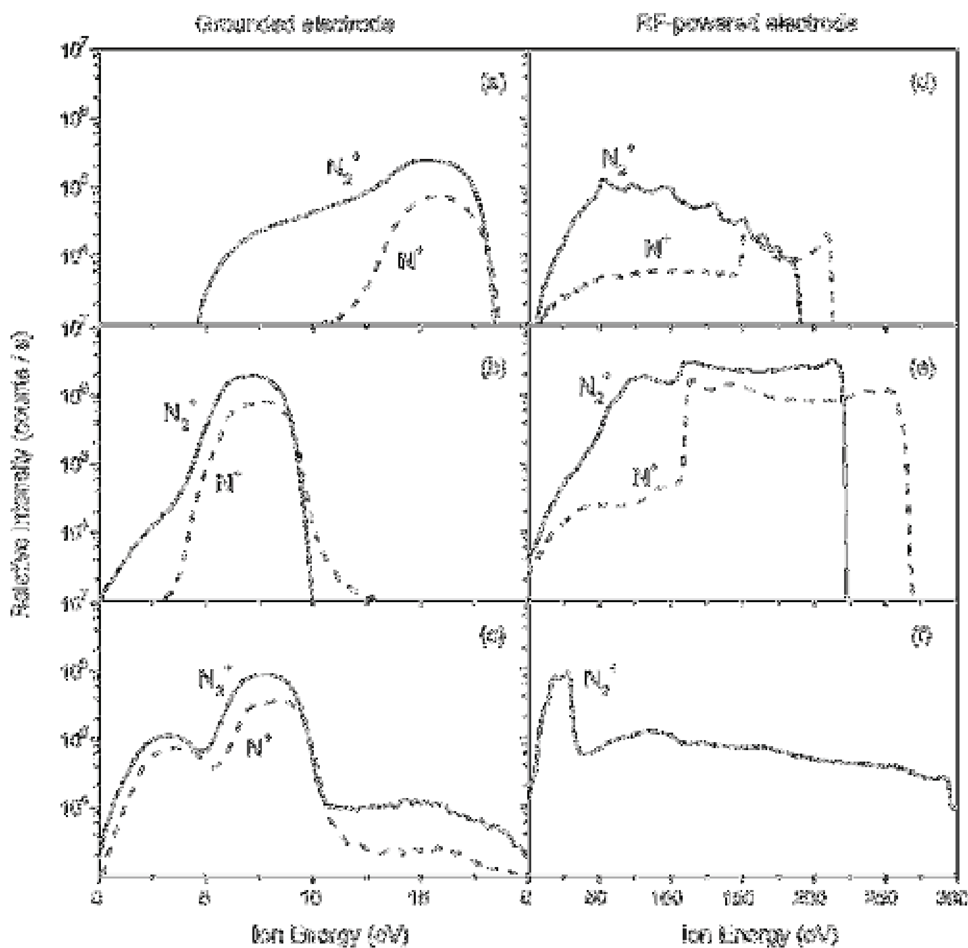

Figure 9.7: Examples of the IEDFs of N_2^+ and N^+ ions in high-frequency plasmas in nitrogen at 40 mtorr measured in the following configurations and detection positions: (a) grounded electrode in (continuous wave) cw-RF discharge such as in the reactor from Figure 9.4(a) ($V_B = -150$ V); (b) grounded electrode in cw-MW discharge such as in the reactor from Figure 9.5(a) ($P_{MW} = 300$ W); (c) grounded electrode in a pulsed MW discharge in the reactor from Figure 9.5(a) ($P_{MW} = 300$ W, pulse frequency = 1 kHz, duty cycle = 0.5); (d) RF-powered electrode in a cw-RF discharge such as in the reactor from Figure 9.4(a) ($V_B = -150$ V); (e) RF-powered electrode in the dual-mode cw-RF/cw-MW discharge in the reactor from Figure 9.5(f) ($V_B = -150$ V, $P_{MW} = 300$ W); (f) RF-powered electrode in the dual-mode cw-RF/pulsed-MW discharge in the reactor from Figure 9.5(f) ($V_B = -150$ V, $P_{MW} = 300$ W, pulse frequency = 1 kHz, duty cycle = 0.5). (Adapted after [55–57].)

nuclei, to the suppression of columnar structure, and hence to material densification. This is in agreement with the so-called structure zone model (SZM) first proposed by Movchan and Demchichin [59], improved by Thornton [60] and Messier et al. [61, 62], and finally refined by Kelly and Arnell [63].

Various approaches to quantitative description of ion bombardment have been taken. It appears that a key parameter for representing these effects is the energy E_P delivered to the growing film per deposited particle [64]:

$$E_{P(Ts=const)} = (E_i\ \Phi_i + E_m\Phi_m)/(\Phi_n + \Phi_r) \sim E_i\ (\Phi_i/\Phi_n), \qquad (9.3)$$

where E denotes energy; Φ the particle flux; and the indices i, m, n, and r refer to ions, neutrals, condensing precursor species, and trapped inert gas, respectively. As a first approximation, one can neglect Φ_r compared to Φ_n and $E_m\Phi_m$ compared to $E_i\Phi_i$, and obtain the simplified relation in Eq. (9.3). Such an approximation is clearly possible in ion beam experiments; however, the energy flux of neutral particles may become significant in PECVD because a certain fraction of the initially accelerated ions become neutral due to charge transfer collisions in the sheath region. Detection of neutral species and determination of their energy is difficult, requiring careful measurements, using mass spectrometry combined with ion energy analysis [54, 55].

It has been proposed that there exist critical ion energies, and critical ion flux ratios ($E_{i,c}$ and $(\Phi_i/\Phi_n)_c$), which can be associated with transitions in the evolution of film microstructure and properties [18, 65]. Clearly, E_P in Eq. (9.3) can be adjusted to the same level by combining low and high E_i and Φ_i/Φ_n values. However, experience suggests that good-quality (dense, hard, chemically stable, low-stress) films are obtained under conditions of low (10–50 eV) or intermediate (about 100 eV) ion energies, sufficient for densification ($E_i \sim E_{i,c}$), but using high Φ_i. This reduces microstructural damage and gas entrapment, generally yielding low values of stress. High fluxes are highly advantageous, especially when one aims at achieving high r_D (>10 nm/s).

In Figure 9.8 the $E_{i,c}$ and $(\Phi_i/\Phi_n)_c$ values for PECVD SiO_2, Si_3N_4, TiO_2, and *a*-C:H films have been compared with the compilation of literature data by Harper et al. [65], who summarized examples of $E_{i,c}$ and $(\Phi_i/\Phi_n)_c$ values reported to be necessary for property modification in numerous materials deposited by different (non-PECVD) ion-assisted techniques. It was concluded that the $E_{i,c}$ values are lower, and $(\Phi_i/\Phi_n)_c$ values are higher for MW and MW/RF PECVD processes than for most other techniques. The energetic conditions leading to good-quality films obtained by the PICVD process also fall within the same energy limits, that is low E_i ($E_i < 10$ eV) but high Φ_i/Φ_n ($\sim$ 1–10) values, due to a high plasma density and ionization rate [25]. In this context, to derive appropriate relations between E_i and Φ_i/Φ_n, and to benefit from the availability of experimental data, one can apply the conversions for the experimentally measured ion current, where 1 mA/cm^2 corresponds to 6.25×10^{15} ions/cm^{2}s,

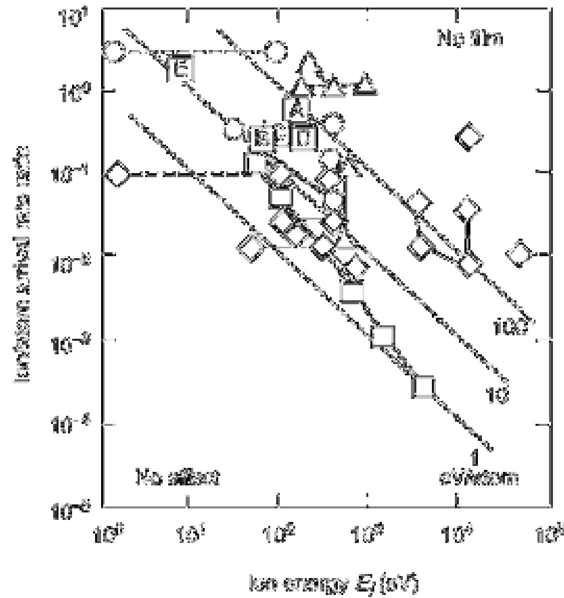

Figure 9.8: Plot of critical ion/condensing particle arrival rate ratios $(\Phi_i/\Phi_n)_c$ vs critical ion energy $(E_i)_c$, required for film structural modification, particularly densification: (A) $SiN_{1.3}$:H; (B) SiO_2:H; (C) *a*-C:H; (D) TiO_2 obtained from MW/RF plasma; (E) estimated for TiO_2 obtained in a PICVD discharge based on the data in [25]. Other data points are from [65] for different materials obtained by PVD techniques: (◯) SiO_2, (△) other dielectrics, (□) metals, (◊) semiconductors. (After [7].)

and a useful relation [66]:

$$\Phi_n = r_D \rho N_A / m \tag{9.4}$$

where N_A is Avogadro's constant and ρ and m are the density and the molecular mass, respectively, of the material.

We conclude from Figure 9.8 that for most materials, energy may range from several to several hundreds of electron volts per particle [58]. These relatively high E_P values were obtained as a result of process and materials optimization, and point to the trend in recent deposition techniques, favoring lower E_i and high Φ_i [7, 66]. In addition, E_P appears to be higher for materials with a higher melting point, in agreement with the SZM. This rather simplified approach does not take into account the fact that, at a relatively high pressure, considerable energy is also delivered to the growing surface by energetic neutrals, as indicated in the full Eq. (9.3) [67].

The role of ion bombardment and the possibility of predicting its effect on the characteristics of individual films, of the interfaces, and on the performance of the thin film systems and

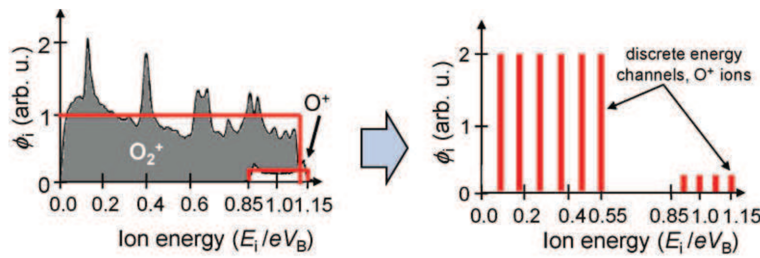

Figure 9.9: IEDF on the RF-powered electrode in a discharge in oxygen and its conversion into energy channels suitable for dynamic Monte Carlo simulations. (After [68].)

related coating architectures can also be assessed by complementary approaches, such as by dynamic TRIDYN Monte Carlo simulations combined with in situ real-time spectroscopic ellipsometry (RTSE) [68, 69]. These have shown that ion- and plasma-assisted deposition processes in the range of tens to a few hundreds of electron volts lead to thin film growth dominated by subsurface deposition, as a result of subplantation (shallow implantation).

As an example for the particular case of PECVD in an O_2-rich plasma at the RF-biased electrode, the experimentally determined IEDF has been modeled as shown in Figure 9.9. This distribution was divided into multiple channels (ten in this particular case), and the effect of ions on the structural changes has been simulated up to an experimentally relevant fluence (e.g. 10^{18} ions/cm^2, corresponding to a typical deposition duration). Such interactions were shown to predict very accurately the thickness of interfacial layers, depending on the Φ_i/Φ_n value (see Section 9.5.5).

RTSE measurements can be used for the study and monitoring of ion bombardment and thin film growth effects without perturbing film growth [47, 48]. As an example, evolution of the real ε_1 and imaginary ε_2 parts of the permittivity of superhard nanocomposite nc-TiN/SiN and nc-TiCN/SiCN coatings is illustrated in Figure 9.10. One can distinguish various regions corresponding to different surface phenomena during film deposition, including pumping (surface desorption) and substrate heating (actual surface temperature can be determined from the shift of the temperature-sensitive substrate parameters – region) beginning of actual film growth (region II), (until the film becomes opaque for the RTSE system wavelength range (region III)), and, finally, system cool-down and possible post-deposition surface interactions (region IV). Analyzing the behavior of the ε_1 and ε_2 values, one can make conclusions with respect to the film's optical, electrical, compositional, and microstructural characteristics (for more detail, see Section 9.5.4) [70].

As a complement to ion bombardment during the film growth, one should also consider another source of energetic plasma–surface interactions, namely photons in the entire range from infrared (IR) and visible to UV, VUV and soft X-ray regions (for a review, see [71]). In

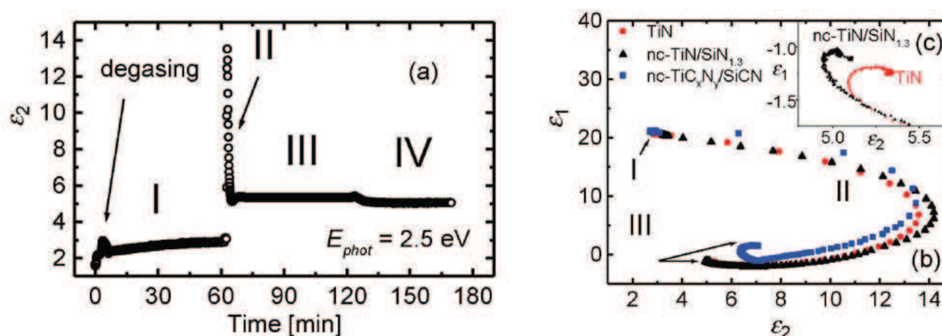

Figure 9.10: Evolution of the ellipsometric parameters during the growth of superhard nc-TiN/$SiN_{1.3}$ and nc-TiCN/SiCN films. The curves pertain to a wavelength of 500 nm (photon energy: 2.5 eV): (a) imaginary part of the permittivity as a function of time during the fabrication process; (b) ε_1 vs $_2$ plot of the real and imaginary parts of the permittivities during the film growth; (c) detail of the ε_1 vs ε_2 plot at a moment when the films become thick. (Modified after [70].) See text for more details.

particular, VUV photons play an important role in the interaction with organic (polymer) surfaces, since their energy, of more than 10 eV, can break any chemical bond. Of considerable importance in active plasmas is the radiation in discharges containing hydrogen with its strong Lyman line at 121 nm and intense molecular bands, oxygen with its strong resonant line at 130 nm and helium (intense lines at 57 nm and above), which are particularly effective (Figure 9.11) [11, 13]. In this context, intense VUV features due to the excitation of different

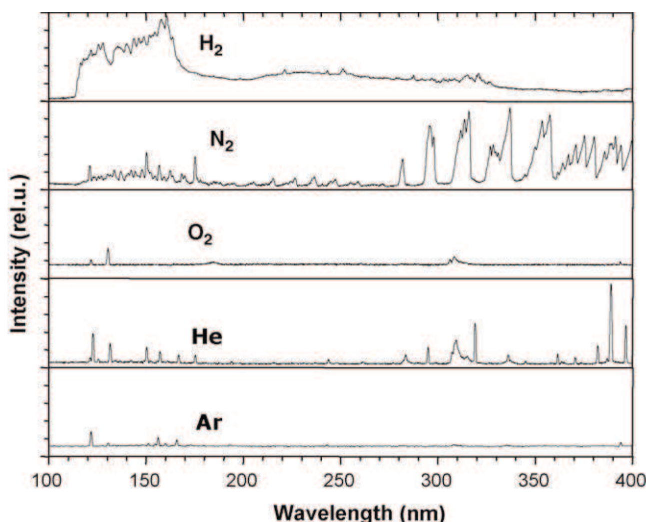

Figure 9.11: Vacuum ultraviolet (VUV) spectra emitted from glow discharges in different gases. (After [72].)

discharge components including impurities (fragments of H_2, SiH_4, CH_4, H_2O, hydrocarbons, and others) desorbed from chamber walls and from polymer substrates may be very important, and can play a significant role in controlling the characteristics of polymer surfaces and of coating–polymer interfaces (see Section 9.5.6).

9.5 PECVD Materials: Effect of Surface Processes on the Microstructure and Properties

Numerous PECVD functional coating materials have been investigated and considered for a large number of applications, and some of them are now applied on an industrial scale. Since there already exists a vast literature on this subject, we specifically focus in this section on coatings studied for their functional (or multifunctional) character, for various applications outside electronics. We particularly show examples of films for which there exist complete sets of microstructural, compositional, and functional characteristics, in close relationship with the energetic aspects of film growth, outlined in the preceding section. First, we introduce the most frequently used characterization methods (Section 9.5.1), and then provide examples of effects of deposition conditions on film characteristics.

For simplicity, we divide the materials described into four categories:

- silicon-based (inorganic) coatings (Section 9.5.2)
- carbon-based coatings and related covalently bonded materials (Section 9.5.3), including organic PECVD films such as plasma polymers
- metal-based PECVD coatings, including nanocomposites which exhibit superhardness and non-linear optical properties (Section 9.5.4)
- interface engineering aspects of film deposition onto various technologically important substrates (Section 9.5.5).

9.5.1 Characterization Methodology Specific to PECVD Coatings

Throughout this chapter, we frequently refer to film characteristics obtained by different, complementary, techniques which provide detailed information about the microstructure, composition, and properties of PECVD films. We comment on certain methodological issues that should be considered in the interpretation of results.

The microstructure of PECVD coatings is most often assessed by scanning electron microscopy (SEM), transmission electron microscopy (TEM), and X-ray diffraction (XRD), which are used to identify crystalline phases, lattice parameters, average crystal size, and surface roughness, the latter also frequently determined by atomic force microscopy (AFM). Chemical composition of the films, particularly the compositional depth profiles, is studied by

elastic recoil detection in the time-of-flight regime (ERD-TOF) [73]. This technique allows one to establish quantitative data without standards. Moreover, ERD can quantify H concentration, [H], which is of primary importance for PECVD coatings, which are most often fabricated in hydrogen-containing environments. Complementary techniques include Auger electron spectroscopy (AES), X-ray photoelectron spectroscopy (XPS), and IR and Raman spectroscopies, used to evaluate chemical composition, chemical bonding, and short- and medium-range microstructure (for a review, see e.g. [74–76]).

Optical properties are determined either from spectrophotometric (reflectance, R, and/or transmittance, T) or ellipsometric measurements, among which variable angle spectroscopic ellipsometry (SE or VASE) combined with R and T data appears to be most powerful (for a review, see [7]). Ellipsometry deals with determination of the relative phase change of a reflected polarized light beam, as opposed to absolute intensity measurements in spectrophotometry, making it more sensitive to very small changes in the optical properties at the surface of the sampled material. Spectrophotometry is more appropriate when evaluating the performance of a coating system, such as an optical filter. For postprocess characterization (sometimes called reverse engineering), the two methods share the same difficulties, related to the optimization algorithms and models used for reproducing the measured data.

The most frequently used dispersion models for dielectric films are the semi-classical Sellmeier and Cauchy relations for the refractive index $n(\lambda)$ [77], and the Urbach tail relation for the extinction coefficient $k(\lambda)$ [78]. Recently, new dispersion relations, such as the Forouhi–Bloomer [79] and Tauc–Lorentz formulae [80], based on a simplified expression for $k(\lambda)$ due to allowed electronic transitions in solids, have been shown to work well for PECVD materials.

Effective medium approximation (EMA) models are frequently applied to account for index inhomogeneities, and to estimate porosity, surface roughness, or other microstructural features [81, 82]. The use of EMA is justified only when the scale of the inhomogeneities is much smaller than the wavelength of the probing light ($< \lambda/10$). The scale of the Bruggeman EMA is used for a heterogeneous medium with components of small size, randomly distributed, while the Maxwell–Garnett model is more appropriate when one of the components surrounds the others, and acts as a host material [83].

Components of the EMA models must be chosen with care to reflect the real composition of the material (sometimes including voids, or an optically absorbing phase, such as *a*-Si). However, one may question the utility of both the Maxwell–Garnett and Bruggeman EMA when the inhomogeneity is on the atomic scale; this applies to solid solutions such as SiO_xN_y films, or when dopants and impurities are present (H, F, Cl, C, etc.), in which cases no particular phases with bulk dielectric response can be identified [84].

Reliable determination of the optical properties is generally based on the (mostly non-global) fit optimization. In such situations, it is very important to have a good starting 'guess' for n, k,

and the thickness, d. In the case of single-layer films for which one has no a priori knowledge of n and k, the optical characteristics can also be obtained from envelope methods which provide analytical expressions for n, k, and d as a function of T or R. For more detail, see the discussion in [7].

Mechanical characterization, to determine hardness, H, reduced Young's modulus, E, and other elastoplastic properties, is frequently performed by depth-sensing indentation, and analyzed by the method of Oliver and Pharr [85]. The intrinsic stress given by the internal structure of the material (in particular, structural defects like macroscopic voids, gas entrapment, or phase transformation) is measured by the curvature of the substrate, before and after film deposition, and calculated from the Stoney formula [76, 86]. The curvature is assessed by mechanical or optical profilometry, or by interference measurements. The wear coefficient, K, and friction coefficient, μ, characterizing the tribological behavior of the coatings, are usually determined by pin-on-disk tribometry. Different tests exist for determining adhesion: these include qualitative (peel test) and semi-quantitative (scratch test) approaches [87, 88].

Corrosion resistance is usually determined qualitatively by evaluating the surface morphology after exposure to a corrosive medium, or quantitatively by measuring the corrosion current or open circuit potential (OCP) [89]. Recently, tribocorrosion properties have been assessed in real time by simultaneously performed OCP and wear measurements [90]. The corrosion mechanism, and especially its relationship with microstructure, can be determined by electrochemical impedance spectroscopy (EIS), in combination with appropriate equivalent electrical models [89].

Complementary to the optical and tribomechanical characterization above, basic electrical testing of PECVD functional (usually dielectric) films is performed in a sandwich metal–insulator–metal (MIM) structure to determine DC resistance, ρ_E, dielectric loss tangent (tan δ) or permittivity, ε, breakdown voltage, leakage current and other electrical properties. For conductive films, ρ_E and carrier mobility are assessed by the four-point method and by Hall effect measurements [76, 91].

The basic optical and mechanical properties of the most frequently studied PECVD films are summarized in Figure 9.12, where they are compared with those of their PVD counterparts and of the most often used substrates. Each of the characteristics exhibits a certain range of values, related to the fabrication conditions and, hence, to the microstructure and composition, a subject of the following sections.

9.5.2 Silicon-Based (Inorganic) Coatings

Silicon compound films have been studied for many decades, because of their use in microelectronics, microelectromechanical systems (MEMS), optics and photonics, photovoltaics, and other areas. PECVD Si-based films are generally amorphous, and contain

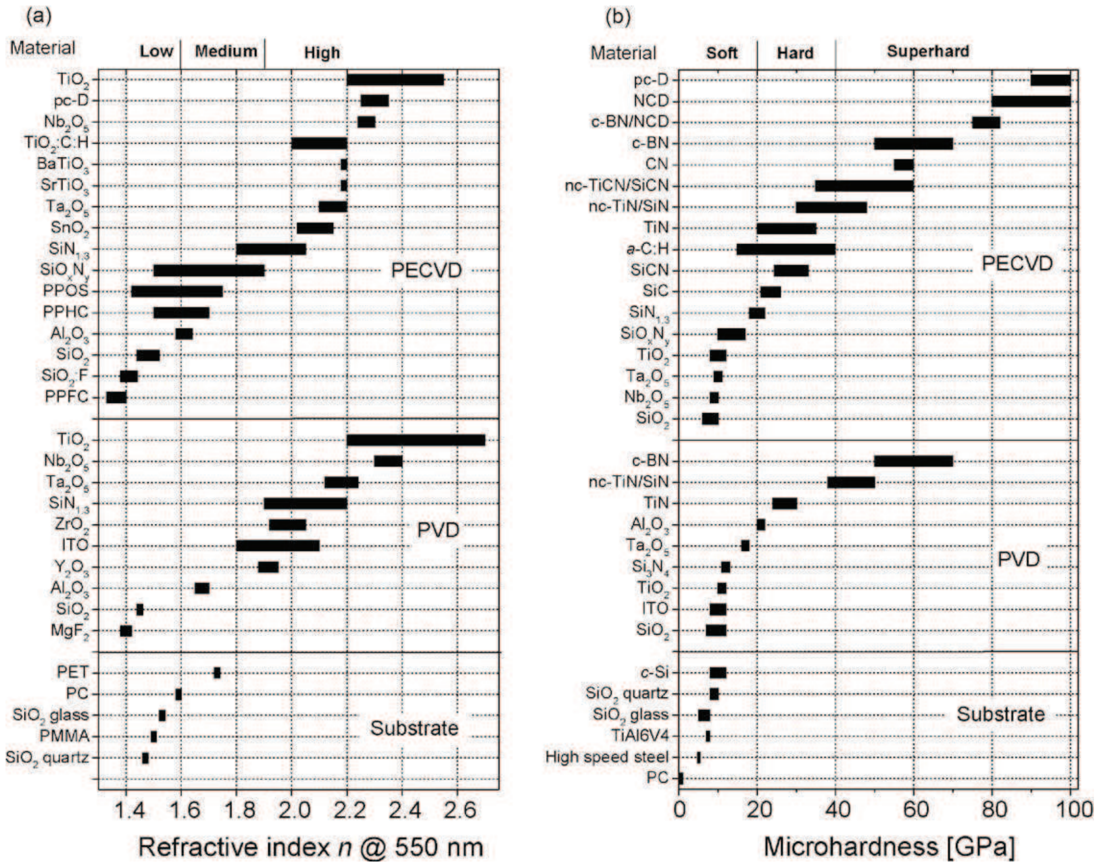

Figure 9.12: Physical properties for the most frequently studied PECVD films: (a) refractive index of transparent films; (b) microhardness. PVD films and often used substrates are shown for comparison.

considerable amounts of hydrogen, owing to the use of precursor gases such as silane (SiH_4) and different organosilicones (OS). The most frequently applied systems include hydrogenated amorphous silicon (*a*-Si:H), silicon oxide (*a*-SiO_2:H), silicon nitride (*a*-Si_3N_4:H), silicon oxynitride (*a*-SiO_xN_y:H), and silicon carbide (*a*-SiC:H). In the following, we focus particularly on functional silicon compound films. For simplicity, we apply an abbreviated nomenclature, namely SiO_2, $SiN_{1.3}$, SiON, SiC, and SiCN. The reader may consult other reviews dealing with amorphous, polycrystalline, crystalline and porous silicon, and related materials and their fabrication, properties and applications [2, 92].

9.5.2.1 Silicon Dioxide

Among all dielectric and silicon-compound coatings, SiO_2 is probably the most studied PECVD material. It is typically deposited from a mixture of SiH_4 and O_2 or N_2O. Both

theoretical and experimental studies of the various phases of SiO_2 underline the link of the film characteristics, such as n, optical gap, E_g, and others, to microstructure, in particular the Si–O–Si mean bond angle, θ, density, and H incorporation [2, 93]. In amorphous SiO_2, changes in θ values can be estimated experimentally from IR spectra of the Si–O–Si stretching mode at $2260\,cm^{-1}$. A small θ value is related to a stressed network in a dense structure.

Small-angle Si–O–Si bonds are very unstable. They can be broken by an accumulation of stress in the film and force the network to relax, leading to a more flexible structure, accompanied by the formation of defect centers, or by reaction with water [94]. In the latter process, water absorption in pores may not necessarily be associated with aging, since not all types of pores give rise to water sorption, but the concept of 'open' and 'closed' pores and their size should be considered [95].

In SiO_2 deposition from SiH_4/O_2 mixtures, the O_2 flow rate is typically twice that of silane, or more, depending on the plasma conditions. Nitrous oxide (N_2O) is frequently used to replace O_2, since the chemical bonds in N_2O break more easily, leading to higher r_D (activation energy, $E_a = 2.5$ eV/molecule in N_2O [96] compared to $E_a = 6.5$ eV/molecule for O_2 [97]). The use of N_2O can introduce some N impurities; however, [N] is usually less than 3 at.% owing to the high affinity of Si with O, and even smaller if the film is produced using ion bombardment or is heated. The use of He has been shown to reduce the number of Si–H, Si–N, Si–OH, and N–H bonds in SiO_2 made from SiH_4/N_2O mixtures [98].

SiO_2 usually contains 5–15 at.% of hydrogen, mostly in the form of –OH, which has an effect on the optical and other properties, and on the stability of the material. It has been shown that during deposition from a SiH_4/O_2 mixture, the surface of the growing oxide is initially covered with silanol (SiOH) [99], owing to instant oxidation of SiH_x by atomic oxygen. The SiH_x groups react further with SiOH and Si–O–Si to yield H_2O and Si–O–SiH_x, which is oxidized by neutral O, leading to superficial–SiOH terminations.

O_2^+ bombardment seems to be particularly efficient for reducing [H] in the film [99]. When the dissociation of SiH_4 is high, Si exists on the surface, and it is easily oxidized, compared with SiH_2 and SiH_3 groups, for which several reactions with oxygen are needed to release all the H atoms. This means that high n_e (high discharge power) can reduce H concentration, such as in ECR [100], MW, or MW/RF [18] plasmas.

An important problem with silane as a precursor is the formation of particles. It can react with traces of humidity in the gas line and form powder that can reach the chamber, and clog valves and mass flow controllers; thus, it is essential to purge the lines periodically and keep them clean. In the plasma, silane produces radicals that can react rapidly in the gas phase, forming particles. This results in nodules and large voids in the films. Several steps can help to solve such problems, namely: (1) reduced operating pressure (e.g. ECR plasma); (2) dilution of SiH_4 in Ar or He; (3) heating the electrode; and (4) use of a pulsed discharge [101].

The use of OS precursors to replace SiH_4 is motivated by its hazards (it is strongly pyrophoric), and by the fact that SiH_4 leads to low surface coverage as a result of its low surface mobility. Therefore, deposition of SiO_2 from hexamethyl disiloxane (HMDSO) and tetra ethoxysilane (TEOS) is widely used; such organic precursors are liquid and require the use of a bubbler (see theoretical study in [102]) or a liquid injection system.

9.5.2.2 Fluorinated Silicon Oxide

Work on fluorinated SiO_2 (SiO_2:F or SiOF) has been stimulated by the search for low-refractive index and low-permittivity (dielectric constant: low-ε or low-κ) materials for optics, photonics, and intermetallic dielectric layers, to reduce the parasitic capacitance in multilevel interconnects in microelectronic devices [103]. In such case, n could be reduced to 1.41–1.43 (at 550 nm), compared to 1.45–1.48 for non-fluorinated SiO_2 (Figure 9.12).

Fluorine was chosen for this purpose, owing to the low-ε properties of fluoropolymers and the properties of fluorine-doped amorphous silicon (*a*-Si:F), in which fluorine plays a stabilizing role, while passivating dangling bonds and reducing [H]. Many methods involving plasma have been applied to fabricate SiOF, using different organic and inorganic precursors, such as TEOS, SiH_4, CF_4, and C_2F_6 mixed with oxygen (for a review, see [7]).

The low-ε properties of SiOF are usually attributed to ionic bonding, such as the change in Si–O bond strength in the neighboring Si(O–)F sites, or replacement of –OH bonds in its structure. Reduction of n and k has also been observed in the visible frequency range, associated with a relaxation of θ, lower density, shorter Si/Si interatomic distance at low [F], and void formation, especially for high [F] [104].

The conclusions of studies of SiOF deposition may be summarized as follows. Optimized conditions should lead to θ of about 148° without the formation of $Si(O–)_2F_2$ and voids. The use of high O_2 (or N_2O) concentrations was found to lead to dense films and to the incorporation of more F. These effects are attributed to higher O_2^+ bombardment. SiOF represents an attractive low-n and low-κ material; dense, stable films with $n = 1.41$ and [F] = 12 at.% can be used in numerous applications, while porous, unstable films with $n = 1.38$ and [F] = 20 at.% need to be combined with a dense barrier layer (e.g. $SiN_{1.3}$ or TiO_2) in multilayer systems.

9.5.2.3 Silicon Nitride

Among possible nitride materials, $SiN_{1.3}$ has been widely used because of its transparency, hardness, impermeability, and other advantageous functional properties. It can be deposited using SiH_4 mixed with nitrogen (N_2) or ammonia (NH_3). The use of OS precursors is limited by the presence of carbon in the final product.

When deposited at low temperature and low energy conditions, $SiN_{1.3}$ exhibits a columnar structure; therefore, more energy must be brought to the surface by ion bombardment or

substrate heating in order to achieve high packing density. The residual gas concentration in the PECVD reactor must also be kept very low, as $SiN_{1.3}$ can react rapidly with traces of O_2 or H_2O [105].

The main 'impurity' in $SiN_{1.3}$ is hydrogen, which has a significant effect on the electronic and optical properties. Owing to the dense structure of the films and the valence of nitrogen versus oxygen, the amount of H (passivating broken bonds) is substantially higher in the nitride than in the oxide [18]; H mainly appears in Si–H and N–H bonds. Replacing Si–N by Si–H has little effect on the gap ($E_g = 5.3$ eV for H-free $SiN_{1.3}$) [106], but N–H bonds considerably reduce the value of n. For silicon-rich nitride, Si–H replaces Si–Si bonds, an approach to tailor the valence edge, and to increase E_g.

One way to avoid H incorporation is to use silicon halide precursors, such as $SiCl_4$ or SiF_4. The chemical affinity between Cl atoms and H atoms promotes the formation of HCl, which can further reduce the H concentration. In addition, the presence of halogen atoms gives rise to a competitive etching process during deposition, which can reduce the film roughness. For $SiN_{1.3}$ films grown in MW/RF plasma at $T_S = 25\,°C$, controlled ion bombardment gives rise to n values between 1.65 and 1.90 for V_B of 0 and 800 V, respectively [107]. The resulting hydrogen concentration is found to vary between 12 and 16 at.%, systematically less than in pure RF discharge [18]. It has been proposed that some of the hydrogen is not chemically bonded, but is trapped or chemisorbed on inner surfaces [18]. Attempts have been reported to deposit 'nitride-like' $SiN_{1.3}$ films from OS precursors, using for example hexamethyl disilazane (HMDSN) and hexamethyl cyclotrisilazane (HMCTSZN) [108], mixed with N_2 or NH_3.

9.5.2.4 Intermediate Oxide Materials

Several materials are particularly suitable for the fabrication of films with intermediate compositions, achieved by adjusting the gas mixtures [48, 107] or by controlling the film density [107, 109]. The most extensively used material for this purpose is SiON obtained from gas mixtures with SiH_4 using varying nitriding versus oxidizing gas ratio (e.g. NH_3/N_2O or N_2/O_2). Since O has more affinity to Si than N, one can choose to control only the O_2 flow.

According to detailed SE and electron spin resonance measurements, SiON films exhibit homogeneous and amorphous microstructures, close to those of a solid solution [110], and no crystal formation has been observed up to a temperature of 900 °C. These measurements lead to certain limitations in the use of EMA to model structural characteristics of such films; the main concerns are as follows: (1) H incorporated in the films reduces n. This is difficult to account for in the EMA model [110]; (2) films deposited at high E_i or T_S values represent solid solutions at the atomic level, containing O–Si–N bonds, hence no SiO_2 and $SiN_{1.3}$ domains can be distinguished; and (3) the optical and electrical characteristics may be dominated by the presence of pores (possibly filled with water vapor).

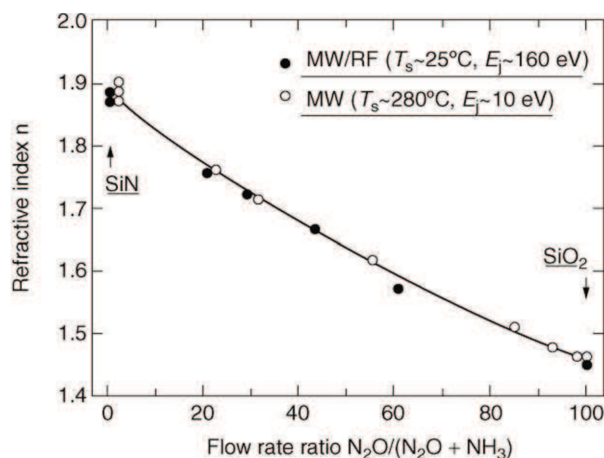

Figure 9.13: Refractive index of SiO_xN_y films as a function of the $N_2O/(N_2O + NH_3)$ concentration ratio in the gas mixture with SiH_4 in the MW and the dual-mode MW/RF plasmas. (After [111].)

The use of SiON films allows one to benefit from the advantages of the specific characteristics of individual SiO_2 and $SiN_{1.3}$ layers. In addition, as also discussed above, one can sensitively control evolution of the film microstructure by an appropriate choice of the ion bombardment conditions. Such choices are illustrated by the following examples.

By adjusting the NH_3/N_2O ratio in the mixture with SiH_4 in a dual-mode MW/RF discharge, one can vary n from high (corresponding to 1.9 for $SiN_{1.3}$) to low (corresponding to 1.45 for SiO_2) (Figure 9.13). This illustrates the possibility of obtaining films with any intermediate value of n, a useful property for the fabrication of discrete multilayer or graded (inhomogeneous) optical filters (discussed in detail in Section 9.6.1) or for other applications. In addition, one can distinguish, in Figure 9.13, two sets of data points, those pertaining to films prepared in pure MW plasma at $E_i = 10\,\text{eV}$ and $T_S = 250\,°\text{C}$, while essentially the same n values were obtained in a MW/RF plasma at $E_i = 160\,\text{eV}$ and $T_S = 25\,°\text{C}$ [107, 111]. A V_B was applied in excess of the $E_{i,c}$ necessary for ion-induced densification in agreement with the SZM.

The effect of V_B on the evolution of stress, σ, is illustrated in Figure 9.14 for films prepared in a MW/RF discharge from mixtures with SiH_4 at RT. The films develop a tensile stress at low ion bombarding energies (in pure MW discharge or at low V_B); when V_B is increased, the σ values pass through the zero-stress region, followed by a higher compressive stress, attributed to film densification and gas entrapment [112].

Silicon compound films have been shown to provide attractive electret properties. They can retain electric charge for extensive periods, suitable for such applications as electret microphones and electret-enhanced solar cells [112]. In such a case, when the film is exposed

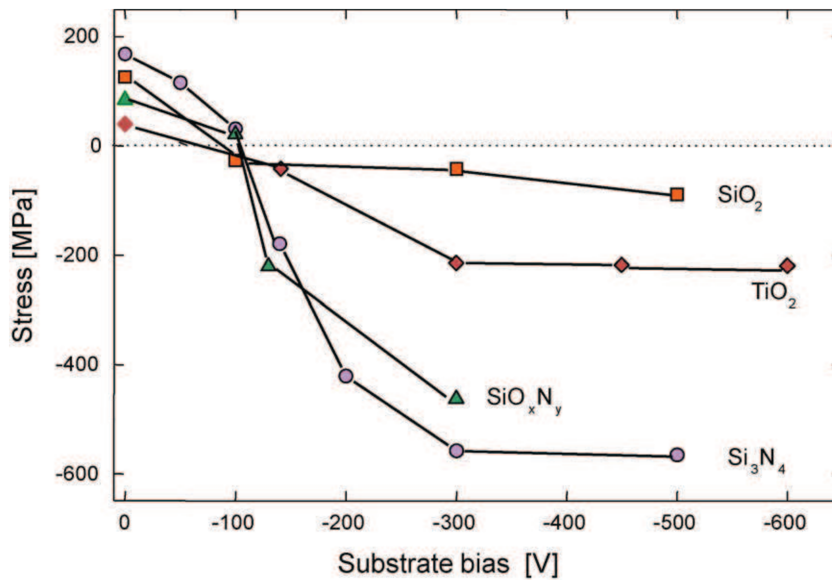

Figure 9.14: Evolution of stress in PECVD films as a function of substrate bias in the dual-mode MW/RF discharge. (Modified after [112].)

to corona-excited air, electric charges (electrons) are incorporated in traps in a range of energetic depth. Deep traps then release the electric charges when sufficient activation energy is supplied. Measured thermally stimulated currents from such electret structures (Figure 9.15) point to the fact that dense SiON films impregnated with OS vapors possess the deepest traps, thus providing very attractive electret properties.

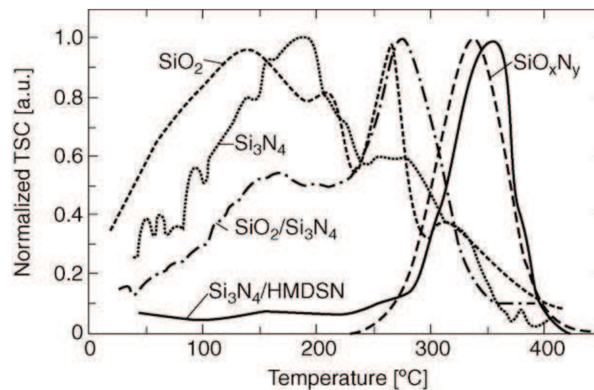

Figure 9.15: Thermally stimulated discharge currents in SiON electret films fabricated and treated under different conditions. (After [112].)

Other Si-based graded materials have also been studied. These include GeO_2/SiO_2 films obtained from a $TEOS/O_2$ mixture doped with TMGe [113], Si-rich SiN_x (absorbing) films considered for near-infrared (NIR) applications, and F-doped SiO_2 which have been studied for graded n optical filters [114].

9.5.2.5 Silicon Carbide and Silicon Carbon Nitride Coatings

Amorphous hydrogenated silicon carbide (*a*-SiC:H or SiC) coatings are attractive because of their optical, electronic, and mechanical properties [2, 115, 116]. Using PECVD, SiC is usually obtained from varying mixtures of SiH_4 and CH_4 or OS at relatively low substrates temperatures ($T_S = 200$–$400\,^\circ C$) [115, 117]. Microstructural characteristics, composition, and mechanical properties of SiC can be controlled by an appropriate selection of process parameters.

Ternary Si compound coatings, such as SiCN, have become increasingly attractive since they can combine advantages of the individual binary materials and of their intrinsic properties, specifically of $SiN_{1.3}$, SiC, and CN. In this context, the important characteristics are: (1) high optical transparency and wide E_g (~ 5 eV) of $SiN_{1.3}$; (2) lower E_g (~ 2.8 eV) and interesting mechanical performance of SiC; and (3) high hardness, partial electrical conductivity, and high elastic rebound due to a fullerene-like microstructure of CN. These three materials are miscible; therefore, by changing the phase content and by controlling the short range order, it is possible to tune the properties of SiCN films for specific electronic, tribomechanical, and other applications. Many interesting results have been reported on such ternary SiCN films, including analysis of its complex chemical structure using infrared SE, and of its tribological properties [118].

9.5.3 Carbon-Based and Related Coatings

The study of various carbon-based materials has been stimulated by a combination of their very advantageous functional properties, ranging from high hardness and low friction to optical transparency in IR, high corrosion resistance, high heat conductivity and biocompatibility. They can be categorized, depending on the sp^2 and sp^3 hybridization, level of structural order, as well as by hydrogen concentration (Figure 9.16). The subject of carbonaceous coatings has been covered in other reviews [119, 120]. Here, we briefly introduce different categories of carbon, specify the nomenclature, and give several examples where the performance of different carbonaceous systems has been controlled by the growth parameters, in particular E_i and T_S.

We distinguish among the most frequent forms of carbon-based films, namely (1) PECVD diamond-like carbon (DLC) or amorphous hydrogenated carbon (*a*-C:H); (2) polycrystalline diamond (pc-D) or nanocrystalline diamond (NCD); and (3) soft organic carbonaceous coatings (plasma polymers) obtained under ‘mild’ plasma conditions. In this context, several

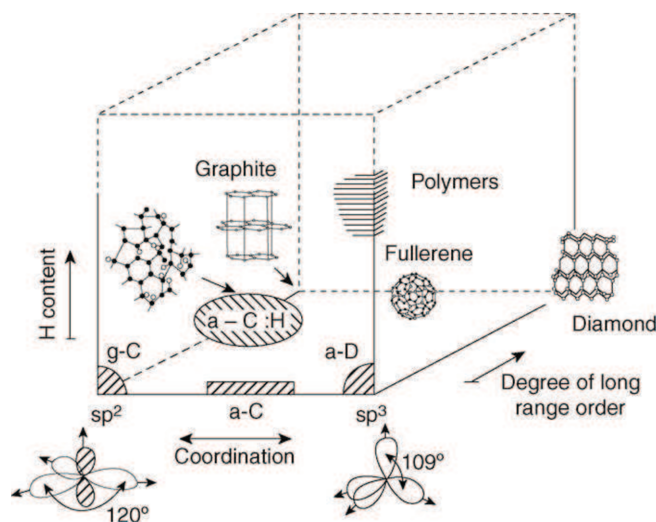

Figure 9.16: Schematic representation of different phases of carbon distinguished by the carbon coordination, degree of range order, and hydrogen content. (After [87].)

categories of organic amorphous PECVD films prepared from hydrocarbon precursors under controlled ion bombardment can be distinguished based on E_i: [7] (a) plasma polymers, $E_i < 30$ eV ([H] = 35 at.%, and $n = 1.6$); (b) soft ('polymer-like') DLC, $E_i = 30$–60 eV ([H] = 30 at.%, and $n = 1.6$–1.8); and hard DLC, 60 eV $< E_i <$ 1 keV ([H] = 20 at.%, $n = 1.8$–2.2, and $E_g = 1.3$–2.0 eV).

Diamond-like carbon films obtained by PECVD from hydrocarbon gases or vapors have been studied for their possible use in functional coatings. They are particularly attractive in combination with their advantageous mechanical and tribological characteristics, such as high hardness ($H = 15$–40 GPa, see Figure 9.12), low friction coefficient ($\mu = 0.05$–0.15), high scratch resistance and biocompatibility. These properties strongly depend on the microstructure (sp^2/sp^3 hybridization ratio) and the hydrogen content [H] (for reviews, see e.g. [120–122]).

The presence of hydrogen contributes to the formation of C–H σ bonds at the expense of π bonds (sp^2 hybridization). The latter affect the density of states and E_g values [120]. Using ERD and IR analyses of DLC films deposited under controlled E_i and Φ_i values in RF and MW/RF discharges, it has been concluded that a significant amount of hydrogen is not chemically bonded, but is trapped inside the material [123]. In addition to its effect on H and thermal stability, the amount of unbonded hydrogen has also been related to density and stress. As illustrated in Figure 9.17, σ in DLC films obtained from CH_4/Ar mixtures is systematically higher for the RF mode of operation (high E_i, low Φ_i, low n_e and hence less gas-phase dissociation), compared to the MW/RF mode (low E_i, high Φ_i, high n_e). Recently, these experimental observations have been supported by molecular dynamics simulations which

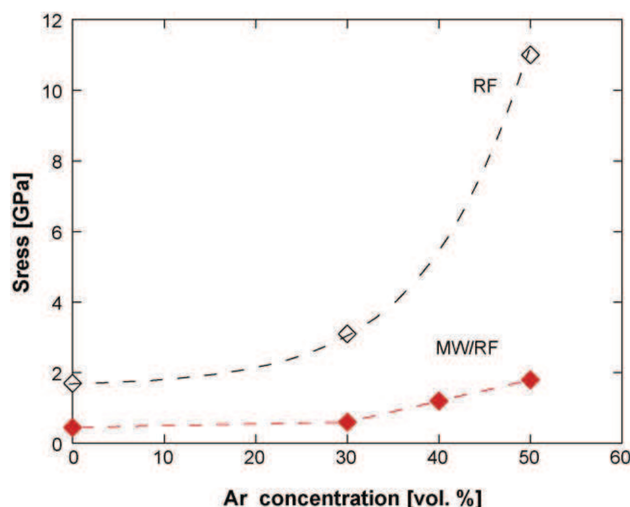

Figure 9.17: Effect of argon concentration in CH_4 on the evolution of compressive stress in hard DLC (*a*-C:H films) obtained in RF ($V_B = -500$ V) and in MW/RF ($V_B = -200$ V) plasmas. (After [123].)

predict that up to several tens of % of molecular hydrogen can be trapped in the internal volume of a DLC film [124].

The microstructure can also be influenced by doping *a*-C layers with nitrogen [125]. This can lead to higher optical absorption, higher electrical conductivity (N acting as a dopant near the edge of the density-of-states in the sp^3 matrix), and a higher Young's modulus (N acting to promote three-dimensional (3D) curvature and attachment in the sp^2 clusters). The addition of fluorine has been studied in an attempt to obtain higher transparency [126]. Incorporation of Si reduces stress and increases thermal and corrosion stability [127].

Polycrystalline diamond films have high refractive index ($n = 2.35$) and transparency over a large wavelength range (0.2–20 μm), and have attracted much attention owing to their extreme hardness ($H = 90$–100 GPa, see Figure 9.12), heat conductivity, and chemical inertness. Their unique properties have stimulated considerable interest for numerous applications, ranging from infrared optics to electronics, biomedical engineering, manufacturing, and numerous other sectors (for reviews, see [119, 128, 129]).

Diamond films are typically prepared from highly diluted mixtures of hydrocarbons (such as CH_4) in hydrogen (< 1% CH_4) in dense MW plasma, complementary to the thermal CVD technique. In plasma, atomic hydrogen acts as an etchant for the sp^2 (graphitic) phase, leaving behind the desired sp^3 (diamond) phase, resulting in polycrystalline structure formed at high T_S, in excess of 600 °C. In certain applications (e.g. optics), the use of diamond may be limited by the presence of relatively large crystals (∼ 1 μm in size) leading to light scattering. However, very smooth, NCD films [130] or laser-polished films [129] have been reported.

Cubic boron nitride (c-BN) is the second hardest (70 GPa) material, and it possesses the second highest thermal conductivity (13 W cm^{-1} K^{-1}) compared to diamond (100 GPa, 20 W cm^{-1} K^{-1}). In fact, c-BN is superior to diamond in several respects: this includes high oxidation (1200 °C) and graphitization (1500 °C) temperatures (compared to 600 and 1400 °C for diamond), and it is a very promising wide bandgap semiconductor since it can be both n- and p-type doped. This material has attracted considerable interest stimulated by the development of coated cutting tools, and of thermal, optical, high-temperature, and high-frequency electronic devices (for review, see [131]).

Owing to the lack of an effective chemical reactant similar to hydrogen in CVD deposition of diamond films (selective etching of non-diamond phases and stabilization of the sp^3 hybridization [120, 230, 131]), it is necessary to apply a high negative bias voltage during c-BN growth in the PECVD reactor. c-BN film deposition using a mixture of different gases such as B_2H_6, BH_3NH_3, BF_3 and trimethyl borazol mixed with H_2, N_2, or NH_3 has been performed using DC jet, RF, ICP or ECR reactors [131]. Recently, films possessing very high hardness (70 GPa) have been obtained [132]. This value has even been significantly increased (H = 82 GPa) when fabricating c-BN/NCD mulilayer systems [133].

Research on o*rganic PECVD films (plasma polymers)*, especially on plasma polymerized fluorocarbons (PPFC), has been stimulated by the prospect of obtaining low n and low ε values similar to those of bulk polytetrafluoroethylene (PTFE, e.g. Dupont Teflon, with $n = 1.35$) or, more recently, for amorphous fluorocarbons, such as Dupont Teflon AF2400 ($n = 1.29$) or Teflon AF1600 ($n = 1.31$) [4, 134–136]. There is an abundant literature on the use of fluorocarbon plasmas for film deposition, and for anisotropic etching of silicon and silicon dioxide [12, 137]. By suitably adjusting the experimental parameters, one can shift the plasma conditions from etching to deposition modes [138]. Various precursors have been explored for deposition. These include C_2F_4, C_2F_6, C_4F_8, C_3F_6, $C_2H_2F_4$, CH_2F_4 and others [4, 134, 139]. The frequently observed low n is generally attributed to a high concentration of CF_2 groups in the films. Plasma-deposited layers usually contain a significant concentration of dangling bonds (estimated at 10^{18}–10^{20} spin/cm^3) [140], which can react with atmospheric oxygen or water vapor leading to the formation of C=O groups [140, 141] and to aging effects [142]. The use of pulsed PECVD has been shown to produce PPFC with lower concentrations of dangling bonds [139]. In general, PPFC films are very hydrophobic and not easily compatible with other layers in multilayer systems, owing to adhesion problems. They are, however, good candidates for water-repellent and smudge-resistant top coats [143].

Other plasma polymer materials include plasma polymerized organosilicones (PPOS), plasma polymerized hydrocarbons (PPHC), and hybrid (mixed organic–inorganic) coatings. In addition to their interesting tribological and optical properties, they are frequently considered for biomedical applications, because of their excellent biocompatibility. The reader is referred to numerous exhaustive reviews on the subject [4, 134].

9.5.4 Metal-Based Compound and Nanocomposite Films

Fabrication of metal oxide, nitride, and carbide films has been inspired by the prospect of obtaining high n, high hardness, advantageous tribological properties, and numerous other functional characteristics. The films are generally prepared from halocarbons or from metal-organic compounds which exhibit specific requirements on handling low vapor pressure sources and/or corrosive products [76]. In this section, we first focus on metal oxide layers, particularly on their optical and mechanical characteristics. In the second part, we describe metal nitrides and carbides, and review the microstructural features and the unique properties of superhard nanocomposite films.

9.5.4.1 Metal Oxides and Optically Passive and Active Films

Titanium dioxide (TiO_2) attracts much attention because of its large bandgap, high n (exceeding 2.4 at 550 nm), and photocatalytic properties. Its high n is due to high ionic character of the TiO_6 octahedral structure, the building block of rutile and of anatase.

The deposition of oxides of transition metals such as Ti (including Ta, Nb and others) is complicated by the fact that they can take different forms and stoichiometries (e.g. TiO or Ti_2O_3) [144]. In addition, in the case of TiO_2, three stable crystalline phases are possible: rutile, anatase, and brookite. Rutile, with the highest density, is the most desired phase in terms of transparency and index, but also has the highest birefringence, with $n_{ord} = 2.9$ and $n_{ext} = 2.6$, and is often unwelcome because of light scattering. Anatase, which differs from rutile in the coordination number of its TiO_6 octahedra (10 in the case of rutile, 8 for anatase), is less birefringent, and has $n = 2.5$. Brookite, an unstable rhombohedral structure, is rarely observed in thin films.

The most frequently used precursors for plasma deposition of Ti-compounds are $TiCl_4$, tetraisopropyltitanate (TIPT), tetra ethoxy titanium (TEOT), $Ti(O–i–C_3H_7)_4$, and $Ti[OCH(CH_3)_2]_4$ (mixed with O_2 or N_2) (for review, see [7]). The use of metal-organic precursors has been stimulated by two considerations: (1) $TiCl_4$ is hazardous, highly corrosive, and requires special installations; and (2) Cl can be a major contaminant in TiO_2 and decreases long-term stability, increasing its absorption coefficient.

Both rutile and anatase are tetragonal and often coexist in films. High temperatures and ion bombardment energy may be needed during growth to control the rutile/anatase concentration ratio. At temperatures below 200 °C, anatase is frequently observed. Using a $TiCl_4/He/O_2$ mixture in an ECR/RF PECVD system [145], it was found that rutile is formed above 600 °C, and that it is the only phase observed above 900 °C. For higher E_i, lower r_D has been observed, resulting from RIE due to Cl, and competing with film densification. However, anatase is favored at high V_B values.

For most applications, crystallization of the films and the size of crystallites must be carefully controlled (e.g. to avoid light scattering). T_S is often kept below 200 °C to prevent crystal formation. The crystallization and phase change temperatures can vary with film thickness and impurities, and crystallization can also be suppressed by mixing TiO_2 with other materials such as SiO_2 [146]. RT-deposited films generally possess a low concentration of Cl (~ 6 at.%), which further decreases with increasing T_S and V_B, accompanied by an increase of n. The films often exhibit excess oxygen (O/Ti > 2), related to hydroxyl groups and to film density, an effect also found for sputtered TiO_2 layers.

Tantalum oxide and *niobium oxide* have been deposited by PECVD using a mixture of metal iso-propoxide (($Ta(OC_2H_5)_5$ or $Nb(OC_2H_5)_5$)) and O_2 with Ar and an RF plasma under intense ion bombardment. They exhibit good optical quality, suitable for various applications including interference filters and protective layers. Their n values were found to be between 2.12 and 2.16, and 2.26, for Ta_2O_5 and Nb_2O, respectively, and the H values between 8 and 10 GPa for both materials [147], comparable with those of the PVD coatings (see Figure 9.12).

Despite the use of O_2-rich deposition atmosphere, both Ta and Nb oxides exhibited about 6 at.% of carbon, uniformly distributed throughout the thickness. However, detailed optical measurements did not reveal any negative effect of the presence of C on the optical performance such as absorption. Both materials showed high temperature stability, with the onset of crystallization observed at 550 °C and 650 °C, respectively [148], making them very attractive high-index alternatives for optical, photonics, and other applications.

Studies of optically active PECVD materials have been stimulated by interesting linear and non-linear optical properties, and by their electrical and protective characteristics. These include:

- Transparent conductors such as *tin–oxide* (SnO_2) [149] and *indium–tin–oxide* [150], the latter obtained from indium nitrate pentahydrate and tin–chloride pentahydrate in water, using an ultrasonic nebulizer in combination with an RF ‘mist’ Ar/O_2 plasma.
- *Yttria-stabilized zirconia* (YSZ), *barium titanate* ($BaTiO_3$), and *strontium titanate* ($SrTiO_3$) were fabricated from metal β-diketonates [151]. The latter two were obtained by combining melted dipivaloylmethanato barium ($Ba(dpm)_2$) and strontium ($Sr(dpm)_2$) compounds with TIPT in an O_2 plasma. The n values of $BaTiO_3$ and $SrTiO_3$ were both found to be 2.19. The permittivity was estimated from capacitance–voltage curves to be 1×10^3 for $BaTiO_3$, and 1×10^2 for $SrTiO_3$, primarily due to a high ionic polarizability.
- *Aluminum oxide* (Al_2O_3) is most often prepared from $AlBr_3$, $AlCl_3$, trimethyl-aluminum (TMA), or trimethyl-amine alane (TMAA) precursors mixed with O_2 or N_2O [7, 76, 152, 153]. *Er^{3+}-doped Al_2O_3*, using

tris(2,2,6,6-tetramethyl-3,5-heptanedionato)erbium ($Er(thd)_3$) as the erbium precursor, has also been fabricated by PECVD [154].

- *Tungsten oxide* (WO_3) films obtained in RF plasma from WF_6 mixed with H_2 and O_2 [155, 156] were studied for their potential use in electrochromic devices including smart windows and sensors [157]. Growth rates (up to 10 nm/s) were maximized when the atomic F density was suppressed and the atomic O density enhanced. Optimal film density was obtained for medium E_i values $\sim$(50–100 eV). The value of n was shown to be a sensitive indicator of the electrochromic performance. The absorption coefficients were similar for both Li^+ and H^+ ions, scaling with the degree of intercalation in the opaque state [158].
- Work on *nanocomposite (nc) optical materials*, formed by nanometer size (1–100 nm, mostly metal) particles embedded in dielectric matrices, has been stimulated by new film properties, such as optical selectivity (absorption filters; colored, decorative coatings; photothermal energy conversion) and optical non-linearity, phenomena linked with the surface plasmon resonance [159]. Depending on the choice of materials and particle concentration, size, and shape, different colors can be obtained. The presence of nanoparticles leads to a substantial local field enhancement [160], giving rise to third order susceptibility, $\chi^{(3)}$, up to 10^{-6} esu [161, 162].
  The nc structures are usually fabricated by hybrid processes, combining PECVD of organic (PPFC, PPHC) or inorganic (SiO_2, Al_2O_3, $SiN_{1.3}$, TiO_2) matrices with simultaneous sputtering or evaporation of metals, such as Au, Ag, Cu, and others (for more details, see [37–39]).

The effect of microstructure on the properties of such nc materials has been modeled using EMA to interpret experimental data obtained by SE and spectrophotometry. Using the generalized Maxwell–Garnett model, considering the permittivities of the host and particle materials, the depolarization factor and the interband and intraband electron transitions, particle concentration, size, and shape can be obtained from non-invasive optical measurements [38]. This particularly also applies to the study of Au/SiO_2 nc films exposed to heavy ion bombardment (tens of MeV) [39]. Energetic ion ‘hammering’ introduces locally significant internal stress, converting initially spherical particles into nanorods with high aspect ratio. Polarization-dependent non-linear optical absorption has recently been detected and modeled using a modified EMA approach [163].

9.5.4.2 Metal Nitrides, Carbides, and Nanocomposite Superhard Coatings

Metal nitrides and carbides (MeN, MeC) are widely used as protective coatings, owing to excellent mechanical properties [164–166] such as high hardness, adhesion, and corrosion resistance, which makes them attractive for tribological applications. In addition, such materials provide interesting colors [167] related to the bonding structure [168].

MeN and MeC are obtained by PECVD, when organometallic or chelate precursors are decomposed in mixtures containing N_2 or CH_4, Ar and H_2. The film microstructure can be selectively controlled by adjusting chemical reactions in the gas phase and at the growing surface, and by appropriate choice of E_i, Φ_i and Φ_n values, which affect the development of crystals, their size, shape, and orientation [164–166, 169–172]. One of the frequent concerns in this activity is handling hazardous and corrosive precursors, including metal chlorides.

Nanocomposite superhard coatings formed by nanometer size particles (usually MeN, MeC) embedded in amorphous or crystalline matrices are of considerable interest. These 3D architectures, also called 'third generation ceramic coatings', represent a new class of materials that exhibit exceptional mechanical, electronic, magnetic, and optical properties due to microstructural features which are reduced to approximately 5–10 nm [164–166, 168–173].

Such hard nc-MeN/hard matrix (usually amorphous such as $SiN_{1.3}$) materials have been fabricated by PECVD [164, 167, 169, 171, 172], complementary to the nc-MeN/soft matrix (usually metal, Me = Ti, Cr, W, V, Zr) films prepared by PVD [166]. Formation of nc structures is based on the thermodynamically driven segregation in binary, ternary, or quaternary systems, which leads to spontaneous self-organization of a stable nanoscale structure [164]. The microstructure of nc gives rise to high H with relatively low E providing high toughness, enhanced wear resistance, high elastic recovery, resistance against crack formation and crack propagation, high thermal stability (up to 1100 °C), and reduced thermal conductivity. These properties are explained by the difficulty of creating dislocations in grains of tens of nanometers in size, and by the reduction of intergranular sliding due to the thinness of the grain boundary region. In general, such properties are controlled by crystal size, orientation, and shape, and by grain boundary thickness, and they depend on the selection of materials, process parameters such as E_i and Φ_i, and deposition methods [166, 169–172].

Of all nc superhard ($H > 40$ GPa) films, TiN-based coatings with $SiN_{1.3}$ matrix have been the most frequently investigated. As an example, the effect of silicon concentration [Si] on H and E for nc-TiN/$SiN_{1.3}$ films, fabricated at $T_s = 500$ °C is shown in Figure 9.18(a). Both clearly exhibit a maximum at an optimum [Si] situated between 5 and 10 at.% that corresponds to an amount of $SiN_{1.3}$ that forms a matrix which surrounds the TiN particles (5–10 nm in diameter). It has been proposed that the boundary between grains is about one monolayer thick [164, 169, 170, 173, 174].

In order to obtain insight into the microstructural characteristics on the nanoscale, and to determine complementary functional properties, electrical resistivity, ρ_E, of such nc films has been studied by in situ RTSE and ex situ four-point measurements [70, 167]. As an example, the effect of [Si] on ρ_E is presented in Figure 9.18(b). The metallic character of pure TiN and of the nc-TiN/$SiN_{1.3}$ was confirmed by low values of ρ_E until about [Si] ~ 40 at.%, above which the loss of metallic character was marked by the onset of a rapid increase in ρ_E due to

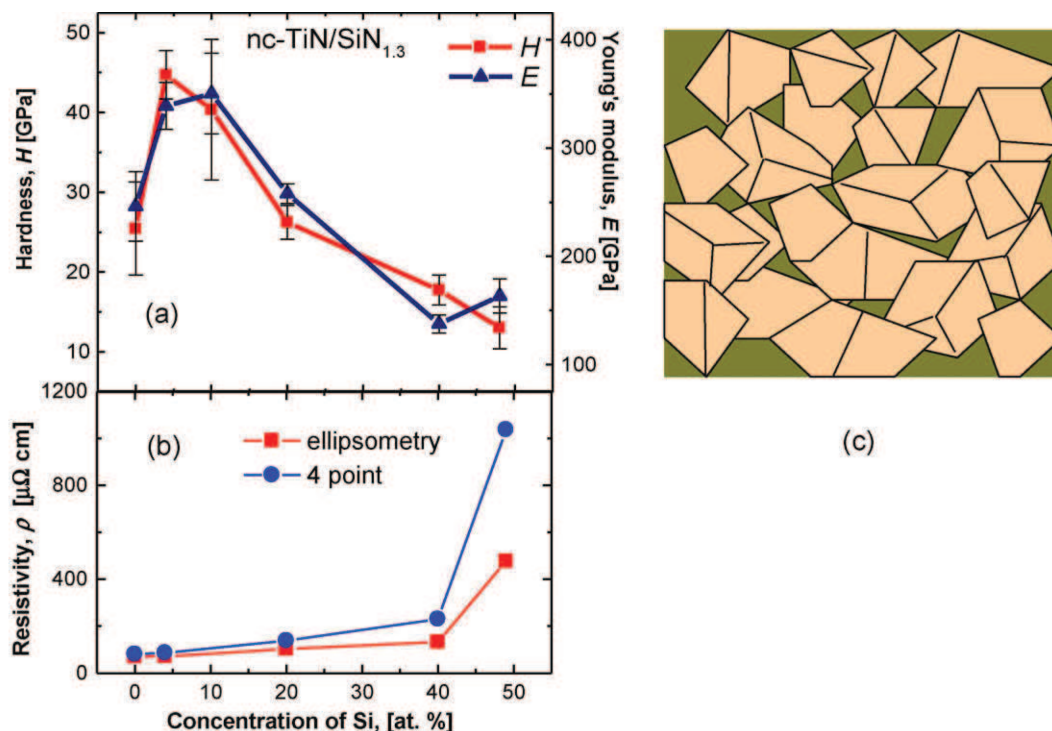

Figure 9.18: Characteristics of nanocomposite nc-TiN/$SiN_{1.3}$ films: (a) effect of Si concentration on the microhardness, *H*, and Young's modulus, *E* [171]; (b) effect of Si concentration on the resistivity measured by spectroscopic ellipsometry and by the four-point method [167]; (c) microstructural model of a superhard nanocomposite coating corresponding to the highest hardness [70].

percolation. Since ρ_E remains low at [Si] corresponding to the highest H value, the TiN particles appear to still be interconnected, as illustrated in the structural model schematically shown in Figure 9.18(c).

This model incorporates the main structural characteristics of the nc films, namely the presence of nanoparticles, the introduction of interface layers, and the possible presence of defects, indicated by charge carrier mean free path much smaller than the particle size [70]. The model suggests that the amorphous matrix fills the space between individual nanoparticles rather than forming a uniform layer around them. Consistent with the electrical properties [70, 167], it can explain the mechanical characteristics of nc films by the presence of inner interfaces, which hamper crack propagation.

Recently, molecular dynamics (MD) calculations have been used to support the experimental data regarding Ti(Si)N materials by fitting two-body empirical potentials using energies from

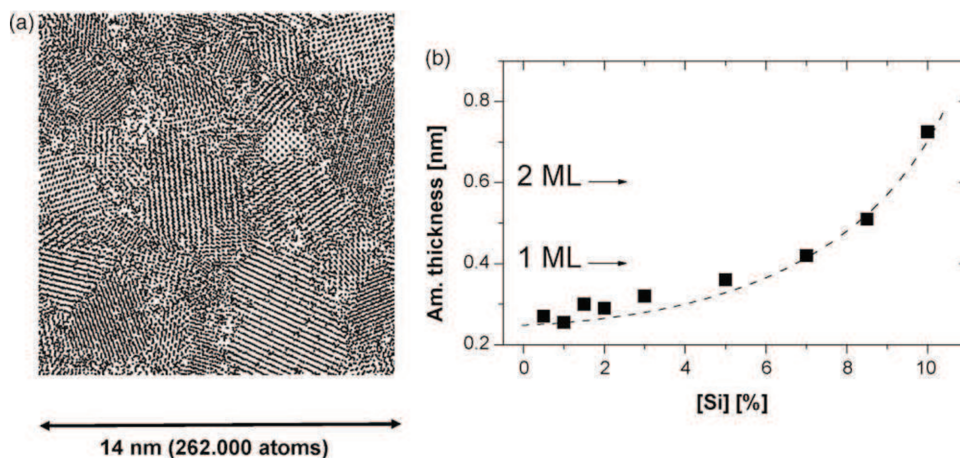

Figure 9.19: Molecular dynamics simulations of the characteristics of nanocomposite nc-TiN/$SiN_{1.3}$ films: (a) slice of the final structure corresponding to [Si] = 7 at.%; (b) thickness of the amorphous $SiN_{1.3}$ phase between the TiN particles. (After [174].)

ab initio calculations [174]. Thermodynamically preferred structures of various compositions were found by slow cooling from a melt: for TiN, it was confirmed that the preferred structure is a cubic (fcc) monocrystal, while for TiSiN, the heterogeneous structure consists of small (< 10 nm) crystals of TiN in a Si-rich amorphous matrix. In addition, the MD simulations predict other structural characteristics of this nc material: (1) a solubility limit of Si in TiN (close to 2%), above which the material becomes heterogeneous; (2) a distribution of sizes of TiN nanocrystals for various compositions (e.g. up to 6000 atoms corresponding to ≈5–9 nm particle size for [Si] = 7%) as illustrated in Figure 9.19(a); (3) the quality of the nanocrystals in terms of defects or angles between the crystalline planes; (4) the thickness of the amorphous phase between the nanocrystals – about 1–2 monolayers at [Si] = 7% (Figure 9.19b); and (5) a probability that the individual nanoparticles touch each other.

9.5.5 Interface Engineering

Interfaces in coating technology are of particular importance for several reasons: (1) to ensure compatibility and adhesion between the coating and the substrate and between the individual coatings; (2) to ensure the thickness (or abruptness) of the interfacial region, or to consider possible compositional and structural gradients inherent to the fabrication process; and (3) to control the characteristics of the interfacial region, ‘interphase’, in order to enhance the performance of the thin film system. In the following, we provide examples of several coating/substrate combinations for which the understanding of the role of plasma surface interactions is crucial.

9.5.5.1 Coatings on Inorganic Substrates

The role of ion bombardment and the possibility of predicting its effect in multilayer systems and related film architectures have recently been studied by RTSE combined with dynamic TRIDYN Monte Carlo simulations [68, 69] (see Section 9.4). It has been shown that ion- and plasma-assisted deposition processes in the range of tens to a few hundreds of electron volts lead to thin film growth dominated by subsurface deposition, as a result of subplantation (shallow implantation). Subplantation is shown to be responsible for significant subsurface modifications and interface broadening during the initial stages of film deposition, as a result of ion mixing.

Control of the thickness of the interfacial layer is very important for ensuring appropriate performance of interference filters and electronic devices, as well as tribological coatings; in specific cases the interphase can be comparable with the film thickness and it must be included in the coating system design.

For the particular case of TiO_2 grown on SiO_2 by PECVD (e.g. in the context of optical interference filters, using high and low values of n) in an O_2-rich plasma, at the RF-biased electrode, the experimentally determined IEDF has been modeled as shown in Figure 9.9. Given by the range of E_i, the formation of 2–4 nm-thick interfacial layers was predicted. The value predicted depended on the Φ_i/Φ_n ratio, which was controlled by varying r_D (Figure 9.20). Such behavior has been found in excellent agreement with RTSE, and has been directly confirmed by HRTEM for PECVD, and for PVD layers [68, 69].

Controlled modification of the interphase has been the subject of extensive work in the field of hard protective coatings on metal substrates and it is known as a duplex process [175]. Here, the metal piece to be coated (e.g. steel) is first exposed to a nitriding or carburizing plasma in order to sputter-clean the surface, and to harden the near-surface region by implementing a hardness gradient up to several μm in thickness due to the diffusion of nitrogen or carbon [176, 177]. In addition, specific interface engineering steps may include formation of a diffusion barrier at the interface, for example, to hamper diffusion of cobalt from a WC-Co substrate, when pc-D is deposited at elevated temperatures [178]. This would otherwise lead to the formation of a weak CoC interlayer. In contrast, routine plasma surface nitriding of steel can also have a negative effect on the corrosion resistance: when stainless steel is exposed to N_2-rich plasma, N preferentially reacts with chromium, leaving behind iron which becomes more prone to subsequent corrosion [179].

9.5.5.2 Coatings on Plastics

The role and control of interfaces between plastic substrates and inorganic coatings is of particular importance for the performance of the final devices. Energetic interactions of plasma with the exposed polymer surface lead to substantial modification of the physical and chemical

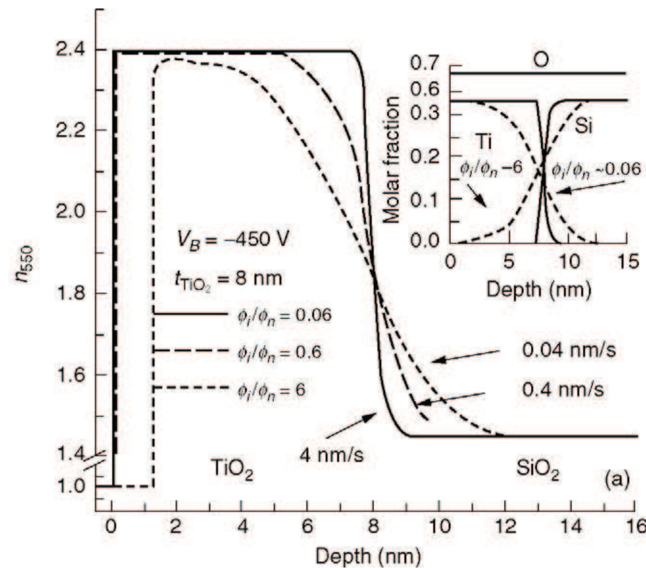

Figure 9.20: Ion bombardment effects in PECVD on the TiO_2/SiO_2 interface considering an IEDF according to Figure 9.9. The curves correspond to different ion/neutral flux ratios and their effect on the width of the TiO_2/SiO_2 interface represented by the "abruptness" of the refractive index at 550 nm. (After [68].)

properties of the surface and the near-surface region, and they affect the initial stage of the film growth.

Surface modification of polymers is particularly important to improve adhesion. In comparison with other methods of modifying polymer surfaces [14], including wet-chemical or mechanical treatments, exposure to flames, UV radiation, corona discharges, ion beams, and intermediate adhesive layers, low-pressure plasma modification appears very powerful, since it can address all of the adhesion mechanisms [11, 13, 180]. In this context, there are four major effects of plasma on polymer surfaces: (1) surface cleaning; (2) ablation (or etching); (3) cross-linking, and (4) surface chemical functionalization. All of them are always present to a certain degree, but one may dominate, depending on the polymer, gas, and operating conditions.

Adhesion enhancement by plasma pretreatment is illustrated in Figure 9.21(a), where PECVD $SiN_{1.3}$ was applied as a first layer in multilayer antireflective (AR) coatings or as a gas permeation barrier on polycarbonate (PC) and polyethylene terephthalate (PET) [143, 181, 182]. After pretreatment of PC in MW plasma, the highest adhesion was found when using N_2 (highest critical load, L_C, in the scratch test). Based on complementary surface analyses, adhesion improvement has been related to the formation of new N- and O-containing groups, which react with Si to form Si–N–C and Si–O–C bonds at the interface [181]. In addition,

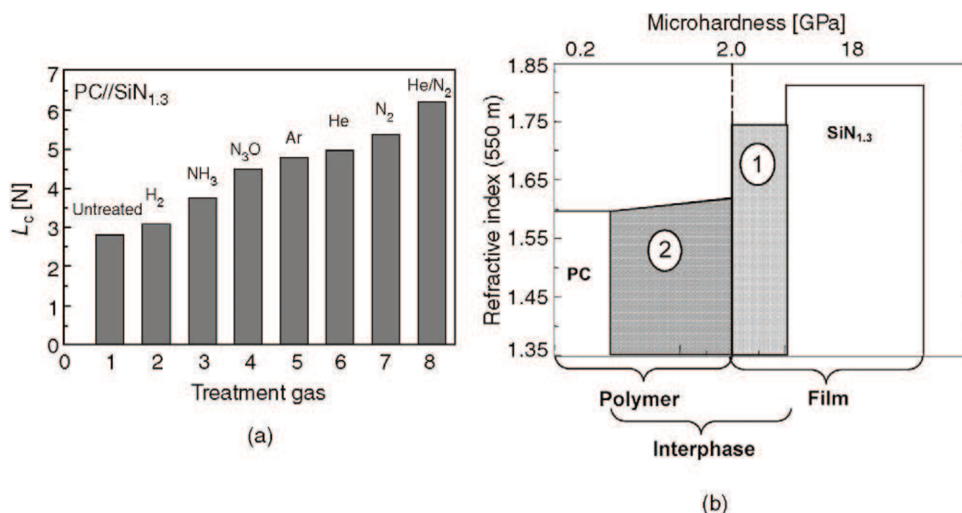

Figure 9.21: Effect of plasma treatment of polymer surface (example of polycarbonate) on the characteristics of the polymer/coating interface: (a) effect of different gases on the adhesion of $SiN_{1.3}$ films (critical load, L_c, film thickness 0.5 μm); (b) structured interfacial region (interphase) represented by the refractive index depth profile. (After [143].)

adhesion was further improved by exposing PC to He plasma, confirming a favorable effect of the VUV radiation.

Owing to the phenomena involving energetic photons, ions, and reactive species (see Section 9.4), the interphase is structured (Figure 9.21b). Similar depth profiles have been observed for other combinations of materials, including SiO_2, PET, polymethyl methacrylate (PMMA), and other polymers [183]. Using both non-invasive optical (in situ and ex situ SE, photometry, IR spectroscopy) and invasive methods, the interphase has been found to be several tens of nanometers thick [181–185]. It consists of a cross-linked layer (region 2 in Figure 9.21b), followed by a transition layer (region 1) formed by intermixing the growing film with the substrate materials [185] and possibly by voids [186]. In the case of $SiN_{1.3}$ considered in the context of optical or barrier applications, n increases from 1.59 for PC to 1.80, while H increases by two orders of magnitude from 0.2 GPa for bulk PC to ~2 GPa for the cross-linked surface layer, and up to 18 GPa for $SiN_{1.3}$ [143, 187]. This inhomogeneity generally leads to better adhesion, tribological properties, flexibility, stretchability, and other functional characteristics suitable for coated plastics.

Formation of the interphase has also been observed for situations when no specific plasma pretreatment has been performed. Indeed, the energetic conditions are still present when the film starts growing (nucleation), while the plasma is always a rich source of energetic photons, particularly owing to the presence of hydrogen originating from the precursor, from the

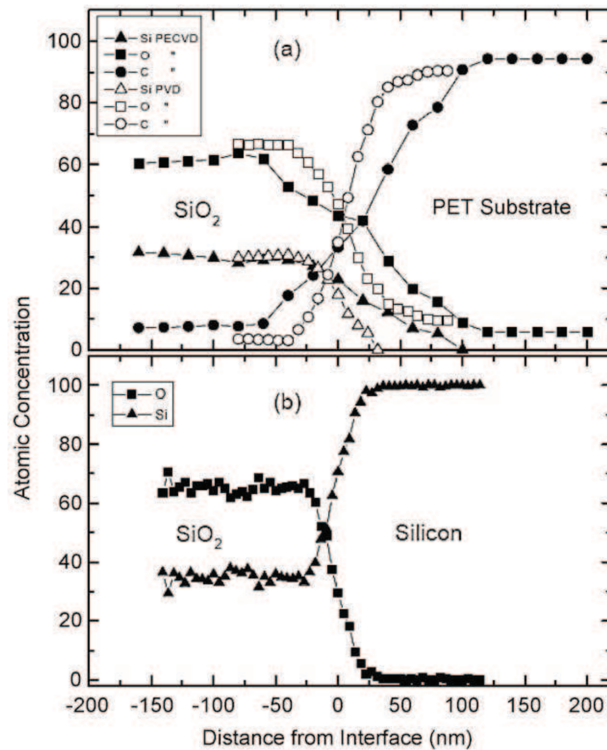

Figure 9.22: Comparison of compositional depth profiles of the SiO_2/substrate interfacial region obtained by ERD: (a) PECVD (320 nm, full symbols) and PVD (120 nm, open symbols) SiO_2 layers on PET; (b) thermal CVD (200 nm) SiO_2 on c-Si. (After [185].)

polymer material itself, or from residual water vapor. This situation is quite different from PVD processes in which hydrogen concentrations in the gas phase and energetic VUV radiation are less intense. In fact, no interphase (below detection) has been observed for inorganic films, such as SiO_2 on PET, fabricated by PVD compared to the PECVD layer [185] (Figure 9.22). This may explain the generally observed better mechanical performance of PECVD coatings on plastics, compared to their PVD counterparts.

9.6 Functional Characteristics and Applications of PECVD Coatings

In the previous sections, we have introduced basic phenomena governing the plasma processing of materials, the evolution of their microstructure and a number of concepts of structure–property relationships. Given the recent progress in this field, numerous attractive applications of PECVD have been proposed and investigated, based on the functional characteristics of the coating, which are related to basic properties. Examples are given in

Figure 9.12 and Table 9.1. Many of the applications have already left the laboratory and pilot scales and entered large-scale production.

Given the large number of applications, both under investigation and exploited commercially, we do not attempt to list them all. Rather, we focus on selected examples of specific functional properties of films illustrating advances in this field, while demonstrating the importance of plasma–surface interactions in their preparation. In particular, we describe two broad areas: optical and related coatings (Section 9.6.1), and protective tribological coatings (Section 9.6.2). The reader is referred to numerous publications covering other areas in which plasma processing has advanced significantly. These include electronics [1, 188], biomedical engineering [189, 190], and surface treatment of plastics [4, 11, 14].

9.6.1 Optical and Related Functional Coating Systems

The microstructure and composition of optical films depend on the choice of source precursor and of other gases, and on surface reactions during film fabrication, including the energetic conditions in film growth. These govern their optical, mechanical, and other functional characteristics which need to be taken into account when the films are applied to the fabrication of optical coating systems. In most cases, optical thin films are amorphous, since they are deposited at low substrate temperatures, typically below 250 °C. However, they can crystallize at higher temperatures or under energetic ion bombardment conditions [65, 66].

The principal characteristics of optical coatings, namely the refractive index and hardness of the most frequently studied PECVD materials, are summarized in Figure 9.12, where they are compared with those of the widely used PVD films. The values presented refer to published data, and clearly demonstrate film quality suitable for optical system fabrication. For comparison, we also include data pertaining to the most common substrate materials: silicon, fused silica, and float glass, as well as PC, PMMA, and PET, which are increasingly used in the optics industry, since they benefit from low optical absorption ($k < 10^{-4}$ at $\lambda = 550$ nm) and enhanced mechanical characteristics (e.g. low weight and high impact resistance) [143].

Several deposition techniques aim at optimizing the energetics of the film growth, including ion bombardment effects, to obtain dense optical thin films. However, recent trends focus also on new opportunities for porous materials with well-defined porosity and pore sizes [191, 192]. These advances have been stimulated, especially, by the possibility of fabricating materials with very low n, low ε, and different levels of doping leading to birefringence, controlled pore-filling for specific optical and sensor applications, optical activity, etc. Optical design can also be simplified by taking advantage of a large difference between high and low refractive indices, $n_{\mathrm{H}} - n_{\mathrm{L}}$, possible in such structures.

Control of the film deposition process and microstructure, and adjustment of the films' passive and active optical properties, opens interesting opportunities for applications in optics,

photonics, photovoltaics, energy saving, sensors, and other related areas (see Table 9.2). In the following section, we describe examples of film performance and of industrial applications in which PECVD has been explored for the fabrication of optical interference filters (OIFs, both discrete and graded), optical waveguides, and energy transformation (solar cells, displays, and smart windows).

9.6.1.1 Optical Interference Filters

PECVD can provide n_H, n_L, and n_M materials for any simple or complex optical coating system. The design strategies can be based on three types of approach: (1) multilayer (step index) design, using two or more materials with different indices; (2) inhomogeneous (graded index depth profile, $n(z)$) design; and (3) quasi-inhomogeneous design, when very thin layers with varied composition are consecutively applied, giving properties close to that of an inhomogeneous design. Traditionally, approach (1) is most frequently used both in industry and in the laboratory, but PECVD offers new possibilities, particularly in design strategy (2), which can also provide the added value of enhanced mechanical and tribological performance. In the following, we document this situation by selected examples.

Ophthalmic lenses and light assemblies (e.g. indoor reflectors, car light bezels) are probably the most well-known applications of optical coatings, specifically in situations in which plastic substrates are used, and for which PECVD has also been extensively explored. This application has a long history, but remains very active, owing to numerous challenges. These are related not only to the optical properties, but particularly, to the mechanical and tribological performance, which includes adhesion (affected by a two orders of magnitude difference between the coefficients of thermal expansion of the inorganic coatings and the plastic), scratch and wear resistance, and other functionalities [143 and references therein]. It is estimated that in the USA alone, 160 million people wear glasses, 80 million pairs of glasses are purchased every year, and more than 90% of the lenses are plastic. Low index PMMA ($n = 1.49$) has been considered for such applications since the 1930s, but it was dialyl diglycol dicarbonate, known as CR39 (trademark of the PPG company) that became popular after World War II, while high-index PC ($n = 1.59$) has increased in importance since the 1980s, owing to its toughness, impact resistance, and thermal stability [193].

Plastics are soft, requiring hard coats to protect them. This is most frequently achieved by dipping, spinning or spraying 3–5 μm thick silica-type materials. The original, brittle, films have been replaced either by thermally cured polysiloxanes, which contain organosilane modifiers, leading to less brittleness due to the cross-linking of the organic component, or by UV-cured urethane/acrylate hard coats, which provide better adhesion but lower hardness [193]. Promising hard coats have also been fabricated by PECVD, using organosilicone precursors [194, 195]. In this case, control of film growth allows one to enhance adhesion to the soft substrate by adjusting the gradient from organic to inorganic character by, for example, changing the oxygen content [195]. In addition, optical interference between the

substrate and the hard coat can be reduced by depositing an optical matching layer ($n_{PC} = 1.59 > 1.52 > 1.46 = n_{SiO_2}$). Evaluation of mechanical properties of hard coat materials, using the scratch test method, pointed out the importance of controlling the interface properties [87, 196].

In many cases ophthalmic lenses are provided with AR coatings whose major role is to reduce double (ghost) images and back-side reflections. In this context, AR coatings are the most frequently used OIF systems, typically consisting of three to five layers, for the visible region [197]. However, they have also made their way into applications in the NIR (optoelectronics and solar cells), particularly using SiN_x and *a*-C:H, or deep UV (for 248 and 193 nm lithography), in order to reduce interference effects (using TiO_2 and Si-rich SiN_x) (for review, see [7]). In the context of ophthalmic lenses, PECVD AR films have also been investigated [198, 199], as an alternative to the more commonly used ion-beam and plasma ion-assisted deposition techniques [143].

When AR coatings are deposited directly onto a polymeric substrate, special care needs to be taken in relation to adhesion [143, 181] and to the presence of an interphase, as described in Section 9.5. For example, in the case of a four-layer AR system on PC [200], an optimized 'W-shape' design between 450 and 650 nm, using $SiN_{1.3}$ and SiO_2 as n_H and n_L materials, brought the original single-side reflection of 5.0% down to about 0.8%. However, corrections had to be introduced into the design to account for the presence of the interphase adjacent to the first n_H layer (see Figure 9.21). Benefiting from the knowledge of the existence of such an interphase, a reoptimized design was then capable of further reducing the overall reflectance.

In many instances the lenses are provided with top coats which are highly repellent to water and dust. These may be either hydrophobic or hydrophilic, but must be very thin (5–10 nm), so as not to contribute an additional optical effect. Hydrophobic top coatings are frequently obtained from wet solutions (by dipping) or by evaporation, but PEVCD films of PPFC ($n = 1.38$) have also shown promising results [201]: surface water contact angles for PECVD and non-PECVD coatings appear comparable, but the former exhibit better long-term stability, possibly due to their higher cross-linking. Good smudge resistance has also been reported for organosilicones with well-controlled O_2 concentrations and discharge power levels [194].

PECVD is well suited to the fabrication of inhomogeneous (graded-index) OIFs such as broadband AR quintic layers or rugate filters. In such cases, the n value is continuously varied between n_H and n_L, mostly by changing the gas composition [107, 146, 202], although variation of film density (or porosity) by changing the bias potential is also possible [192]. In such an approach, at each instant of the deposition process, the $n(\lambda)$ dispersion and r_D value must be known. A material well suited for such coatings is SiON (Figure 9.13), but TiO_2/SiO_2 [146], porous/dense $SiN_{1.3}$ [192], and Si-rich SiN_x [203, 204] systems have also been tested with success; specific examples illustrating the level of materials and process control that has been achieved are described below (see Figures 9.23 and 9.24).

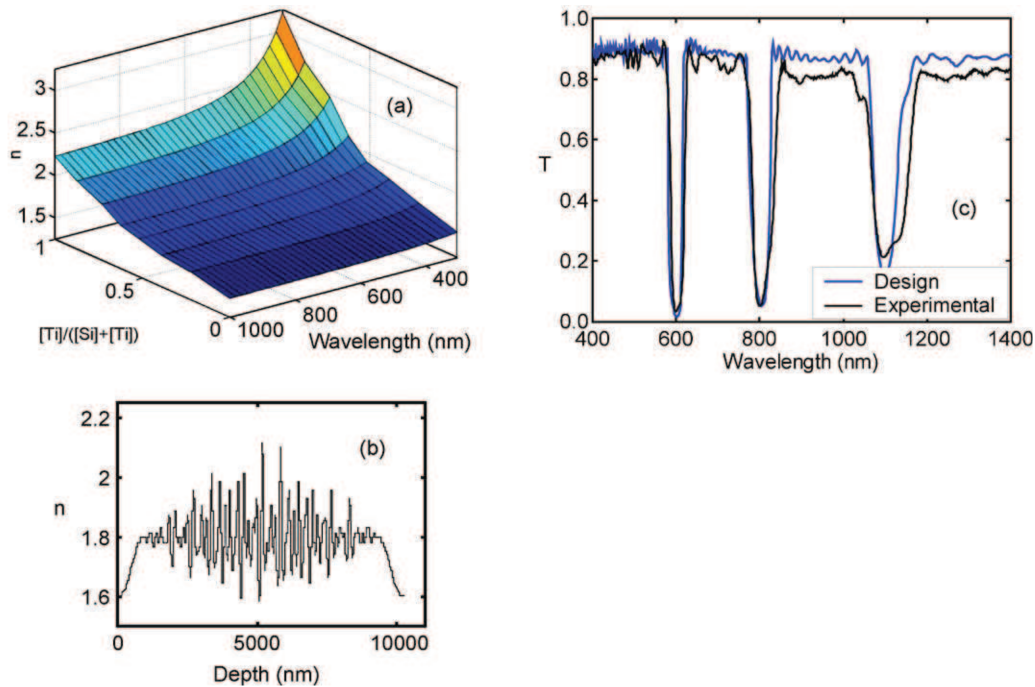

Figure 9.23: PECVD optical coatings based on TiO_2 and SiO_2: (a) refractive index dispersion curves for different TiO_2/SiO_2 compositional ratios; (b) refractive index depth profile for a sample three-band rugate filter; (c) measured and designed optical transmission of a three-band rugate filter with a refractive index depth profile from (b). (After [146, 205].)

Fabrication of a rugate filter starts with the establishment of $n(\lambda)$ dispersion curves corresponding to the materials of choice; an example is shown here for a mixture of TiO_2 and SiO_2 controlled by the flow-rate ratio of precursors, such as $TiCl_4$ and $SiCl_4$ (Figure 9.23a). Following the filter design (using a software specifically developed for graded coatings [206]) of a three-band inhomogeneous (rugate) filter as an example (Figure 9.23c), the desired $n(z)$ profile is rather complex owing to the existence of three peaks, continuous variation of n, apodization and incorporation of quintic layers at the filter–substrate and filter–air interfaces (Figure 9.23b) [205]. Such a filter, with a total thickness of about 10 μm, has been successfully reproduced, as documented by the comparison of the measured transmission spectrum with the design target (Figure 9.23c). Similar filters have also been fabricated using SiON, including on substrates such as glass and plastic [7].

In addition to their optical characteristics, such filters offer additional advantages due to their improved mechanical behavior, related to the absence of abrupt interfaces and to the uniform distribution of stress, particularly enhanced adhesion and scratch resistance [207, 208].

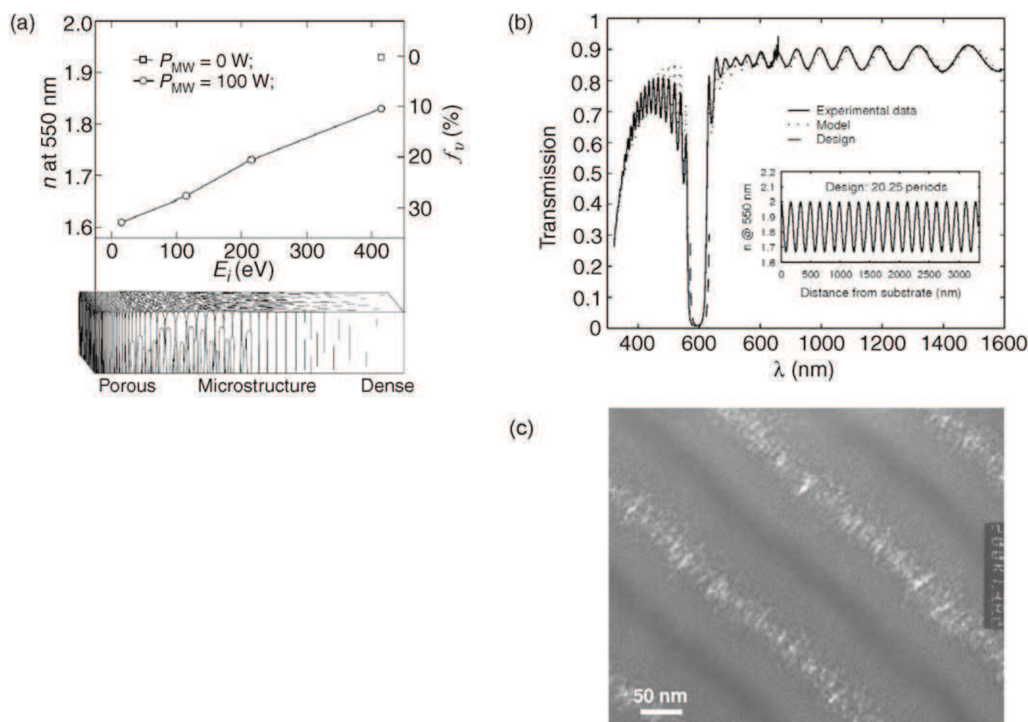

Figure 9.24: Single-material optical coatings based on the control of porosity in $SiN_{1.3}$ films: (a) variation of the refractive index and of the void volume fraction as a function of E_i in a MW/RF discharge; (b) optical transmission of a dense/porous graded (rugate) filter based on the continuous variation of *n* (see insert); (c) TEM micrograph of the filter in (b). (After [192, 209].)

The following example illustrates a possibility of tuning plasma–surface interactions in order to obtain a controlled $n(z)$ profile by changing the film microstructure (Figure 9.24). Controlling ion bombardment in the growth of $SiN_{1.3}$ films (by adjusting the surface bias or the duty cycle in a pulsed plasma as illustrated by the IEDF in Figure 9.7) allows one to vary n from 1.50 to 1.90, owing to the control of the film porosity (Figure 9.24a). This makes it possible to prepare (discrete) multilayer and inhomogeneous (rugate) filters (with a continuous sinusoidal variation of $n(z)$) using one single material. Such filters have been designed and fabricated, and examples of the corresponding $n(z)$ profile, optical transmission spectrum, and TEM micrograph are shown in Figure 9.24(b) and (c) [192, 209].

9.6.1.2 Optical Waveguides

Research on plasma-deposited optical waveguides for integrated optics began in the early 1970s, and has continued until now, with the aim of further improving their performance (low optical loss), increasing the deposition rate, and making them part of sophisticated integrated

optical systems. In most cases the goal has been to fabricate waveguides on silicon substrates, where the cladding layer is a thermal- or a plasma-deposited film of silicon dioxide, followed by a patterned waveguiding core layer [7, 111, 210, 211]. Direct comparison of the reported optical loss values is rather difficult because of different measuring techniques and device concepts: for example, the difference, Δn, between n values of the core and the cladding layers determines the number of inner reflections in the waveguide and the depth of field penetration into the cladding. For smaller Δn, the effect of light scattering by surface (or interface) roughness becomes more important while, in turn, the cladding layer may be thinner, and the evanescent wave is not attenuated by the Si substrate.

In this context, SiON offers a good tradeoff between compactness, fiber match, fabrication complexity, and the possibility of combining optical and electronic components on one chip. As the most frequently used core-layer material, SiON is obtained from SiH_4 mixed with N_2O or O_2, but depositions using $SiH_4/N_2O/NH_3$ or $SiH_4/N_2O/N_2$ mixtures, or with $SiN_{1.3}$ from SiH_4/NH_3 have also been studied [212, 213]. Although n in SiON can vary between 1.45 and 1.90, a lower n range ($n < 1.7$) is more suitable owing to a smaller Δn (typically $\Delta n < 0.005$), and to a reduced dependence of n on the gas flow rate ratio. Non-uniformity and run-to-run reproducibility of such optical waveguides is 1–3%, associated with inhomogeneity and reproducibility of n of 0.7–1.7% [211].

Most of the waveguiding characteristics of Si-compound films have been evaluated in the visible region, where optical losses below 0.2 dB/cm in slab waveguides and between 0.1 and 1.5 dB/cm in channel waveguides have been reported [111, 211]. In the NIR region, however, H- and N-containing films absorb, owing to the presence of O–H (at 1400 nm) and Si–H, and therefore optical losses may increase considerably (< 10 dB/cm). The concentrations of these groups can be reduced by postannealing: the O–H absorption has been found to disappear at 800 °C, while the N–H and Si–H contributions vanished only at 1100 °C, both accompanied by a substantial drop of loss. When the waveguides are fabricated on low-loss buffer layers (such as thermal SiO_2), one can change the dimensions and index of the core SiON layer and avoid the problem of IR absorption, since the light propagates mostly in the cladding [214].

In addition to SiON, other waveguiding materials and chemistries have been employed. These include SiO_2:F or SiO_2:Ge (losses typically 0.1–1.5 dB/cm, 0.027 dB/cm at 1.55 μm), but also organosilicones, organometallics (Al_2O_3, ~ 20 dB/cm), and Er-doped epitaxial Si (for review, see [7]). PPFC ($n = 1.38$) core layers on Teflon AF cladding on Si have been considered, in view of the possibility of obtaining low optical loss in the NIR region, owing to the absence of O–H, Si–H, and N–H groups [215].

Plasma-deposited Si-compound waveguides were tested on chips of integrated optical devices, such as an interferometer pressure sensor [216], splitters [217], and in conjunction with light-emitting diodes, micromirrors, and photodetectors [218]. It should be mentioned that

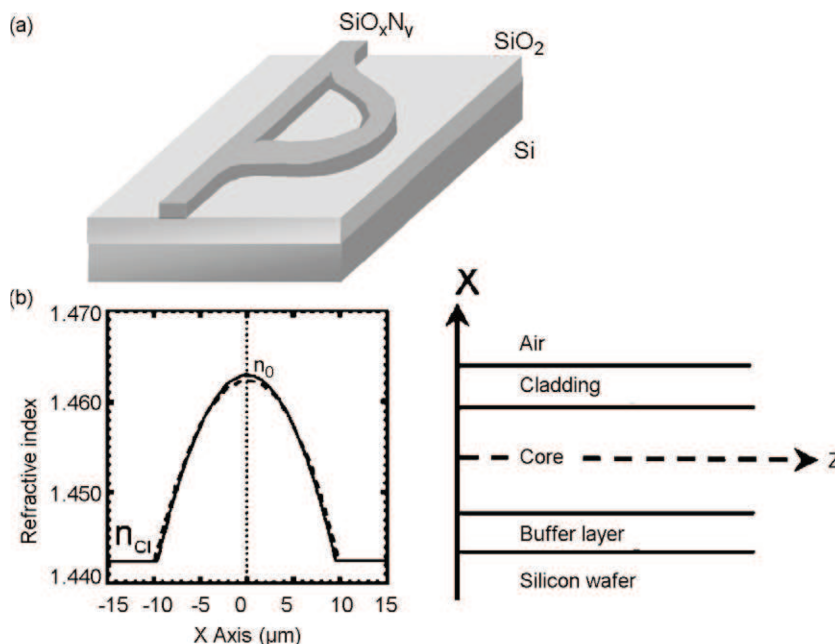

Figure 9.25: Examples of optical waveguide systems: (a) non-symmetric Mach-Zehnder interferometer sensor (after [219]); (b) structure of GRIN slab lens showing the refractive index profile and the layered structure (after [220]).

fabrication of such devices frequently combines several techniques, used in different steps; in addition to PECVD and RIE, these can include low-pressure CVD, sputtering, and implantation.

As an example, a non-symmetric Mach–Zehnder interferometer chemical sensor has been studied. In this configuration [219] the light propagating along the longer branch is affected more by the surrounding medium, whose refractive index is determined by its composition (e.g. gas or liquid solutions) than in the shorter counterpart (Figure 9.25a). This requires fewer fabrication steps than the symmetric interferometer sensor, which has to be equipped with a sensitizing window, but generally provides reduced sensitivity. Another interesting example, illustrating device fabrication, is the gradient-index (GRIN) planar slab lens on Si for use in a 1×7 coupler, or for coupling between a laser diode and a waveguide [220] (Figure 9.25b). In this case, inhomogeneously F-doped SiO_2 (using SiH_4, O_2, and CF_4; $n = 1.437–1.462$), with an approximately parabolic n profile, surrounded by a low-index buffer layer and cladding, was used, for a total thickness of about 24 μm. The layers were deposited at low temperature (< 250 °C), under ion bombardment (300 eV), resulting in a propagation loss of about 0.1 dB/cm. The advantage of PECVD in that case, compared to ion exchange, for example, is that only one fabrication step is required for fabrication of the entire GRIN lens.

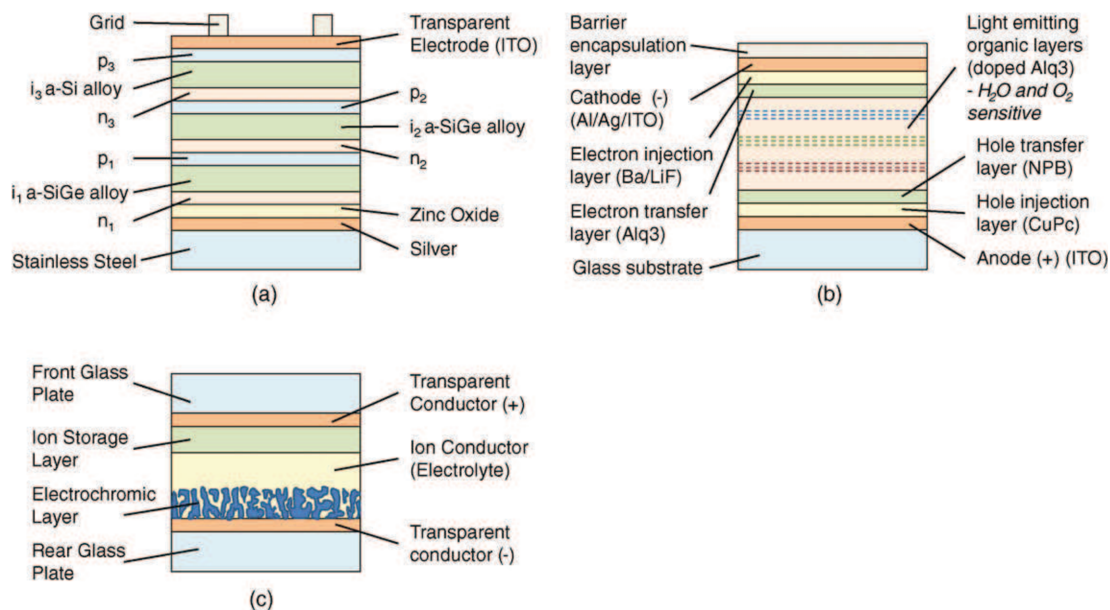

Figure 9.26: Schematic structure of active thin film devices: (a) triple-junction solar cell (after [222]); (b) thin film display (after [227]); (c) electrochromic device – smart window (after [234]).

In parallel with the integrated optics field, plasma has also been used for the deposition of Fe- or Ge-doped SiO_2 core layers on the inner surface of silica tubes for fiber optic preforms [26]. This is the first industrial use of PECVD for optical applications.

9.6.1.3 Thin Films for Solar Cells, Gas Permeation Barriers, and Smart Windows

Application of thin film technology in the fabrication of devices for energy generation, transformation, and reduced consumption has advanced rapidly with the implementation and demonstration of thin film solar cells, displays, smart windows, and numerous other devices. For all of these, the individual layers can be prepared by PECVD as indicated in the schematics in Figure 9.26, though other methods have also been successfully applied [157, 221]. The PECVD films, depending on their nature, composition, and microstructure, can fulfill different functions, such as the semiconductor layer, transparent conductive layer, barrier layer, electrochromic layer, AR coating, and possibly others.

Thin films for solar cells

Of the various thin film materials, PECVD hydrogenated amorphous semiconductors, especially silicon (*a*-Si:H), have received much attention for their use in low-cost solar cells [222]. Because of its broad wavelength range absorption characteristics (due to the inherent disorder), *a*-Si:H absorbs sunlight very efficiently, and very thin films (<500 nm) are sufficient to form the solar cell structure. The main focus has been on single- and multijunction cells

using *a*-Si:H, but *a*-SiGe:H, and more recently hydrogenated nanocrystalline silicon (NC-Si:H), have been explored [223], the latter reaching a higher conversion efficiency, η.

a-Si:H is usually prepared in glow-discharge from silane, but strong dilution in hydrogen has been found to favor formation of its NC phase. In fact, the best performing Si is grown at a dilution just below the edge of amorphous to NC transition [224], and the highest η values of NC solar cells are obtained when the hydrogen dilution pushes the material just above the edge [225]. Figure 9.26(a) shows a spectrum-splitting triple-junction structure that leads to good stability, and 13% stable AM1.5 efficiency.

The top cell using *a*-Si:H has a bandgap of about 1.8 eV and absorbs the blue photons. The middle and bottom cells, using *a*-SiGe:H alloys of different Si to Ge ratios, possess bandgaps of around 1.6 and 1.4 eV and absorb green and red photons. The nine-layer, triple-junction stack is deposited onto a thin, flexible stainless steel (SS) substrate coated with a textured silver-doped zinc oxide (Ag/ZnO) back-reflector, to facilitate light trapping. Transparent-conductive indium-tin oxide (ITO) is deposited on top of the top cell, serving as the contact as well as an AR coating. Thin and highly conductive *p*-type and *n*-type layers used in individual cells also form tunnel junctions between adjacent cells [226].

Gas permeation barriers

Permeation of gases (e.g. O_2) and vapors (e.g. H_2O) through polymers, which represents an important problem in device technology and in the packaging of various high added value consumer products, is particularly important in the context of encapsulation of organic electronic devices. These include organic light-emitting devices (OLEDs) (Figure 9.26b), organic solar cells, integrated circuits, and food and pharmaceutical products. Application of high-performance barriers can substantially extend the lifetime and performance of all of these.

PECVD SiO_2 and $SiN_{1.3}$ have received particular attention as barrier materials for polymeric substrates, mainly owing to their hardness, optical transparency [7, 184], good adhesion, and barrier properties [182, 228–230]. Films deposited by PECVD are found to be superior compared to other techniques such as PVD. Specifically, the main reason is considered to be formation of the interphase (about 50 nm thick) which is distinct in structure, composition, and mechanical properties from the coating and the substrate [185] (see Section 9.5.4).

It has been shown that oxygen transmission rate (OTR) and water vapor transmission rate (WVTR) decrease as much as 1000-fold with increasing coating thickness, to a certain asymptotic minimum value, when the thickness exceeds a ‘critical’ value, d_c, that has been estimated at $\sim$15 nm for SiO_2 and $\sim$8 nm for $SiN_{1.3}$, for which useful barrier characteristics can be achieved [182, 229, 230]. Typically found OTR values are about 0.5 scc/m^{2}day and WVTR about 0.3 g/m^{2}day, for barrier thicknesses exceeding such d_c, but the minimum permeation values depend on the concentration of defect sites in the coating and on the substrate surface roughness.

In order to mitigate the effect of defects, multilayer systems are applied (ultrabarrier coatings) to benefit from best performance of individual layers, and to minimize defects and pinhole concentration [230]. They typically combine two or more layers deposited by one process (e.g. PECVD), or by a hybrid process including fabrication of a smoothening layer (e.g. by evaporation) followed by a dense PECVD coating [231–233].

Electrochromic devices

An example of an electrochromic (EC) device is illustrated in Figure 9.26(c). It typically contains five layers between two substrates formed by glass or plastic. It features two transparent electrodes, an EC layer, such as WO_3, an electrolyte, and an ion-containing layer. The latter coating can eventually be also replaced by another EC layer that possesses properties inverse with respect to the former one [234]. For appropriate function of such a device, an EC film with controlled porosity is generally required. This can be achieved by appropriate control of film growth conditions, including medium-energy ion bombardment [156, 158] in conjunction with the structural evolution described by the SZM (see Section 9.5).

9.6.1.4 Industrial Scale-Up and Economic Considerations

It has become apparent that PECVD techniques can provide optical properties comparable to other techniques such as PVD, and the final choice of the deposition approach for each specific application depends on both technical and manufacturing factors. These include: (1) mechanical properties (e.g. adhesion and stress); (2) deposition rate; (3) process scale-up (uniformity, reproducibility, etc.); (4) process integration in the optical device fabrication; (5) manufacturing yield; and (6) cost of manufacturing (capital investment and operation). From this point of view, novel plasma-based processes, offering the possibility of selectively controlling E_i and Φ_i/Φ_n and frequently providing high r_D values, are advantageous. Furthermore, PECVD offers good mechanical performance and the possibility of pretreating or 'engineering' interfaces (e.g. in the case of plastic substrates).

Different plasma system concepts have been proposed for the fabrication of optical coatings. In general, the characteristics of a suitable plasma reactor are dictated by the requirements of the desired optical coating, in which the decisive factors are the choice of the n_H and n_L materials, control and reproducibility of $n(z)$, the component size and required film uniformity, and the total film thickness. In addition, the deposition rate is a tradeoff between factors such as film microstructure, film stress, and precision of the thickness control. Uniformity better than 1% over more than 50 cm can be achieved, while a deposition rate of 1–5 nm/s is a good practical value for high-quality (dense) optical coatings. It should be noted, however, that such considerations are very general, and specific aspects depend on the device to be fabricated. For example, the total thickness of AR coatings in the visible region is about 0.4 μm, while a narrowband filter in the NIR composed of more than 100 layers may be 50 μm thick or more, as compared to about 10 μm thickness for a homogeneous monomode optical waveguide.

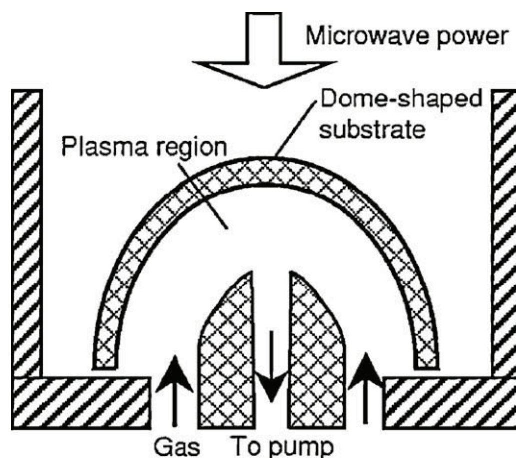

Figure 9.27: MW PICVD deposition system: schematic of the commercial reactor for coating individual lamps. (After [25, 26].)

Careful optimization is required in order to accommodate specific substrate materials (glass, polymers, etc.), sizes, and shapes (flat, curved, rough).

Despite considerable efforts to develop novel optical film materials using PECVD, there are relatively few publications documenting its use in industry. Significant among them appears to be the PICVD process of Schott Glaswerke GmbH (see Section 9.3.3), illustrated in Figure 9.27. This approach, in which the substrate forms part of the reactor walls, was originally developed to coat the inner surface of glass tube for fiber preforms, and is used to fabricate cold light reflectors for projection lamps and IR reflectors for energy-efficient lamps, as well as waveguides, and transparent barrier coatings [26]. Large production (several million lamps per year) is achieved by increasing the total number of small deposition chambers. Another example concerns a microwave PECVD used for the medium- and large-scale roll-to-roll deposition of AR coatings onto webs [235].

Commercialization and adoption of PECVD have been often hampered by high manufacturing cost. In order to avoid risks and unforeseen surprises, it is desirable to explore economic models allowing one to compare the PECVD process with other alternative technologies. An interesting example of such a study [236] has been performed for the particular case of tungsten oxide, which attracts much attention owing to its applications, such as smart windows, gas sensors, and displays [157].

The study compares the costs of manufacturing of WO_3 films deposited either by PECVD using an RF discharge or by DC reactive magnetron sputtering from metal targets, and it considers both inline systems for large area (2 m wide) glass substrates and roll-to-roll systems for flexible webs [236]. Assuming $r_D = 10$ nm/s (confirmed experimentally in a static mode),

the model PECVD process was predicted to give the best performance with the roll-to-roll system at a cost of $5.26/m^2 and an annual capacity of 1.4 million m^2, while the cost was dominated by raw materials (primarily WF_6). On the other hand, the model DC sputtering process at $r_D = 0.6$ nm/s was predicted to give the best performance with the roll-to-roll system at a cost of $15.00/m^2 and an annual capacity of 0.12 million m^2, and the cost was found to be dominated by labor and depreciation.

The study concludes that PECVD can produce WO_3 for as little as one-third the cost, and have more than ten times the annual production capacity of sputtering. However, in such situations, one has also to consider other (hidden) expenses related to handling potentially toxic and corrosive products, safety, and long-term projections of the cost of raw materials. Such approaches are well illustrated by examples from the area of microelectronics [188].

Examples of commercial processes using PECVD include both vendors and end users who apply high-frequency plasmas for the fabrication of coatings with specific optical, electrical, and barrier characteristics. By way of illustration, one type of commercial plasma machine using both MW (an array of linear plasma sources) and RF discharges is available in Germany (Roth & Rau AG) (Figure 9.28). The system allows one to coat areas up to 0.5×0.5 m^2 with transparent multilayer barriers, AR coatings, and other related systems, and it also provides a possibility for uniform etching in microfabrication.

United Solar Ovonic has developed a roll-to-roll automated process for manufacturing solar cells on stainless steel (SS). Rolls of SS substrates, 2500 m long, 36 cm wide, and 125 μm thick continuously move through four compartments to perform (1) washing, (2) back-reflector

Figure 9.28: Large-area PECVD coating system for the fabrication of barrier and antireflective coatings over an area of up to 55 cm × 55 cm. (Courtesy of Roth & Rau.)

Figure 9.29: Large-area roll-to-roll deposition system for the fabrication of amorphous silicon triple-junction photovoltaic cells. (Courtesy of United Solar Ovonic.)

deposition (sputtered Al and ZnO), (3) PECVD of the triple junction alloy consisting of nine layers of *a*-Si and *a*-SiGe, and (4) AR coating deposition (ITO). The complete thin film solar cell device is illustrated in Figure 9.26(a), and the production machine is shown in Figure 9.29. The system is approximately 90 m long and 3 m tall; it contains a vertical central cathode, and three webs are transported on each side of the cathode parallel to it at a speed of 30 cm/minute. Deposition of 14.5 km of solar cells can be completed in about 72 hours.

9.6.2 Protective Tribological Coatings

In recent years we have witnessed an increasing need for protective coatings with improved durability and performance, preventing wear in dry and wet (tribocorrosion) conditions, erosion and corrosion, and providing environmental protection and thermal insulation. There have been considerable advances in the understanding of the mechanisms of wear and corrosion of coatings particularly related to the characteristics of film microstructure, interface properties, and wear and corrosion mechanisms.

The need to ensure good adhesion to numerous technological substrates has stimulated much research, exploring different interface engineering approaches, in order to improve the tribomechanical and tribocorrosion characteristics of coating–substrate systems. Specifically,

numerous applications call for so-called duplex or triplex treatments (usually performed in the same reactor) to stabilize the interface by affecting its composition and microhardness, and frequently introducing property gradients such as hardness [176]. The commonly used methods consist of two or three of the following independent steps: (1) surface treatment in an active (non-deposition) plasma containing nitrogen, carbon, boron, or other gases, leading to surface nitriding, boriding, or carburizing, and generally giving to surface hardening; (2) deposition of an intermediate layer, usually metal or metal compound; and (3) deposition of the final, hard, protective tribological coating [175, 237].

In many respects, the protective coatings are categorized according to their hardness as described in Section 9.5 and illustrated for PECVD materials in Figure 9.12. However, tribological behavior of functional coatings is rather complex, and other material properties, such as Young's modulus, toughness, thermal conductivity, stress, friction coefficient, and density, have to be taken into account in order to optimize the coatings' desired performance in terms of wear, erosion and corrosion resistance, and other functional characteristics. In addition, since the material behavior under stress conditions is generally governed by a specific failure mechanism, the coating performance frequently depends on the test conditions for each particular application.

In general, for tribological coatings, H and μ have usually been considered primary properties affecting the wear resistance. However, it has recently been recognized that energy dissipation when two bodies are in relative motion is of primary importance [238, 239]. This allows one to link the tribological properties with the materials' elastoplastic characteristics in two ways: (1) the H/E ratio representing the 'plasticity index' or elastic strain to failure; this appears to be a suitable parameter for predicting wear resistance (K) and for explaining the deformation properties of surfaces in contact [240], by considering the elastic rebound; and (2) the H^3/E^2 ratio – known as resistance to plastic deformation or resilience – that appears to be a key parameter for predicting the tribological behavior [241] as well as the toughness of the coatings [239, 240, 242].

In this section, we describe selected examples of the performance of different tribological coatings, in the context of their applications in aerospace, automobile industry, manufacturing, and biomedical instrumentation (see Table 9.2). We focus particularly on metal-based polycrystalline, nanocrystalline and nanocomposite coatings, and then on covalently bonded amorphous carbonaceous coatings which, in numerous cases, have reached industrial scale.

9.6.2.1 Metal-Based Tribological Coatings

Binary metal nitrides, carbides, borides, and oxides are frequently used in different tribological applications including cutting tools, protection of different components of automobiles, aircrafts, and consumer products. Their most attractive characteristic is a combination of hardness with high wear, erosion and corrosion resistance, while some of them

provide attractive colors and other advantageous functional characteristics. Such coatings are traditionally fabricated by CVD and PVD methods, but PECVD is increasingly taking its place because of the possibility of benefiting from the plasma chemical reactions, plasma–surface interactions, and interface engineering at low temperature.

In order to broaden the range of the film properties suitable for different applications, and especially to benefit from synergistic effects, ternary metal compounds (mostly including metal carbon nitrides), nanocomposites, and nanolaminate structures (multilayers formed by several to several tens of nanometer thick individual layers) appear to satisfy the ever increasing requirements.

In the context of aerospace and avionics applications, commercial, military, rescue or humanitarian aid aircraft or helicopters frequently operate in a hostile environment, in high humidity and marine salt concentrations. They may operate in the presence of aggressive chemicals, in heavily polluted regions, where the air can carry dust, sand particles, volcanic ash, and other compounds. Such conditions contribute to increased erosion and corrosion of aircraft engine components. This generally leads to decreased efficiency and increased fuel consumption, and can eventually result in catastrophic failure. Therefore, frequent inspections and parts replacements are necessary. These contribute to downtime and increased machine operation costs. Application of high-performance erosion-, wear-, and corrosion-resistant protective coatings can significantly extend the lifetime and performance of aircraft engine components and helicopter parts and thus lead to major reductions in maintenance costs, and to improved safety.

Examples of the wear properties of TiN-based coatings deposited onto martensitic 410 stainless steel are shown in Figure 9.30(a). In order to enhance adhesion, the hardness of the steel ($H = 5$ GPa) has been gradually increased at the interface by nitriding the near-surface region (to a depth of several μm, $H = 15$ GPa), followed by the deposition of 1 μm thick TiN ($H = 24$ GPa), on which 4 μm thick nc-TiN/SiN, nc-TiCN/SiCN coatings have been prepared ($H = 35$–42 GPa; triplex process) [237].

The figure shows that nc-TiCN/SiCN exhibits superior tribological properties compared to TiN and to nc-TiN/SiN coatings, such as low friction ($\mu = 0.17$ compared to 0.5 for the former two coatings) and low wear rate ($K = 1.6 \times 10^{-7}$ mm^3/Nm compared to 9.5×10^{-6} mm^3/Nm for the former coatings). The nc-TiCN/SiCN thus allows one to reduce wear by a factor of ~ 600 compared to bare SS410. It has been proposed that this performance is due to higher hardness, higher elastic rebound, and lower friction due to the presence of carbon-containing, flexible, Si–C and C–N bonds in the tribolayer [237]. In addition, the presence of carbon leads to attractive color changes compared to nc-TiN/SiN and to the traditional gold color of TiN [167].

The significant effect of applying nc coatings onto aerospace components has also been found by evaluating the erosion resistance (ER), following the ASTM G76 standard. As illustrated in

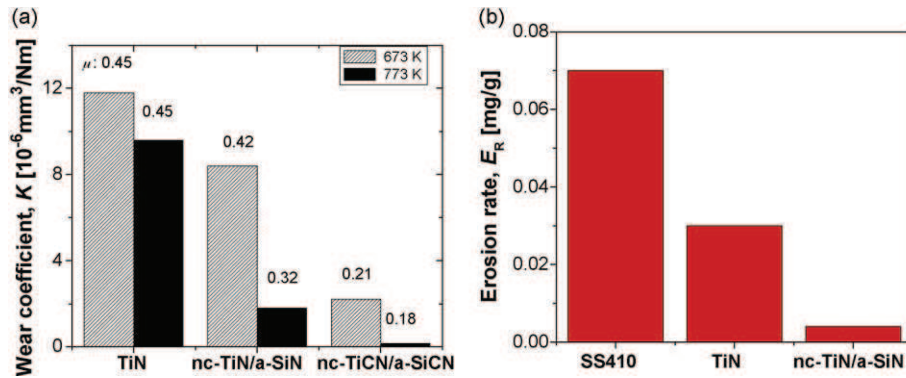

Figure 9.30: Tribological properties of TiN and nanocomposite nc-TiN/$SiN_{1.3}$ and nc-TiCN/SiCN films deposited at T_s of 673 K and 773 K, compared to: (a) the wear coefficient, *K*, and the coefficient of friction, μ (after [237]); (b) solid particle erosion rate of the coatings deposited on 410 stainless steel (Al_2O_3 particles, diameter 50 μm, speed 80 m/s) (after [243]).

Figure 9.30(b), application of PECVD TiN, nc-TiN/SiN, and nc-TiCN/SiCN films resulted in an increase of ER by a factor of 20, compared to uncoated SS410 substrates.

As discussed above, assessment of the tribological properties of coatings with respect to their elastoplastic characteristics opens the possibility of better prediction and optimization of their performance. In this context, the *K* and ER values of the TiN-containing coatings from Figure 9.30 are related to the H^3/E^2 ratio in Figure 9.31. It has been concluded that a substantial improvement in the film's tribological behavior (e.g. erosion and wear) occurs for $H^3/E^2 > 0.5$ GPa (or $H/E > 0.15$–0.20) [237, 243].

Recently, the $H^3/E^2 > 0.5$ GPa condition has also been predicted for such a tribological situation (Al_2O_3 erodent particles, 50 μm size, 85 m/s velocity) based on finite element calculations using a model considering tensile and shear stress, and yielding criteria for failure upon particle impact [244]. In other words, there is now growing evidence that a critical H^3/E^2 ratio (or *H/E* ratio) has to be satisfied for the coating to provide appropriate tribological protection. It also means that for successful tribological applications the H^3/E^2 and *H/E* ratios of the used materials should be maximized. In reality, it is generally important to ensure that the coating hardness is sufficiently higher than that of the eroding or wearing medium, but the *E* value should be minimized. Therefore, film microstructure should be adjusted to satisfy such conditions: in this respect, PECVD metal-based nc coatings are very suitable candidates for many surface engineering and tribological solutions.

9.6.2.2 Covalently Bonded Protective Carbonaceous Coatings

Carbonaceous tribological coatings have become very attractive because of their very low friction, chemical inertness, and biocompatibility. They have already established their

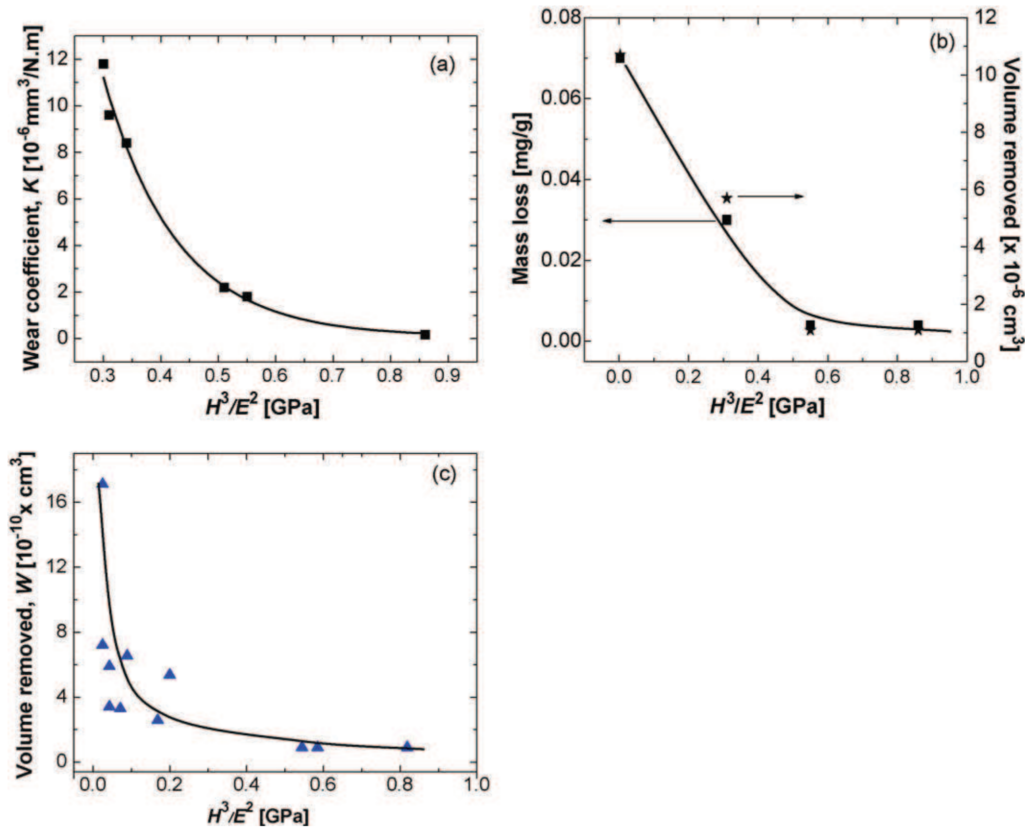

Figure 9.31: Tribological characteristics of TiN and nanocomposite nc-TiN/SiN$_{1.3}$ films as a function of the H^3/E^2 ratio: (a) wear coefficient (after [237]); (b) erosion rate (after [243]); (c) volume removed under single particle erosion (finite element modeling) (after [242]).

importance to the automobile sector, for reduced friction in engines, as sliding, hard, and optically transparent coatings in optics (e.g. barcode readers), and show much promise for biomedical applications (for review, see [245]).

In many cases, before a particular application is tested, frequent problems related to adhesion have to be solved, especially when dealing with metallic, non-carbide forming, substrates. In this respect, adhesion enhancement can be achieved by surface treatments using nitriding and carburizing, as in the case of metal compounds presented above [175–178]. Alternatively, intermediate layers may be applied (duplex or triplex processes). Among the latter, amorphous Si or metal-carbides [246] appear to be the most successful adhesive layers, for steel or non-ferrous metal substrates (e.g. Ti-6Al-4V, WC-Co), under dry sliding conditions.

When corrosion and wear are simultaneously involved, their synergistic action significantly degrades the performance of the materials in contact. Such situations occur, for example, in

orthopaedic applications, such as artificial joints (e.g. hip and knee prosthesis), where the bearing surfaces subjected to sliding wear are immersed in the body fluid, so that corrosion is also a significant concern. For such applications, the coated metals and alloys must possess high tribocorrosion resistance. Otherwise, in the case of adhesion failure of prosthetic implants, particles generated by wear may induce reactions that provoke the release of inflammatory mediators from macrophages [247]. It is well established that the cellular response to wear debris depends, among other factors, on the number, shape, size, surface area, and materials chemistry of the particles, thus contributing to complex tribocorrosion reactions [248, 249].

It has been shown that applying a nitrided interface to DLC-coated medical-grade 316L stainless steel provides a significant improvement of the dry wear resistance [177]. However, this bond layer is insufficient when sliding wear takes place in body fluid conditions, even at low contact pressure. This was found to be mainly due to the infiltration of liquid through pores and the weakening of the interface owing to corrosion processes. In such case, the use of PECVD $SiN_{1.3}$ as an interface layer has been found to significantly improve wear resistance of DLC films in Ringer's solution [179]. By acting simultaneously as an adhesive and corrosion barrier layer, the $SiN_{1.3}$ film largely reduced the infiltration of liquid through the film and, hence, the possibility of interface weakening.

As an example of tribocorrosion behavior, OCP measurements were used to follow, in situ, the degradation of DLC-coated 316L stainless steel exposed to Ringer's solution, and the results are shown in Figure 9.32(a). A drop in the OCP indicates removal of the DLC layer and exposure of the active metal to the environment. Moreover, the OCP measured during the

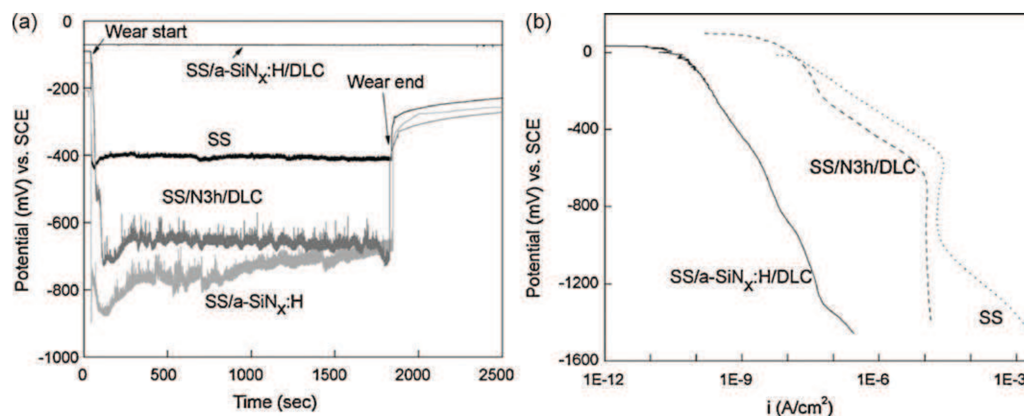

Figure 9.32: Tribocorrosion behavior of DLC-coated biomedical substrates exposed to Ringer's solution: (a) open circuit potential measurements during and after the reciprocal sliding test of SS, SS/N3h/DLC, SS/a-SiN_x:H, and SS/a-SiN_x:H/DLC; alumina ball, normal load: 9 N; frequency: 1 Hz; (b) cathodic polarization curves of bare SS and SS/N3h/DLC and SS/SiN/DLC coating systems. (After [179].)

tribocorrosion experiments was shown to strongly depend on the cathodic reaction rate on the unworn area; a slower rate of cathodic reaction resulted in lower potential during wear. Without an $SiN_{1.3}$ interlayer, OCP drops rapidly within the first tens of cycles of sliding, indicating complete removal of the coatings. When $SiN_{1.3}$ is present, the OCP remains constant during and after the wear test, while μ remains almost constant (0.08) throughout the entire sliding test.

As shown by the cathodic polarization curves in Figure 9.32(b), the presence of DLC and of the DLC/$SiN_{1.3}$ double layer decreases the current density. In addition, the curves show that the $SiN_{1.3}$ film significantly reduces the rate of the cathodic reaction, and therefore explains the low value of OCP measured for $SiN_{1.3}$ and DLC/$SiN_{1.3}$ during the sliding test.

In certain situations, lubricious coatings are needed to be applied on soft substrates, in the case of specific medical, pharmaceutical, or healthcare products. As an example, organic PECVD coatings obtained from MW discharge have been applied for enhanced tribological performance of hearing devices, which need to be inserted into the ear many times without long-term deterioration and skin irritation. In such a case, plasma-deposited organosilicone coatings were applied to silicone rubber components, and their surface friction has been assessed as a function of thickness (deposition time) (Figure 9.33). It has been shown that an equivalent of several hundreds of nanometer thickness is sufficient to ensure suitable long-term lubricity (the μ dropped by a factor between 5 and 10 compared to uncovered rubber), while providing a conformal coating on the substrate surface as confirmed by SEM (Figure 9.33b, c).

9.6.2.3 Industrial Scale-Up

Among possible PECVD processes, acceptance of hard carbon protective coatings by industry is probably most advanced, compared to other film systems. The main reasons appear to be the relative ease of fabrication from hydrocarbon gases and precursors, most frequently using methane, acetylene, or benzene, relative tolerance regarding the film thickness, stability of the process itself, and the fact that most of the deposition equipment is used to batch coat individual sets of differently shaped components. The use of DLC is very advanced in the automotive sector, where DLC coatings were already introduced by 1994, for diesel engine injection systems, followed by piston rings and tappets. Its use in racing cars, gears, and other components has been considered, and applied, since the 1990s (for detailed description, see [245, 251]).

An example of an industrial system, developed by Hauzer Techno Coating (the Netherlands), for DLC coatings onto automobile and other components is shown in Figure 9.34. The turbomolecularly pumped reactor contains six electrodes, up to 1.6 m long, for pulsed discharge excitation, and allows both PECVD and PVD processes to be combined in one chamber.

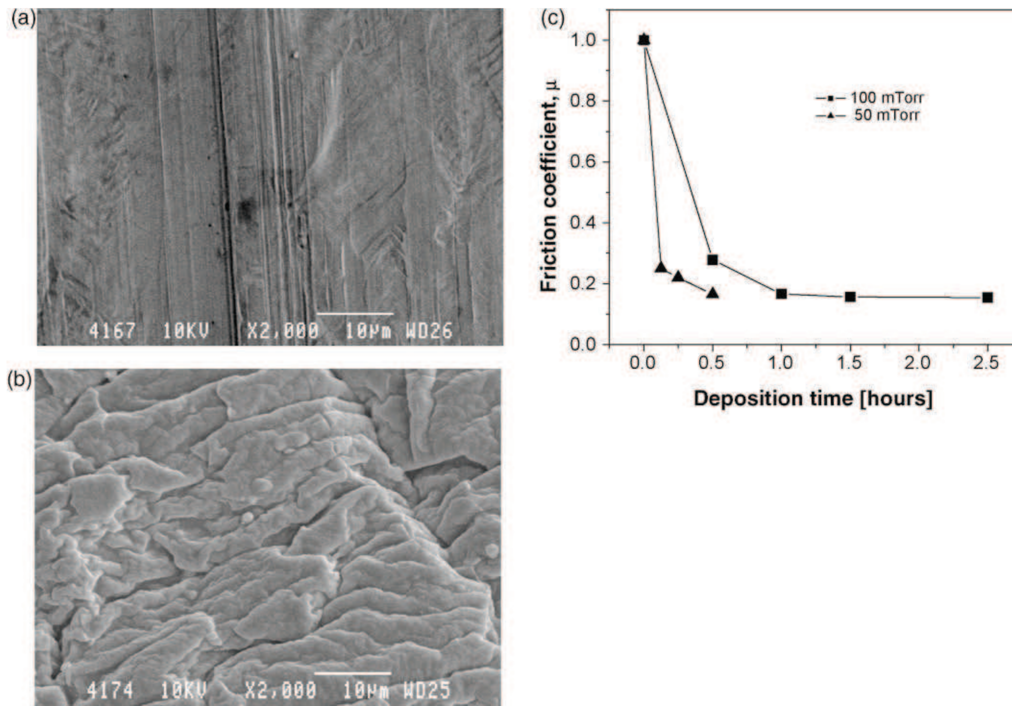

Figure 9.33: Effect of lubricious organosilicone protective coatings on the reduction of friction coefficient of multiusage hearing devices: SEM micrographs (a) before and (b) after coating; (c) coefficient of friction as a function of coating time. (After [250].)

Figure 9.34: Industrial multizone deposition system for the fabrication of DLC coatings for automotive parts and other applications. Each chamber contains six 1.6 m long electrodes. (Courtesy of Hauzer Techno Coatings.)

Figure 9.35: Example of a commercial system for the deposition of hard protective coatings. (Courtesy of PATT Technologies Inc.)

An interesting approach to the fabrication of metal nitrides, carbides, and borides as single layers, multilayers and nanolaminates has been developed and explored by PATT Technologies Inc. (Canada) (Figure 9.35). This producer fabricates such Ti-based and other metal-based coatings from metal halide precursors, specifically prepared in a furnace adjacent to the deposition chamber, using a reaction of solid metal with the halogen, such as Cl_2. Each chamber, of 1.6 m^3 volume, allows about 1600 kg of parts to be coated in one run, using high-power, medium-frequency pulsed plasmas.

Other concepts of deposition systems exist, each of which must be examined using an economic model related to the capital and operation costs, deposition rate at the given film quality, and potentially ‘hidden’ costs related to safety, precursor, and exhaust handling.

9.7 Future and Perspectives

During the past several decades, vacuum-based technologies for functional coatings have evolved significantly. Numerous PECVD concepts are industrially applied for optical, tribomechanical, protective, biomedical, and other applications. In each instance, recent advances in understanding the deposition processes and improved process control led to better

film performance. This clearly gave rise to continuously increased acceptance of PECVD technologies in industry.

Physical and chemical understanding of the basic science underlying various deposition processes is now quite advanced. In this chapter we have underlined the key factors affecting the control of film microstructure: plasma density, and ion energy and ion flux. It has also been clearly shown that, when appropriately optimized, all of the deposition processes described here produce functional thin films possessing characteristics comparable with, or even better than PVD counterparts. Therefore, the final choice of the appropriate process will depend on other factors, such as those related to different scale-up issues and economic aspects.

Current trends point toward the invention of new and improved deposition approaches, in particular those focusing on creating nanostructured coatings for various new products. By tailoring the nanostructure and controlling the interfaces between layers and substrates the engineer can create new film systems for a variety of specific applications, including active optical filters (tunable filters, smart windows, etc.), displays, sensors, security devices, energy-conversion and energy-saving devices, optical MEMS, nanophotonic devices, active optical waveguides, protective coatings for aerospace, automobiles, and biomedical components, as well as numerous consumer products. Among the emerging technologies for PECVD of functional coatings, we are already witnessing considerable progress in high-energy-content plasma processes or in those requiring a precise control of the surface growth mechanisms; these include pulsed PECVD, plasma-assisted atomic layer deposition, atmospheric pressure plasma deposition, and hybrid systems. We also are entering an exciting period that is being marked by the development of new active materials. Examples are doped transparent conductive oxides and electrochromic, photochromic, and magneto-optic materials; porous and nanocomposite materials with well-controlled nanostructural characteristics (concentration, size, and shape of nanoparticles); new organic materials; and new challenges in the area of process control and in situ real-time monitoring, smart self-healing protective coatings, and numerous others.

References

[1] T. Sugano (Ed.), Applications of Plasma Processes to VLSI Technology, Wiley, New York (1985).
[2] J. Mort, F. Jansen, Plasma Deposited Thin Films, CRC Press, Boca Raton (1986).
[3] S.M. Rossnagel, J.J. Cuomo, W.D. Westwood (Eds.), Handbook of Plasma Processing Technology, Noyes, Park Ridge, NJ (1990).
[4] R. d'Agostino (Ed.), Plasma Deposition, Treatment and Etching of Polymers, Academic Press, Boston (1990).
[5] R.F. Bunshah (Ed.), Handbook of Deposition Technologies for Films and Coatings, Noyes, Park Ridge, NJ (1994).
[6] D. Glocker, I. Shah (Eds.), Handbook of Thin Film Process Technology, IOP, Bristol (1996).
[7] L. Martinu, D. Poitras, J. Vac. Sci. Technol. A 18 (2000) 2619.
[8] Chemical Vapor Deposition, 13 (2007), special issue on low pressure PECVD.

[9] Chemical Vapor Deposition, 11 (2005), special issue on atmospheric pressure PECVD.
[10] H. Caquineau, I. Enache, N. Gherardi, N. Naude, F. Massines, J. Phys. D: Appl. Phys. 42 (2009) 125201.
[11] M.R. Wertheimer, L. Martinu, E.M. Liston, Chap. E3.0, in: D. Glocker, I. Shah (Eds.), Handbook of Thin Film Process Technology, IOP, Bristol (1996).
[12] D.M. Manos, D.L. Flamm (Eds.), Plasma Etching – An Introduction, Academic Press, Boston (1990).
[13] E.M. Liston, L. Martinu, M.R. Wertheimer, J. Adhes. Sci. Technol. 7 (1993) 1091.
[14] K.L. Mittal, L. Pizzi (Eds.), Adhesion Promotion Techniques, Marcel Dekker, New York (1999).
[15] M.J. Kushner, J. Appl. Phys. 63 (1988) 2532.
[16] M. Moisan, J. Pelletier (Eds.), Microwave Excited Plasmas, Elsevier, Amsterdam (1992).
[17] M. Moisan, C. Barbeau, R. Claude, C.M. Ferreira, J. Margot, J. Paraszczak, J. Vac. Sci. Technol. B 9 (1991) 8.
[18] L. Martinu, J.E. Klemberg-Sapieha, O.M. Kuettel, A. Raveh, M.R. Wertheimer, J. Vac. Sci. Technol. A 12 (1994) 1360.
[19] K. Okada, S. Komatsu, S. Matsumoto, J. Vac. Sci. Technol. A 17 (1999) 721.
[20] C. Pomot, J. Pelletier, Chap. 13, in: M. Moisan, J. Pelletier (Eds.), Microwave Excited Plasmas, Elsevier, Amsterdam (1992).
[21] M.A. Lieberman, A.J. Lichtenberg, Principles of Plasma Discharges and Materials Processing, Wiley, New York (1994).
[22] P. Benoit-Cattin, L.-C. Bernard, J. Appl. Phys. 39 (1968) 5723.
[23] J.W. Coburn, E. Kay, J. Appl. Phys. 43 (1972) 4965.
[24] Z. Zakrzewski, M. Moisan, Plasma Sources Sci. Technol. 4 (1995) 379.
[25] J. Segner, Chap. 7, in: F.R. Flory (Ed.), Thin Films for Optical Systems, Marcel Dekker, New York (1995) 209.
[26] H. Bach, D. Krause (Eds.), Thin Films on Glass, Schott Series on Glass and Glass Ceramics, Springer, Berlin (1997).
[27] L. Martinu, J.E. Klemberg-Sapieha, M.R. Wertheimer, Appl. Phys. Lett. 54 (1989) 2645.
[28] J.E. Klemberg-Sapieha, O.M. Kuttel, L. Martinu, M.R. Wertheimer, Thin Solid Films 193/194 (1990) 965.
[29] C. Rostaing, F. Coeuret, B. Drevillon, R. Etemadi, C. Godet, J. Huc, Thin Solid Films 236 (1993) 58.
[30] R. Etemadi, C. Godet, M. Kildemo, J.E. Bouree, R. Brenot, B. Drevillon, J. Non-Cryst. Solids 187 (1995) 70.
[31] R.R. Burke, J. Pelletier, C. Pomot, L. Vallier, J. Vac. Sci. Technol. A 8 (1991) 2931.
[32] P. Bulkin, N. Bertrand, B. Drevillon, Thin Solid Films 296 (1997) 66.
[33] M. Leskela, M. Ritala, Thin Solid Films 409 (2002) 138.
[34] S.M. Rossnagel, A. Sherman, F. Turne, J. Vac. Sci. Technol. B 18 (2000) 2016.
[35] M. Creatore, J.-C. Cigal, G.M.W. Kroesen, M.C.M. van de Sanden, Thin Solid Films 484 (2005) 104.
[36] J.W.A.M. Gielen, M.C.M. van de Sanden, D.C. Schram, Appl. Phys. Lett. 69 (1996) 152.
[37] H. Biederman, L. Martinu, Chap. 4, in: R. d'Agostino (Ed.), Plasma Deposition, Treatment and Etching of Polymers, Academic Press, Boston (1990) 269.
[38] D. Dalacu, L. Martinu, J. Vac. Sci. Technol. A 17 (1999) 877.
[39] J.-M. Lamarre, Z. Yu, C. Harkati, S. Roorda, L. Martinu, Thin Solid Films 479 (2005) 232.
[40] S. Kanazawa, M. Kogoma, T. Moriwaki, S. Okazaki, J. Phys. D: Appl. Phys. 21 (1988) 838.
[41] B. Eliasson, U. Kogelschatz, IEEE Trans. Plasma Sci. 19 (1991) 309.
[42] U. Kogelschatz, Plasma Chem. Plasma Process. 23 (2003) 1.
[43] I.H. Hutchinson, Principles of Plasma Diagnostics, Cambridge University Press, Cambridge (2002).
[44] R. Hippler, S. Pfau, M. Schmidt, K.H. Shoenbach (Eds.), Low Temperature Plasma Physics: Fundamental Aspects and Applications, Wiley-VCH, Berlin (2001).
[45] F. Chen, Lecture Notes on Principles of Plasma Processing, Kluwer Academic/Plenum Publishers, New York (2003).
[46] V.M. Donnelly, J. Phys. D: Appl. Phys. 37 (2004) R217.
[47] M. Kildemo, Appl. Opt. 37 (1998) 113.
[48] M. Kildemo, P. Bulkin, B. Drevillon, O. Hunderi, Appl. Opt. 36 (1997) 6352.

[49] C. Lu, A.W. Czanderna (Eds.), Applications of Piezoelectric Quartz Crystal Microbalances, Elsevier, Amsterdam (1984).
[50] A. Grill, Cold Plasma in Materials Fabrication: From Fundamentals to Applications, IEEE Press, New York (1994).
[51] H. Aguas, R. Martins, E. Fortunato, Vacuum 56 (2000) 31.
[52] P. Spatenka, H. Suhr, Plasma Chem. Plasma Process. 13 (1993) 555.
[53] O. Zabeida, L. Martinu, J. Appl. Phys. 85 (1999) 6366.
[54] M. Zeuner, H. Neumann, J. Meichsner, Vacuum 48 (1997) 443.
[55] O. Zabeida, A. Hallil, M.R. Wertheimer, L. Martinu, J. Appl. Phys. 88 (2000) 635.
[56] A. Hallil, O. Zabeida, M.R. Wertheimer, L. Martinu, J. Vac. Sci. Technol. A 18 (2000) 882.
[57] A. Hallil, O. Zabeida, J.E. Klemberg-Sapieha, M.R. Wertheimer, L. Martinu, in: Proc. 42nd Annual Technical Conference, Society of Vacuum Coaters, Chicago, IL (1999) 311.
[58] R.A. Roy, D.S. Yee, in: J.J. Cuomo, S.M. Rossnagel, H.R. Kaufman (Eds.), Handbook of Ion Beam Processing Technology, Noyes, Park Ridge, NJ (1989) 194.
[59] B.A. Movchan, A.V. Demchishin, Fiz. Met. Metalloved. 28 (1969) 653.
[60] J.A. Thornton, J. Vac. Sci. Technol. 11 (1974) 666.
[61] R. Messier, A.P. Giri, R.A. Roy, J. Vac. Sci. Technol. A 2 (1984) 500.
[62] R. Messier, J. Vac. Sci. Technol. A 4 (1986) 490.
[63] P.J. Kelly, R.D. Arnell, J. Vac. Sci. Technol. A 16 (1998) 2858.
[64] J. Musil, in: Proceedings of 8th International Symposium on Elementary Processes and Chemical Reactions in Low Temperature Plasma, Casta, Slovakia (1992) 177.
[65] J.M.E. Harper, J.J. Cuomo, R.J. Gambino, H.R. Kaufman, in: O. Auciello, R. Kelly (Eds.), Ion Bombardment Modification of Surfaces, Elsevier, Amsterdam (1989) 127.
[66] J.E. Klemberg-Sapieha, J. Oberste-Berghaus, L. Martinu, R. Blacker, I. Stevenson, G. Sadkhin, Appl. Optics 43 (2004) 2670.
[67] A. Manenschijn, W.J. Goedheer, J. Appl. Phys. 69 (1991) 2923.
[68] A. Amassian, M. Svec, P. Desjardin, L. Martinu, J. Vac. Sci. Technol. A 24 (2006) 2061.
[69] A. Amassian, M. Svec, P. Desjardins, L. Martinu, J. Appl. Phys. 100 (2006) 063526.
[70] P. Jedrzejowski, A. Amassian, E. Bousser, J.E. Klemberg-Sapieha, L. Martinu, Appl. Phys. Lett. 88 (2006) 071915.
[71] M.R. Wertheimer, A.C. Fozza, A. Hollander, Nucl. Instrum. Methods Phys. Res. B 151 (1999) 65.
[72] A. Hollander, J.E. Klemberg-Sapieha, M.R. Wertheimer, J. Polym. Sci. A, Polym. Chem. 33 (1995) 2013.
[73] S.C. Gujrathi, in: E. Sacher, J.J. Pireaux, S.P. Kowalczyk (Eds.), Metallized Polymers, Vol. 440, ACS Symposium Series, ACS, Washington, DC (1990) 88.
[74] L.C. Feldman, J.W. Mayer, Fundamentals of Surface and Thin Film Analysis, North Holland, Elsevier Science, Amsterdam (1986).
[75] H. Bubert, H. Jenett (Eds.), Surface and Thin Film Analysis: A Compendium of Principles, Instrumentation, and Applications, Wiley-VCH, Weinheim (2002).
[76] M. Ohring, Materials Science of Thin Films, Academic Press, New York (1992).
[77] M. Born, E. Wolf, Principles of Optics, 6th ed., Pergamon, New York (1993).
[78] F. Urbach, Phys. Rev. 89 (1953) 1189.
[79] A.R. Forouhi, I. Bloomer, Phys. Rev. B 34 (1986) 7018.
[80] G.E. Jellison Jr., F.A. Modine, Appl. Phys. Lett. 69 (1996) 371 Erratum 69 (1996) 2137.
[81] D.A.G. Bruggeman, Ann. Phys. Leipzig 24 (1935) 636.
[82] D. Stroud, Phys. Rev. B 12 (1975) 3368.
[83] J.C. Garland, D.B. Tanner (Eds.), Electrical Transport and Optical Properties of Inhomogeneous Media, AIP Conf. Proc., Vol. 40, AIP, New York (1978).
[84] D.E. Aspnes, Chap. 5, in: E.D. Palik (Ed.), Handbook of Optical Constants of Solids, Academic, San Diego, CA (1985) 89.
[85] W.C. Oliver, G.M. Pharr, J. Mater. Res. 7 (1992) 1564.

[86] K. Holmberg, A. Matthews, Coatings Tribology; Properties, Techniques and Applications in Surface Engineering, Elsevier, New York (1998).
[87] L. Martinu, in: R. d'Agostino, P. Favia, F. Fracassi (Eds.), Plasma Treatments and Deposition of Polymers, Kluwer Academic Publishers, Dordrecht (1997) 247.
[88] P.J. Burnett, D.S. Rickerby, Thin Solid Films 154 (1987) 403.
[89] E. Stansbury, R. Buchanan, Fundamentals of Electrochemical Corrosion, ASM International (2000).
[90] M. Azzi, J.A. Szpunar, Biomol. Eng. 24 (2007) 443.
[91] L. Eckertova, Physics of Thin Films, Springer, New York (1986).
[92] W.M.M. Kessels, A.H.M. Smets, D.C. Marra, E.S. Aydil, D.C. Schram, M.C.M. van de Sanden, Thin Solid Films 383 (2001) 154.
[93] G. Lucovsky, M.J. Manitini, J.K. Srivastava, E.A. Irene, J. Vac. Sci. Technol. B 5 (1987) 530.
[94] R.A.B. Devine, M. Marchand, Appl. Phys. Lett. 63 (1993) 619.
[95] P.J. Martin, R.P. Netterfield, W.G. Sainty, J. Appl. Phys. 55 (1984) 235.
[96] A. Gupta, S. Toby, E.P. Gusev, H. Lu, Y. Li, M.L. Green, Prog. Surf. Sci. 59 (1998) 103.
[97] A. Ricard, J.E. Oseguera-Pena, L. Falk, H. Michel, M. Gantois, IEEE Trans. Plasma Sci. 18 (1996) 940.
[98] W. Hsieh, C.Y. Chang, S.C. Hsu, J. Appl. Phys. 74 (1993) 2638.
[99] S.M. Han, E.S. Aydil, J. Vac. Sci. Technol. A 14 (1996) 2062.
[100] N. Bertrand, B. Drevillon, P. Bulkin, J. Vac. Sci. Technol. A 16 (1998) 63.
[101] Y. Watanabe, M. Shiratani, Jpn. J. Appl. Phys. Part 1 32 (1993) 3074.
[102] A. Love, S. Middleman, A.K. Hochberg, J. Cryst. Growth 129 (1993) 119.
[103] D. Shamiryan, T. Abell, F. Iacopi, K. Maex, Mater. Today 7 (2004) 34.
[104] S.M. Han, E.S. Aydil, J. Appl. Phys. 83 (1998) 2172.
[105] C. Vallee, A. Goullet, F. Nicolazo, A. Granier, G. Turban, J. Non-Cryst. Solids 311 (1997) 212.
[106] J. Robertson, Philos. Mag. B 63 (1991) 47.
[107] D. Poitras, P. Leroux, J.E. Klemberg-Sapieha, S.C. Gujrathi, L. Martinu, Opt. Eng. 35 (1996) 2693.
[108] F. Fracassi, R. d'Agostino, G. Bruno, Plasmas Polymers 1 (1996) 3.
[109] R. Vernhes, O. Zabeida, A. Amassian, J.E. Klemberg-Sapieha, L. Martinu, Appl. Optics 43 (2004) 97.
[110] H.G. Tompkins, R.B. Gregory, P.W. Deal, S.M. Smith, J. Vac. Sci. Technol. A 17 (1999) 391.
[111] L. Martinu, in: S.I. Najafi, M.N. Armenise (Eds.), Functional Photonic and Fiber Devices, Vol. 2695, SPIE, Bellingham, WA (1994) 30.
[112] J.E. Klemberg-Sapieha, L. Martinu, M.R. Wertheimer, P. Günther, R. Schellin, C. Thielemann, G. Sessler, J. Vac. Sci. Technol. A 14 (1996) 2775.
[113] T. Hattori, S. Semura, N. Akasaka, Jpn. J. Appl. Phys. Part 1 38 (1999) 2775.
[114] W.-T. Tseng, Y.-T. Hsieh, C.-F. Lin, M.-S. Tsai, M.-S. Feng, J. Electrochem. Soc. 144 (1997) 1100.
[115] A. Badzian, T. Badzian, R. Roy, W. Drawl, Thin Solid Films 354 (1999) 148.
[116] Z. He, G. Carter, J.S. Colligon, Thin Solid Films 283 (1996) 90.
[117] A.M. Wrobel, A. Walkiewicz-Pietrzykowska, J.E. Klemberg-Sapieha, Y. Nakanishi, T. Aoki, Y. Hatanaka, Chem. Mater. 15 (2002) 1749.
[118] P. Jedrzejowski, J. Cizek, J.E. Klemberg-Sapieha, J. Vlcek, L. Martinu, Thin Solid Films 447–448 (2004) 201.
[119] R.F. Davis, Diamond Films and Coatings – Development, Properties and Applications, Noyes, Park Ridge, NJ (1993).
[120] J. Robertson, Mater. Sci. Eng. R37 (2002) 129.
[121] R. Clausing, L. Horton, J. Angus, P. Koidl (Eds.), Diamond and Diamond-Like Films and Coatings, Plenum, New York (1991).
[122] J. Pouch, S.A. Alterovitz (Eds.), Properties and Characterization of Amorphous Carbon Films, Materials, Science Forum, Vols. 52–53, Trans. -Tech., Aedermannsdorf, Switzerland (1990).
[123] A. Raveh, L. Martinu, S.C. Gujrathi, J.E. Klemberg-Sapieha, M.R. Wertheimer, Surf. Coat. Technol. 53 (1992) 275.
[124] J. Houska, J.E. Klemberg-Sapieha, L. Martinu, Surf. Coat. Technol. 203 (2009) 3770.

[125] N. Hellgren, M.P. Johansson, E. Broitman, L. Hultman, J.-E. Sundgren, Phys. Rev. B 59 (1999) 5162.
[126] R.E. Sah, B. Dischler, A. Bubenzer, P. Koidl, Appl. Phys. Lett. 46 (1985) 739.
[127] D. Lusk, M. Gore, W. Boardman, T. Casserly, K. Boinapally, M. Oppus, Diamond Relat. Mater. 17 (2008) 1613.
[128] L.S. Pan, D.R. Kania (Eds.), Diamond: Electronic Properties and Applications, Kluwer Academic, Dordrecht (1995).
[129] A. Feldman, Y. Tzeng, W.A. Yarbrough, M. Yoshikawa, M. Murakawa (Eds.), Applications of Diamond Films and Related Materials, Vol. 885, National Institute of Standards and Technology, Washington, DC (1995).
[130] C.F.M. Borges, M. Moisan, A. Gicquel, Diamond Relat. Mater. 4 (1995) 149.
[131] W.J. Zhang, Y.M. Chong, I. Bello, S.T. Lee, J. Phys. D: Appl. Phys. 40 (2007) 6159.
[132] C.Y. Chan, W.J. Zhang, S. Matsumoto, I. Bello, S.T. Lee, J. Crystal Growth 247 (2003) 438.
[133] H.Q. Li, K.M. Leung, K.L. Ma, Q. Ye, Y.M. Chong, Y.S. Zou, Appl. Phys. Lett. 91 (2007) 201918.
[134] H. Biederman, Plasma Polymer Films, Imperial College Press (2004).
[135] A. Alptekin, E. Sacher, G. Czeremuszkin, L. Martinu, M. DiRenzo, Electrochem. Soc. Proc. 97–8 (1998) 58.
[136] C.I. Butoi, N.M. Mackie, J.L. Barnd, E.R. Fisher, Chem. Mater. 11 (1999) 862.
[137] D. Zhang, M.J. Kushner, J. Vac. Sci. Technol. A 19 (2001) 524.
[138] E. Kay, J. Coburn, A. Dilks, Top. Curr. Chem. 94 (1980) 1.
[139] C.B. Labelle, K.K. Gleason, J. Vac. Sci. Technol. A 17 (1999) 445.
[140] A. Weber, R. Pochelmann, C.-P. Klages, J. Vac. Sci. Technol. A 16 (1998) 2120.
[141] U. Hetzler, E. Kay, J. Appl. Phys. 49 (1978) 5617.
[142] L. Martinu, H. Biederman, J. Nedbal, Thin Solid Films 136 (1986) 11.
[143] L. Martinu, J.E. Klemberg-Sapieha, in: N. Kaiser, H.K. Pulker (Eds.), Optical Interference Coatings, Springer (2003) 359.
[144] Y.H. Lee, K.K. Chan, M.J. Brady, J. Vac. Sci. Technol. A 13 (1995) 596.
[145] Y.H. Lee, Vacuum 51 (1998) 503.
[146] S. Larouche, H. Szymanowski, J.E. Klemberg-Sapieha, L. Martinu, S.C. Gujrathi, J. Vac. Sci. Technol. A 22 (2004) 1200.
[147] H. Szymanowski, O. Zabeida, J.E. Klemberg-Sapieha, L. Martinu, J. Vac. Sci. Technol. A 23 (2005) 241.
[148] J.-P. Masse, H. Szymanowski, O. Zabeida, A. Amassian, J.E. Klemberg-Sapieha, L. Martinu, Thin Solid Films 515 (2006) 1674.
[149] F. Arefi-Khonsari, F. Hellegouarc'h, J. Amouroux, J. Vac. Sci. Technol. A 16 (1998) 2240.
[150] J.H. Lee, D.S. Kim, Y.H. Lee, J. Electrochem. Soc. 143 (1996) 1443.
[151] K. Itoh, O. Matsumoto, Thin Solid Films 345 (1999) 29.
[152] T. Gato, W. Zhang, T. Hirai, Jpn. J. Appl. Phys. Part 1 38 (1999) 3668.
[153] J. Patscheider, S. Veprek, Plasma Chem. Plasma Process. 12 (1992) 129.
[154] C.E. Chryssou, C.W. Pitt, IEEE J. Quantum Electron. 34 (1998) 282.
[155] W.B. Henley, G.J. Sacks, J. Electrochem. Soc. 144 (1997) 1045.
[156] M. Seman, C.A. Wolden, J. Vac. Sci. Technol. A 21 (2003) 1927.
[157] C.G. Granqvist, Solar Energy Mater. Solar Cells 60 (2000) 201.
[158] M. Seman, C.A. Wolden, Solar Energy Mater. Solar Cells 82 (2004) 517.
[159] U. Kreibig, P. Zacharias, Z. Phys. 231 (1970) 128.
[160] D. Ricard, P. Roussignol, C. Flytzanis, Opt. Lett. 10 (1985) 511.
[161] F. Hache, D. Ricard, C. Flytzanis, U. Kreibig, Appl. Phys. A: Solids Surf. 47 (1988) 347.
[162] H.B. Liao, R.F. Xiao, J.S. Fu, H. Wang, K.S. Wong, G.K.L. Wong, Opt. Lett. 23 (1998) 388.
[163] J.-M. Lamarre, F. Billard, C. Harkati-Kerboua, M. Lequime, S. Roorda, L. Martinu, Opt. Commun. 281 (2008) 331.
[164] S. Veprek, J. Vac. Sci. Technol. A 17 (1999) 2401.
[165] A.A. Voevodin, J.P. O'Neill, J.S. Zabinski, Surf. Coat. Technol. 116–119 (1999) 36.
[166] J. Musil, Surf. Coat. Technol. 125 (2000) 322.

[167] P. Jedrzejowski, B. Baloukas, J.E. Klemberg-Sapieha, L. Martinu, J. Vac. Sci. Technol. A 22 (2004) 725.
[168] H. Holleck, in: A. Kumar, Y.W. Chung, J.J. Moore, J.E. Smugeresky (Eds.), Surface Engineering: Science and Technology I, Minerals, Metals and Materials Society (1999) 207.
[169] S. Veprek, A.S. Argon, Surf. Coat. Technol. 146–147 (2001) 175.
[170] J. Patscheider, T. Zehnder, M. Diserens, Surf. Coat. Technol. 146 (2001) 201.
[171] P. Jedrzejowski, J.E. Klemberg-Sapieha, L. Martinu, Thin Solid Films 426 (2003) 150.
[172] P. Jedrzejowski, J.E. Klemberg-Sapieha, L. Martinu, Thin Solid Films 466 (2004) 189.
[173] L. Hultman, J. Bareño, A. Flink, H. Söderberg, K. Larsson, V. Petrova, Phys. Rev. B 75 (2007) 155437.
[174] J. Houska, J.E. Klemberg-Sapieha, L. Martinu, Surf. Coat. Technol. 203 (2009) 3348.
[175] I. Zukerman, A. Raveh, Y. Landu, R. Weiss, R. Shneck, Y. Shneor et al., Surf. Coat. Technol. 201 (2007) 6171.
[176] T. Bell, H. Dong, Y. Sun, Tribol. Int. 31 (1998) 127.
[177] R. Snyders, E. Bousser, P. Amireault, J.E. Klemberg-Sapieha, E. Park, K. Taylor, Plasma Process. Polym. 4 (2007) S640.
[178] C. Campillo, S. Illias, C.F.M. Borges, M. Moisan, L. Martinu, New Diamond Front Carbon Technol. 11 (2001) 147.
[179] M. Azzi, M. Paquette, J.A. Szpunar, J.E. Klemberg-Sapieha, L. Martinu, Wear 267 (2009) 860.
[180] M.R. Wertheimer, L. Martinu, J.E. Klemberg-Sapieha, G. Czeremuszkin, in: K.L. Mittal, L. Pizzi (Eds.), Adhesion Promotion Techniques, Marcel Dekker, New York (1999) 139.
[181] J.E. Klemberg-Sapieha, D. Poitras, L. Martinu, N.L.S. Yamasaki, C.W. Lantman, J. Vac. Sci. Technol. A 15 (1997) 985.
[182] A.S. Da Silva-Sobrinho, M. Latrèche, G. Czeremuszkin, J.E. Klemberg-Sapieha, M.R. Wertheimer, J. Vac. Sci. Technol. A 16 (1998) 3190.
[183] J.E. Klemberg-Sapieha, L. Martinu, N.L.S. Yamasaki, C.W. Lantman, Thin Solid Films 476 (2005) 101.
[184] A. Bergeron, J.E. Klemberg-Sapieha, L. Martinu, J. Vac. Sci. Technol. A 16 (1998) 3227.
[185] A.S. Da Silva Sobrinho, N. Schühler, J.E. Klemberg-Sapieha, M.R. Wertheimer, M. Andrews, S.C. Gujrathi, J. Vac. Sci. Technol. A 16 (1998) 2021.
[186] A. Bergeron, D. Poitras, L. Martinu, Opt. Eng. 39 (2000) 825.
[187] S. Dahl, D. Rats, J. von Stebut, L. Martinu, J.E. Klemberg-Sapieha, Thin Solid Films 355–356 (1999) 290.
[188] K. Seshan (Ed.), Handbook of Thin-film Deposition Processes and Techniques: Principles, Methods, Equipment and Applications, William Andrew (2002).
[189] P.K. Chu, J.Y. Chen, L.P. Wang, N. Huang, Mater. Sci. Eng. R36 (2002) 143.
[190] H. Liang, B. Shi, A. Fairchild, T. Cale, Vacuum 73 (2004) 317.
[191] J.C. Sit, D. Vick, K. Robbie, M.J. Brett, J. Mater. Res. 14 (1999) 1197.
[192] R. Vernhes, O. Zabeida, J.E. Klemberg-Sapieha, L. Martinu, Appl. Opt. 43 (2004) 97.
[193] D. Bohling, M. Coda, R. Blacker, C. Burton, R. Gove, P. Murphy, in: Proc. 43rd Annu. Tech. Conf. of the SVC, Denver (2000) 222.
[194] R. Hora, C. Wohlrab, in: Proc. 36th Annu. Tech. Conf. of the SVC (1993) 51.
[195] R. Beckmann, K.D. Nauenberg, T. Naumann, U. Patz, G. Ieked, H. Hagedorn, in: Proc. 44th Annu. Tech. Conf. of the Society of Vacuum Coaters (SVC), Philadelphia (2001) 288.
[196] M.H. Blees, G.B. Winkelman, A.R. Balkenende, J.M.J. den Toonder, Thin Solid Films 359 (2000) 1.
[197] J.A. Dobrowolski, Chap. 42, in: M. Bass (Ed.), Optical Society of America's Handbook of Optics, McGraw–Hill, New York (1995).
[198] S. Pongratz, A. Zöller, J. Vac. Sci. Technol. A 10 (1992) 1897.
[199] U. Schulz, U.B. Schallenberg, N. Kaiser, Appl. Opt. 41 (2002) 3107.
[200] D. Poitras, L. Martinu, Appl. Opt. 39 (2000) 1168.
[201] J.E. Klemberg-Sapieha, L. Martinu, V. Fridman, D.E. Morton, in: Proc. of the 41st Annu. Tech. Conf. of Society of Vacuum Coaters (SVC), Chicago (1998) 138.
[202] A.C. Greenham, B.A. Nichols, R.M. Wood, N. Nourshargh, K.L. Lewis, Opt. Eng. 32 (1993) 1018.
[203] P.L. Swart, P.V. Bulkin, B.M. Lacquet, Opt. Eng. 36 (1997) 1215.

[204] R. Vernhes, A. Amassian, J.E. Klemberg-Sapieha, L. Martinu, J. Appl. Phys. 99 (2006) 114315.
[205] D. Poitras, S. Larouche, L. Martinu, Appl. Opt. 41 (2002) 5249.
[206] S. Larouche, L. Martinu, Appl. Opt. 47 (2008) 4321.
[207] D. Rats, D. Poitras, J.M. Soro, L. Martinu, J. von Stebut, Surf. Coat. Technol. 111 (1999) 220.
[208] D. Rats, J.M. Soro, L. Martinu, J. von Stebut, Surf. Coat. Technol. 123 (2000) 36.
[209] R. Vernhes, PhD Thesis, École Polytechnique de Montréal, Montréal, Québec, Canada, 2006.
[210] J.M. Mir, J.A. Agostinelli, J. Vac. Sci. Technol. A 12 (1994) 1439.
[211] K. Worhoff, P.V. Lambeck, A. Driessen, J. Lightwave Technol. 17 (1999) 1401.
[212] F. Bruno, M. del Guidice, R. Recca, F. Testa, Appl. Opt. 30 (1991) 4560.
[213] G. Giroult-Matlakowski, C. Charles, A. Durandet, R.W. Boswell, S. Armand, H.M. Persing et al., J. Vac. Sci. Technol. A 12 (1994) 2754.
[214] M. Hoffmann, P. Kopka, E. Voges, IEEE Photonics Technol. Lett. 9 (1997) 1238.
[215] W. Wirges, S. Bauer-Gogonea, S. Bauer, R. Gerhard-Multhaupt, L. Martinu, J.E. Klemberg-Sapieha, M.R. Wertheimer, in: Proc. SPIE 2213 (1994) 303.
[216] C. Wagner, J. Frankenberger, P.P. Deimel, IEEE Photonics Technol. Lett. 5 (1993) 1257.
[217] D.K.W. Lam, Appl. Opt. 23 (1984) 2744.
[218] S. Yokoyama, A.T. Nagata, Y. Kuroda, T. Doi, T. Namba, K. Miyake, J. Vac. Sci. Technol. A 13 (1995) 629.
[219] A. Malek-Tabrizi, S.I. Najafi, L. Martinu, in: S.I. Najafi, M.N. Armenise (Eds.), Functional Photonic and Fiber Devices, Vol. 2695, SPIE, Bellingham, WA (1996) 180.
[220] D.R. Beltrami, J.D. Love, A. Durandet, A. Samoc, C.J. Cogswell, Appl. Opt. 36 (1997) 7143.
[221] A.H. Mahan, Solar Energy Mater. Solar Cell 78 (2003) 299.
[222] S. Guha, J. Yang, J. Non-Cryst. Solids 352 (2006) 1917.
[223] A.V. Shah, J. Meier, E. Vallat-Sauvain, J. Wyrsch, U. Kroll, C. Droz, U. Graf, Solar Energy Mater. Solar Cells 78 (2003) 469.
[224] S. Guha, J. Yang, A. Banerjee, B. Yan, K. Lord, Solar Energy Mater. Solar Cells 78 (2003) 329.
[225] O. Vetterl, F. Finger, R. Carius, P. Hapke, L. Houben, O. Kluth, Solar Energy Mater. Solar Cells 62 (2000) 97.
[226] J. Yang, A. Banerjee, S. Guha, Solar Energy Mater. Solar Cells 78 (2003) 597.
[227] M. Zeuner, Private communication.
[228] H. Chatham, Surf. Coat. Technol. 78 (1996) 1.
[229] N. Schühler, A.S. da Silva Sobrinho, J.E. Klemberg-Sapieha, M. Andrews, M.R.S. Wertheimer, in: Proc. 39th Annu. Tech. Conf. of the Society of Vacuum Coaters (SVC), Philadelphia, PA (1996) 285.
[230] A.S. Da Silva Sobrinho, G. Czeremuszkin, M. Latrèche, M.R. Wertheimer, J. Vac. Sci. Technol. A 18 (2000) 149.
[231] J.D. Affinito, M.E. Gross, C.A. Coronado, G.L. Graff, E.N. Greenwell, P.M. Martin, in: Proc. 39th Annu. Tech. Conf. of the Society of Vacuum Coaters (SVC) (1996) 397.
[232] M.E. Gross, P.M. Martin, L.C. Olsen, G.L. Graff, P.E. Burrows, C.C. Bonham et al., in: Proc. 46th Annu. Tech. Conf. of the Society of Vacuum Coaters (SVC) (2003) 89.
[233] J. Madocks, J. Rewhinkle, L. Barton, Mater. Sci. Eng. B 119 (2005) 268–273.
[234] C.G. Granqvist, Solar Energy Mater. Solar Cells 92 (2008) 203.
[235] T. Ellison, B. Dotter, M. Izu, S. Ovshinsky, in: Proc. 40th Annu. Tech. Conf. of the Society of Vacuum Coaters (SVC) (1997) 309.
[236] D. Garg, P.B. Henderson, R.E. Hollingsworth, D.G. Jensen, Mater. Sci. Eng. B 119 (2005) 224.
[237] S. Guruvenket, D. Li, J.E. Klemberg-Sapieha, L. Martinu, J. Szpunar, Surf. Coat. Technol. 203 (2009) 2905.
[238] Y.T. Cheng, C.M. Cheng, Appl. Phys. Lett. 73 (1998) 614.
[239] A. Leyland, A. Matthews, Wear 246 (2000) 1.
[240] J. Musil, M. Jirout, Surf. Coat. Technol. 210 (2007) 5148.
[241] D. Galvan, Y.T. Pei, J.T.M. De Hosson, Surf. Coat. Technol. 200 (2006) 6718.
[242] S. Hassani, M. Bielawski, W. Beres, L. Martinu, M. Balazinski, J.E. Klemberg-Sapieha, Surf. Coat. Technol. 203 (2008) 204.
[243] J.E. Klemberg-Sapieha, L. Martinu et al., unpublished.

[244] S. Hassani, J.E. Klemberg-Sapieha, M. Bielawski, W. Beres, L. Martinu, M. Balazinski, Wear 265 (2008) 879.
[245] C. Donnet, A. Erdemir (Eds.), Tribology of Diamond-Like Carbon Films: Fundamentals and Applications, Springer, New York (2008).
[246] R. Butter, M. Allen, L. Chandra, A.H. Lettington, N. Rushton, Diamond Relat. Mater. 4 (1995) 857.
[247] P.E. Sinnet-Jones, J.A. Wharton, R.J.K. Wood, Wear 259 (2005) 898.
[248] A.S. Shanbhag, J.J. Jacobs, J. Black, J.O. Galante, T.T. Glant, J. Biomed. Mater. Res. 28 (1994) 81.
[249] H.F. Hildebrand, J.-C. Hornez, J.A.H. Helsen, Chap. 9, in: J. Breme (Ed.), Biological Response and Biocompatibility, John Wiley and Sons (1998).
[250] O. Zabeida, J.E. Klemeberg-Sapieha, L. Martinu, unpublished.
[251] S.D.A. Lawes, M.E. Fitzpatrick, S.V. Hainsworth, J. Phys. D.: Appl. Phys. 40 (2007) 5427.